ABSTRACT

MEASUREMENT OF SUB-PICOSECOND ELECTRON BUNCHES VIA ELECTRO-OPTIC SAMPLING OF COHERENT TRANSITION RADIATION

Timothy John Maxwell, Ph.D.
Department of Physics
Northern Illinois University, 2012
Philippe Piot, Director

Future collider applications as well as present high-gradient laser plasma wakefield accelerators and free-electron lasers operating with picosecond bunch durations place a higher demand on the time resolution of bunch distribution diagnostics. This demand has led to significant advancements in the field of electro-optic sampling over the past ten years. These methods allow the probing of diagnostic light such as coherent transition radiation or the bunch wakefields with sub-picosecond time resolution. We present results on the single-shot electro-optic spectral decoding of coherent transition radiation from bunches generated at the Fermilab A0 photoinjector laboratory. A longitudinal double-pulse modulation of the electron beam is also realized by transverse beam masking followed by a transverse-to-longitudinal phase-space exchange beamline. Live profile tuning is demonstrated by upstream beam focusing in conjunction with downstream monitoring of single-shot electro-optic spectral decoding of the coherent transition radiation.

NORTHERN ILLINOIS UNIVERSITY
DE KALB, ILLINOIS

MAY 2012

MEASUREMENT OF SUB-PICOSECOND ELECTRON BUNCHES VIA ELECTRO-OPTIC SAMPLING OF COHERENT TRANSITION RADIATION

BY

TIMOTHY JOHN MAXWELL
© 2012 Timothy John Maxwell

A DISSERTATION SUBMITTED TO THE GRADUATE SCHOOL
IN PARTIAL FULFILLMENT OF THE REQUIREMENTS
FOR THE DEGREE
DOCTOR OF PHILOSOPHY

DEPARTMENT OF PHYSICS

Dissertation Director:
Philippe Piot

ACKNOWLEDGEMENTS

First and foremost I acknowledge advisors Philippe Piot and Jinhao Ruan for their valuable input and mentoring over the years. Thanks to Mike Church and Helen Edwards for guidance and support throughout the project as well as Michael Kucera of Fermi National Accelerator laboratory, Michael Maikowski and Art Camire at Newport Corporation's Spectra Physics division for technical support. And finally thanks to all of my colleagues at Fermilab's A0 photoinjector laboratory, Alex Lumpkin, Randy Thurman-Keup, Charles Tobin, Yin-e Sun, Congcong Tan, James Santucci, Amber Johnson, and Liana Nicklaus for their contributions, athletic training, and many fruitful discussions. This work was supported by the Fermi Research Alliance, LLC under U.S. Department of Energy Contract Number DE-AC02-07CH11359, and Northern Illinois University under U.S. Department of Defense DURIP program Contract N00014-08-1-1064.

DEDICATION

For my dear family and friends (especially Ann)

TABLE OF CONTENTS

Page

LIST OF TABLES vii

LIST OF FIGURES viii

Chapter

1 INTRODUCTION 1

2 ACCELERATOR PHYSICS AND APPARATUS 5

- 2.1 Accelerator Layout 5
- 2.2 Definition of beam parameters 6
- 2.3 Emittance exchange line 10
- 2.4 Transition radiation 11
  - 2.4.1 Single-electron transition radiation response 12
  - 2.4.2 Transition radiation of a bunch 16
- 2.5 Existing diagnostics 18
  - 2.5.1 Martin-Puplett Interferometer 18
  - 2.5.2 Streak Camera 20
  - 2.5.3 Emittance measurement 21
- 2.6 Ellipsoidal bunch 23

3 OPTICAL THEORY 26

- 3.1 The wave equation 27
- 3.2 Free-wave solution and 1D description of an optical pulse 29
  - 3.2.1 The spectral phase and time-bandwidth product 31
  - 3.2.2 Wigner distribution function 32
  - 3.2.3 Example: the Gaussian pulse 33
    - 3.2.3.1 Transform-limited pulse 34
    - 3.2.3.2 Optical pulse with higher order dispersion 35
- 3.3 Linear, isotropic medium and dispersion 39

Chapter Page

3.4 Anisotropic medium and birefringence . . . 43

3.4.1 Polarization optics and Jones vectors . . . 47

4 ELECTRO-OPTIC SPECTRAL DECODING. . . . 51

4.1 Qualitative description of electro-optic spectral decoding . . . 51

4.2 Titanium-sapphire laser layout . . . 54

4.3 Optical apparatus for EOSD . . . 55

4.4 Quantitative analysis of electro-optic spectral decoding . . . 58

4.4.1 Form of the second-order polarization coupling . . . 58

4.4.2 Dependence of coupling strength on crystal rotation. . . . 64

4.4.3 Spectral decoding approximation . . . 69

4.4.3.1 Dispersion effects . . . 70

4.4.3.2 Chirped pulse distortions . . . 74

5 LASER SYNCHRONIZATION AND CHARACTERIZATION . . . 79

5.1 Coarse triggering of the Ti:sapph amplifier . . . 80

5.1.1 1-kHz burst generation. . . . 81

5.1.2 Intensity dependence on unstable triggering . . . 82

5.1.3 1-kHz trigger synthesizer . . . 86

5.2 Fine synchronization . . . 88

5.2.1 Initial phase measurements . . . 89

5.2.2 Simultaneous streaking of two images . . . 92

5.2.3 Secondary laser phase monitor and feedback. . . . 94

5.2.4 Measurement of corrected laser-to-laser drift. . . . 96

5.3 Temporal pulse shape measurement . . . 98

5.3.1 SHG FROG. . . . 99

5.3.1.1 SHG FROG optical system. . . . 100

5.3.1.2 The signal and effect of phase mismatch . . . 102

5.3.1.3 SHG FROG traces and reconstruction . . . 107

5.3.2 FROG measurements . . . 110

5.3.2.1 Pulse length optimization. . . . 111

Chapter Page

5.3.2.2 Chirped pulse measurement 113

6 BEAM MEASUREMENTS 116

6.1 Establishing synchronization 116

6.2 Dependence of signal strength on crystal orientation 118

6.3 Initial single bunch results with comparison to interferometery 118

6.4 Double beam generation by laser masking 122

6.5 Measurement of the double bunch 126

7 CONCLUSIONS 130

REFERENCES 132

LIST OF TABLES

Table Page

3.1 Resulting pulse widths for a laser pulse with higher-order dispersion 36

4.1 Ti:sapph laser parameters 54

6.1 Longitudinal emittance values for double beam 124
6.2 Double beam transverse emittance measurement 124

LIST OF FIGURES

Figure Page

1.1 Vectors defined for a moving particle 1

2.1 A0 photoinjector layout. 6
2.2 Phase space ellipse parameters 8
2.3 Geometry of the emittance exchanger 10
2.4 Image charge picture of transition radiation 13
2.5 Spectral fluence of CTR in the vicinity of a finite target 14
2.6 Illustration of CTR emission from a diagnostic cross. 15
2.7 Relative transmission function of CTR in the THz regime 15
2.8 Optical layout of a Martin-Puplett interferometer. 19
2.9 Schematic of streak camera operation 20
2.10 Transverse emittance measurement by slit method 22
2.11 Masked phase space of transverse emittance slit measurement. 23
2.12 Simulation of ellipsoidal bunch formation in the blow-out regime. 24

3.1 Gaussian Ti:sapph laser spectrum 36
3.2 Wigner distribution functions of a laser pulse with higher order dispersion 37
3.3 Extraordinary index of refraction for calcite. 42
3.4 Geometry for a field incident on a uniaxially birefringent crystal 45
3.5 Geometry of a beam-displacing polarizing prism 49

4.1 Overview of electro-optic spectral decoding process 52
4.2 Optical layout of Ti:sapph laser system 55
4.3 Optical layout of the 4-way beam combiner. 56
4.4 Optical layout of EOSD breadboard 57
4.5 Optical layout of polarization-resolving spectrometer 58

Figure Page

4.6 ZnTe crystal structure 62

4.7 Coordinate definitions for wave mixing in ZnTe 63

4.8 Signal strength as a function of crystal rotation angle 69

4.9 Indices of refraction for ZnTe 71

4.10 Propagation in ZnTe of a 1-ps Gaussian transient with a chirped laser pulse 72

4.11 Spiked bunch distribution with low-frequency losses 73

4.12 Propagation in ZnTe of the spiked distribution transient with a chirped laser pulse. 75

4.13 Sample signal with and without dispersion 76

4.14 Effect of chirp on the measurement of a 1-ps signal 77

5.1 Block diagram of laser timing system 81

5.2 Pump laser measurement for pulses occurring on edge of 100-pulse bursts 84

5.3 Variation of pump laser output with firing rate for pulses occurring on edge of 100-pulse burst 85

5.4 Variation of amplified Ti:sapph output with firing rate for pulses occurring on edge of 100-pulse burst 85

5.5 Burst generator/custom synthesizer performance comparison 88

5.6 Charge emitted from RF gun as function of gun-laser phase 90

5.7 Nd:YLF and Ti:sapph temporal stabilities by charge technique and streak camera 91

5.8 Demonstration of simultaneous streak imaging of two signals 93

5.9 Simultaneous streak imaging of Ti:sapph IR and OTR from Nd:YLF-generated electron beam 95

5.10 Block diagram of secondary, external phase feedback loop(s) 95

5.11 Feedback loop monitoring of Nd:YLF and Ti:sapph 96

5.12 Simultaneous streak imaging of Nd:YLF UV and Ti:sapph IR output with phase feedback enabled. 97

5.13 SHG FROG optical layout 100

5.14 SHG FROG interaction geometry 101

5.15 Index of refraction for BBO 104

5.16 Complex phase matching function for BBO crystal. 105

5.17 Phase matching bandwidth for BBO crystal. 106

Figure Page

5.18 Sample SHG FROG traces from pulse optimization measurement. 112

5.19 Marginals from pulse minimization measurement 112

5.20 Measurement and compensation of a nearly transform-limited pulse 113

5.21 SHG FROG repeatability 114

5.22 SHG FROG traces of a strongly chirped laser pulse 115

5.23 Measurement of a strongly chirped laser pulse 115

6.1 Determining relative laser delay using a crossed polarizer and photodiode 117

6.2 Variation of a recovered EOSD signal with crystal orientation. 119

6.3 Comparison of predicted signal strength orientation dependence to data 119

6.4 Recovered EOSD signals for two short electron bunches. 120

6.5 Comparison of EOSD to interferometry measurements of bunch compression by EEX . . 121

6.6 Masking of drive laser to generate transverse beam modulation 123

6.7 Transverse phase space of double beam before EEX 125

6.8 Simulated longitudinal phase spaces of double beam after EEX. 125

6.9 Simulated longitudinal distributions after EEX with focusing 126

6.10 Measured longitudinal distribution after EEX with focusing. 127

6.11 Repeated measurement of a double bunch. 128

6.12 Comparison of EOSD to interferometry for the double bunch 128

6.13 Double bunch widths and spacing compared to simulation. 129

CHAPTER 1

INTRODUCTION

Electron accelerators are a rapidly-advancing field of scientific research with widespread applications in industry and medicine. The production and acceleration of high-quality electron bunches with ultra-short durations (below 1 ps) can support the generation of short-wavelength coherent radiation using, e.g., the free-electron laser principle [1–4]. Low energy electron bunches can also be directly used to probe matter via electron microscopy with the availability of short bunches leading to four-dimensional electron microscopy [5], thereby enabling dynamic probing of transient phenomenon such as phase transitions or molecular reactions. Finally, high energy physics accelerators such as next generation electron-positron TeV-scale center-of-mass colliders call for sub-ps bunches at the interaction points [6]. The motivation of this dissertation is to develop a single-shot diagnostic capable of measuring the time distribution of relativistic electron bunches.

Many temporal electron bunch diagnostics rely on detecting the electromagnetic field associated with a moving bunch. To qualitatively describe the principle of operation, consider the field produced by a moving electron with charge e and trajectory $\mathbf{r}_i(t)$ as seen by an observer at $\mathbf{r}$, as illustrated in 1.1. In this figure

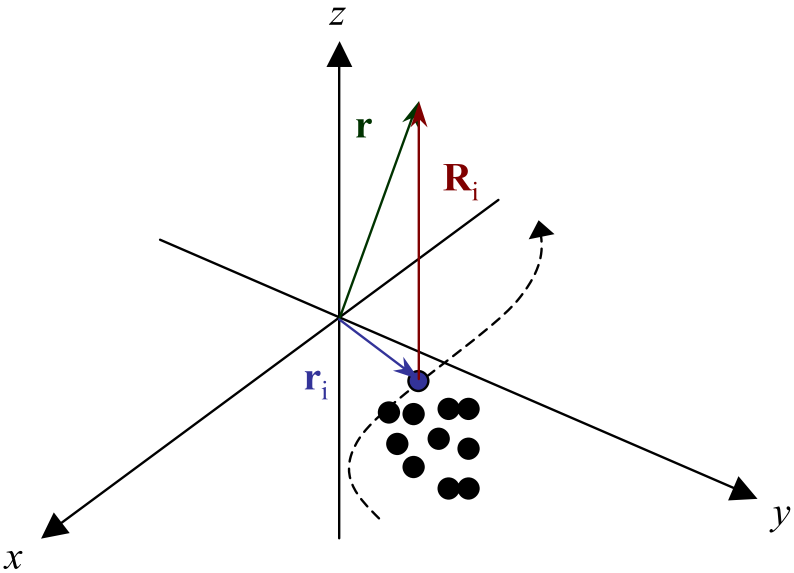

Figure 1.1: Geometry of vectors used for a moving particle.

$\mathbf{r}_i(t)$ describes the location of a single particle at time t, and the vector $\mathbf{R}_i(t) = \mathbf{r} - \mathbf{r}_i(t)$ is the relative vector between the two points at time t.

The resulting fields for this particle (neglecting subscript i) are obtained from the Liénard-Wiechert potential [7–9] as

$$\mathbf{E}(\mathbf{r},\ t) = \frac{e}{4\pi\epsilon_0}\left\{\frac{\hat{\mathbf{R}}-\boldsymbol{\beta}}{\gamma^2 R^2(1-\boldsymbol{\beta}\cdot\hat{\mathbf{R}})^3} + \frac{\hat{\mathbf{R}}\times\left[(\hat{\mathbf{R}}-\boldsymbol{\beta})\times\dot{\boldsymbol{\beta}}\right]}{cR(1-\boldsymbol{\beta}\cdot\hat{\mathbf{R}})^3}\right\}_{t=t'} \tag{1.1}$$

$$\mathbf{B}(\mathbf{r},\ t) = \frac{1}{c}\left[\hat{\mathbf{R}}\times\mathbf{E}\right]_{t=t'} \tag{1.2}$$

where $\mathbf{E}$ and $\mathbf{B}$ are the electric and magnetic fields, respectively, ϵ_0 is the permittivity of free space, $\boldsymbol{\beta} = \mathbf{v}/c = \dot{\mathbf{r}}_i/c$ with $\beta < 1$, and γ is the usual relativistic factor

$$\gamma = \frac{1}{\sqrt{1-\beta^2}}. \tag{1.3}$$

Note that the bracketed terms on the right-hand side are all evaluated at the retarded time $t' = t - R(t)/c$.

The first and second terms in the sum of Eq. (1.1) are frequently referred to as the velocity (or Coulomb) fields and acceleration (or radiation) fields, respectively, due to the second's dependence on the acceleration $\dot{\boldsymbol{\beta}}$. The $1/R^2$ and $1/R$ dependence of the velocity and acceleration fields, respectively, also imply that very far from the particle the radiation field dominates.

For a dense bunch of particles we may instead describe at every point $\mathbf{r}_i$ the continuous charge and current densities ρ and $\mathbf{J}$. By superposition we can sum over all charges and derive the Jefimenko equations [7, 8]

$$\mathbf{E}(\mathbf{r},t) = \frac{1}{4\pi\epsilon_0}\int\left[\left(\frac{\mathbf{r}-\mathbf{r}_i}{|\mathbf{r}-\mathbf{r}_i|^3}\right)\rho(\mathbf{r}_i,t') + \left(\frac{\mathbf{r}-\mathbf{r}_i}{|\mathbf{r}-\mathbf{r}_i|^2}\right)\frac{\dot{\rho}(\mathbf{r}_i,t')}{c} - \left(\frac{1}{|\mathbf{r}-\mathbf{r}_i|}\right)\frac{\dot{\mathbf{J}}(\mathbf{r}_i,t')}{c^2}\right]\mathrm{d}^3\mathbf{r}_i \tag{1.4}$$

$$\mathbf{B}(\mathbf{r},t) = \frac{1}{4\pi\epsilon_0 c^2}\int\left[\mathbf{J}(\mathbf{r}_i,t')\times\left(\frac{\mathbf{r}-\mathbf{r}_i}{|\mathbf{r}-\mathbf{r}_i|^3}\right) + \frac{\dot{\mathbf{J}}(\mathbf{r}_i,t')}{c}\times\left(\frac{\mathbf{r}-\mathbf{r}_i}{|\mathbf{r}-\mathbf{r}_i|^2}\right)\right]\mathrm{d}^3\mathbf{r}_i \tag{1.5}$$

with $\mathbf{R}_i = \mathbf{r} - \mathbf{r}_i$ and the integrations are performed over all space. Written this way, we see that the aggregate field takes the form of a (generally quite complicated) 3-dimensional vectorial convolution of the charge distribution and its trajectories (the phase space distribution) with the response function given by Eq (1.1). In many easily realized physical cases this can be expressed as a convolution that can be analytically reduced.

Therefore one can infer properties of the bunch distribution by observing the electromagnetic radiation generated under a well-defined situation. Some simple examples include measuring the passing of the velocity field as the beam drifts, the light thrown off as the beam follows the arcing path through a bending magnet (synchrotron radiation), or observing the light emitted when the beam strikes a target (transition radiation). From these one can design an experiment to measure the phase space distribution of a bunch. Using different, carefully chosen configurations a number of diagnostics can then be developed to probe the behavior of a charged particle beam to verify and tune its performance. With the bunch distribution having significant influence on experimental performance, diagnostics capable of measuring it become vital in the accelerator research and development process.

The goal of this dissertation is therefore to make use of these principles to develop and install a diagnostic with sufficient time resolution to measure a high-brightness electron beam with sub-picosecond time structure at the Fermilab A0 photoinjector (A0PI). Ultimately we used the diagnostics developed to study the generation and shaping of the longitudinal distribution of an electron beam by making use of a unique beam manipulation technique pioneered at A0PI.

This dissertation is arranged in six chapters. In Chap. 2 we will describe the accelerator at A0PI and some relevant principles of its operation. This includes the general layout of the beam line, details on its unique beam manipulation capabilities, and illustration of the particular radiative process used to generate the signal we will use to probe the longitudinal distribution.

As the technique we have chosen to probe this signal relies heavily on the use of an ultra-short, broadband laser pulse, Chap. 3 provides a review of some fundamentals in optics illustrated periodically by examples related to the experiment. This will further serve as a basis of the notation we will use in subsequent analyses.

With groundwork established, Chap. 4 begins with a qualitative overview of the technique chosen to measure the longitudinal distribution. Details on our experimental setup are described. With the optics fully defined, more precise quantitative details on the diagnostic process are explained with limitations of the measurement also addressed.

Chapter 4 will shed light on requirements for the synchronization of our instrumentation to the accelerator as well as calibration of the diagnostics. Chapter 5 therefore provides technical details on how these issues were overcome with final performance results.

We can then proceed in Chap. 6 to present measurements taken of the electron beam's longitudinal profile. Benchmarking of the experiment is demonstrated by the measurement of compressed bunches at A0PI. A proof of principle experiment on the generation of a beam with a longitudinal double pulse structure using novel masking techniques is then performed. We conclude in Chap. 7 with a summary of findings and their future implications.

CHAPTER 2

ACCELERATOR PHYSICS AND APPARATUS

We now introduce the accelerator as well as some fundamental concepts of accelerator physics relevant to our experiment. To begin we describe the accelerator layout and the A0PI emittance exchange line. The goal of this work is to measure the longitudinal distribution of the beam. We therefore introduce transition radiation and the relationship between its coherent spectrum and the longitudinal electron distribution. Additional diagnostics employed will briefly be described, as well as a related on-going experiment on beam generation.

2.1 Accelerator Layout

The A0 photoinjector (A0PI) facility [10] at Fermilab has provided electron beam in support of a variety of advanced accelerator R&D experiments over the last decade. Shown schematically in Fig. 2.1, the photoinjector utilizes a Cs_2Te photocathode located on the back plate of a 1-1/2 cell, 1.3-GHz resonant cavity operating on the $TM_{010,\pi}$ mode, referred to as the radio frequency (RF) gun. The photocathode is typically driven by the amplified, frequency quadrupled (263 nm) output of the existing drive laser using a neodymium-doped yttrium lithium fluoride (Nd:YLF) lasing medium to produce 3-ps pulses [11]. This Nd:YLF laser is capable of producing up to a 100-μs long train of pulses with a 1-MHz repetition rate.

As the laser strikes the photocathode, photoelectrons are produced. These are then accelerated by the field applied from the RF gun to a typical energy of 4 MeV with a total charge of $\sim$1 nC or less. Downstream of the gun, the 1.3-GHz, 9-cell superconducting RF (SCRF) booster cavity operating in the TM_{010} mode further accelerates the electron beam up to a maximum of 16 MeV.

A new laser system was also commissioned as a part of this experiment. This broadband, titanium-sapphire (Ti:sapph) laser can produce 100-fs duration laser pulses in the infrared (IR) to be used with the ultra-fast, laser-based diagnostics established here, or alternatively be tripled to the ultraviolet (UV) to be used as the accelerator drive laser. Details on this installation are presented in Chap. 5.

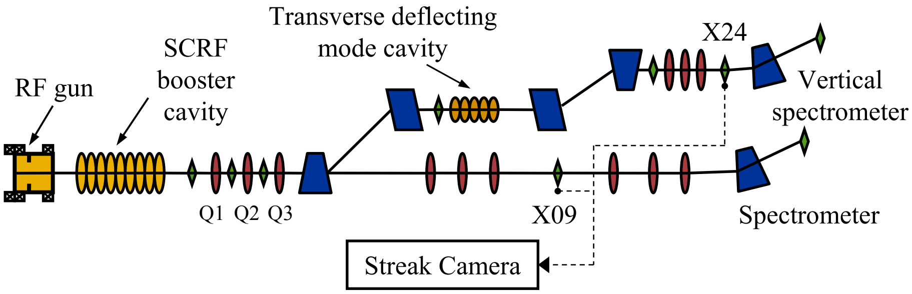

Figure 2.1: Top view of the A0 photoinjector setup. The red ellipses and blue trapezoids are quadrupole and dipole magnets, respectively. The OTR station labeled X09 was used for timing measurements and station X24 used for EOSD, with optical paths to the streak camera shown.

The beamline also includes quadrupole and dipole magnets necessary to control the beam's transverse size and trajectory. The beam then propagates down either the straight-ahead beamline for diagnostics and user studies or the emittance exchange (EEX) beamline [12–14]. As shown in Fig. 2.1, the latter consists of a 5-cell, TM_{110}-mode transverse deflecting cavity [15] flanked between two double dispersive bends referred to as doglegs. The RF gun, 9-cell SCRF cavity and 3.9-GHz deflecting mode cavity are all synchronized to the 1.3-GHz RF master oscillator.

The accelerator incorporates transverse and longitudinal phase-space diagnostic stations. The stations pertinent to the experiments presented in this paper are shown as X09 and X24 in Fig. 2.1. Both stations generate backward transition radiation using the conventional arrangement, discussed in Sec. 2.4. The light from either cross can be imaged to the entrance slit of a synchronized streak camera (Sec. 2.5.2).

2.2 Definition of beam parameters

For describing the configuration space of the individual particles that make up an electron bunch, we use the 6D coordinate system $(x,\ x',\ y,\ y',\ z,\ \delta)$ where x, y and z are the spatial coordinates of a particle relative to the mean reference trajectory $\vec{s}$, x' and y' are the divergences p_x/p_0 and p_y/p_0, and δ is the fractional relative momentum offset given in terms of the momentum coordinate p and the mean momentum p_0 via $\delta = (p - p_0)/p_0$.

In the case of a particle beam we have many particles that can be considered to have a continuous distribution. It is both practical and customary to describe them in 3 phase space ellipses (u, u') where u is a coordinate direction and u' the associated divergence, related to the conjugate momentum. The original derivation and parameterization of the ellipses were first described by Courant and Snyder [16], which we now summarize here.

Beam transport systems are comprised primarily of magnets designed to control beam trajectory and shape. Under the Lorentz force imposed by these fields, the equation of motion for a single electron along the trajectory s is like that of a simple harmonic oscillator (neglecting radiative effects) taking the form of Hill's equation [17]

$$u + K(s)u'' = 0 \tag{2.1}$$

where u is a given coordinate x, y, or z and $K(s)$ is the field strength. This is solved by a solution of the form

$$u(s) = \sqrt{\epsilon\beta(s)}\sin\left[\psi(s) + \phi_0\right], \tag{2.2}$$

where ϵ is a constant. The functions $\beta(s)$ and $\psi(s)$ are referred to as the beta function and phase advance, respectively.

Inserting these into Hill's equation (2.1) one finds that the phase advance is related to the beta function by

$$\psi(s) = \int_0^s \frac{ds'}{\beta(s')}. \tag{2.3}$$

We further define the functions

$$\begin{aligned} \alpha(s) &= \frac{1}{2}\beta' && (2.4) \\ \gamma(s) &= \frac{1 + \alpha^2(s)}{\beta(s)}. && (2.5) \end{aligned}$$

Combining all of these, one arrives at the expression for the Courant-Snyder invariant [17, 18]

$$\epsilon = \gamma(s)u^2(s) + 2\alpha(s)u(s)u(s)' + \beta(s)u'^2(s). \tag{2.6}$$

The parameter ϵ is therefore a constant of motion. Where the so-called Courant-Snyder parameters $\alpha(s), \beta(s)$ and $\gamma(s)$ are given, this describes an ellipse in u and u' with an area of $\pi\epsilon$ evolving along s. Therefore, if we choose the ellipse to reasonably enclose the initial distribution at $s = 0$, the evolution of all particles within the beam remain confined to orbits with smaller ϵ. This single phase space ellipse with $\epsilon = \epsilon_{max}$ can then be propagated through the beam lattice to compute the limiting beam envelope function

$$E(s) = \sqrt{\epsilon_{max}\,\beta(s)}. \tag{2.7}$$

In terms of the Courant-Snyder parameters and emittance ϵ, a Gaussian approximation for a continuous elliptical distribution is given by [18]

$$\rho(u,\ u') = \frac{1}{2\pi\epsilon}\exp\left[-\frac{\gamma u^2 + 2\alpha uu' + \beta u'^2}{2\epsilon}\right]. \tag{2.8}$$

The value of ϵ in this case corresponds to the area within the RMS ellipse for the distribution and is referred to as the emittance. For this case of uncoupled motion under conservative forces, this remains constant in each coordinate direction. This is a manifestation of Liouville's theorem.

Undamped and undriven coupled motion can also occur, though in this case it is the product of emittances $\epsilon = \epsilon_x\,\epsilon_y\,\epsilon_z$ that remains constant (a reaffirmation of Liouville's Theorem). Where non-conservative forces from, e.g., beam acceleration or synchrotron radiation losses take effect this is no longer the case.

The Courant-Snyder parameters along with the emittance provide, in an RMS sense, the orientation and extent of the phase space distribution of the particles in a bunch, as illustrated in Fig. 2.2 [17]. With the area

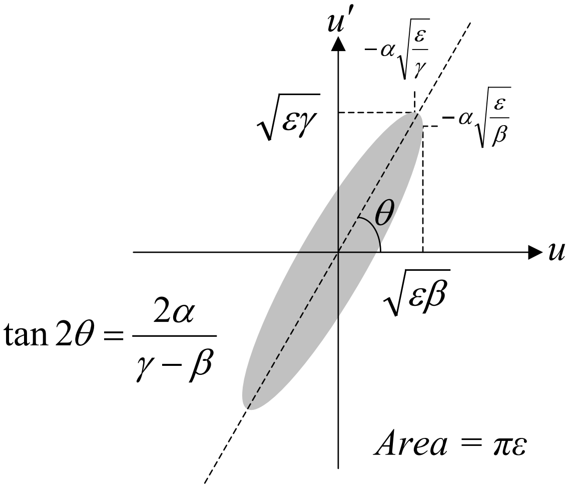
u'
$-\alpha\sqrt{\frac{\varepsilon}{\gamma}}$
$\sqrt{\varepsilon\gamma}$
$-\alpha\sqrt{\frac{\varepsilon}{\beta}}$
θ
u
$\sqrt{\varepsilon\beta}$
$\tan 2\theta = \frac{2\alpha}{\gamma-\beta}$
$Area = \pi\varepsilon$

Figure 2.2: The geometry of the phase space ellipse and their relation to the emittance ϵ and Courant-Snyder parameters α, β and γ.

of the ellipse fixed by ϵ, only two of the three Courant-Snyder parameters are independent with the third given geometrically

$$\beta\gamma - \alpha^2 = 1. \tag{2.9}$$

The significance of the Courant-Snyder parameters is clear from Fig. 2.2 with β related to the spatial extent of the beam, γ the spread in divergence and α the $u - u'$ correlation. Indeed, from Eq. (2.8) we can compute the moments of the bivariate Gaussian distribution to find [18]

$$\begin{aligned} \langle u^2 \rangle &= \epsilon\beta & (2.10) \\ \langle u'^2 \rangle &= \epsilon\gamma & (2.11) \\ \langle uu' \rangle &= -\epsilon\alpha. & (2.12) \end{aligned}$$

Combining these with Eq. 2.9 we can find ϵ in terms of the RMS values

$$\epsilon = \sqrt{\langle u^2 \rangle \langle u'^2 \rangle - \langle uu' \rangle^2}. \tag{2.13}$$

This RMS sense of ϵ is used in the case of arbitrary bunch distributions [17].

The emittance described so far is influenced by ordinary acceleration as the divergences are inversely related to the mean momentum. This effect is referred to as adiabatic damping. Therefore the normalized emittance

$$\epsilon^* = \beta\gamma\epsilon \tag{2.14}$$

is specified instead, where here β and γ refer to the relativistic factors. The normalized emittances do not scale under acceleration.

The ϵ_u^* describe the compactness of their corresponding phase spaces, a concern in high brightness accelerator applications such as colliders and light sources. Low transverse emittance implies a spatially compact beam with a small angular spread. The longitudinal emittance can also be defined in terms of bunch length and energy spread.

Where the emittance from a given source is minimized, further reduction requires damping such as that provided by a damping ring. For applications such as the free electron laser, a small transverse emittance is required. In beams where a smaller longitudinal emittance is available, the two can be swapped by emittance exchange.

2.3 Emittance exchange line

The transverse-to-longitudinal emittance exchange line has been of considerable interest for high-brightness beams. The configuration at A0 was suggested by Emma, *et al*, in 2006 [19] as a variant of that of Cornacchia and Emma in 2002 [20]. A0PI has subsequently performed a proof-of-principle experiment of the emittance exchange technique along with its applications to bunch shaping [12–14]. We now briefly describe the effect of the EEX line on the incoming beam.

The EEX line couples the behavior between coordinates in the $x - z$ plane, so we do not consider the motion of the y phase space. In the remaining 4D basis and under the thin lens approximation, one finds that the single-particle transfer matrix $\mathbf{M}_{EEX}$ for the combined elements in the EEX line (Fig. 2.1) with an appropriately chosen strength of the deflecting mode cavity reduces to [12]

$$\begin{pmatrix} x_f \\ x'_f \\ z_f \\ \delta_f \end{pmatrix} = \begin{pmatrix} 0 & 0 & -\frac{1}{\alpha}\left(1+\frac{l}{L}\right) & -\alpha l \\ 0 & 0 & -\frac{1}{\alpha L} & -\alpha \\ -\alpha & -\alpha l & 0 & 0 \\ -\frac{1}{\alpha L} & -\frac{1}{\alpha}\left(1+\frac{l}{L}\right) & 0 & 0 \end{pmatrix} \begin{pmatrix} x_i \\ x'_i \\ z_i \\ \delta_i \end{pmatrix} \tag{2.15}$$

This is written in the form $\mathbf{r}_f = \mathbf{M}_{EEX}\mathbf{r}_i$ where $\mathbf{r}_i$ is the initial coordinate, $\mathbf{r}_f$ the position after the EEX line and with L the distance between the dipoles in each of the two doglegs, l half the distance between the doglegs and α the bending angle of the dipoles, as shown in Fig. 2.3.

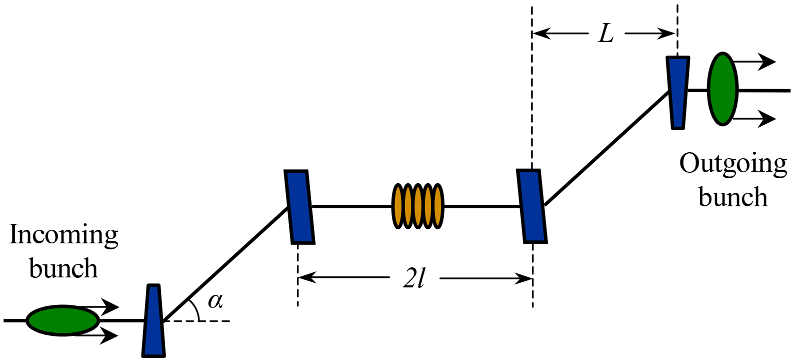

Figure 2.3: Geometry of the emittance exchange beam line. With appropriate choice of settings for the transverse deflecting mode cavity (center), the transfer matrix creates a map between phase space coordinates $(x, x') \leftrightarrow (z, \delta)$.

As the form of the transfer matrix is totally anti-block diagonal, we see that the transverse x phase space maps to the longitudinal z space and vice versa. This implies that with proper tuning one may rotate an elongated bunch in the coordinate $x - z$ space, as shown in Fig. 2.3.

This process is also sometimes referred to as "phase space exchange." In general only the emittance, related to the area of the phase space, should undergo a 1:1 exchange in $x \leftrightarrow z$ in the linear approximation. The precise form of how the individual particles swap then depends on the above transformation.

This property of transverse-to-longitudinal EEX is advantageous in a free-electron laser where one desires a small transverse emittance. The small longitudinal emittance of a compressed beam can then in principle be exchanged to produce a smaller transverse emittance as needed.

Alternatively pulse compression can also be achieved in EEX by adjusting the beam focusing upstream of the emittance exchanger. This change in the incident $x - x'$ distribution can be optimized to produce a minimum in the outgoing temporal width.

Extending beyond compression, one can use EEX to shape the outgoing longitudinal profile [21]. Here one imparts a modulation to the horizontal beam distribution which becomes a longitudinal modulation after EEX. This can be accomplished by masking the beam, as has been demonstrated [14]. We ultimately use system developed here to study a variation on the longitudinal modulation process previously performed.

In all of these cases, a shot-to-shot monitor of the outgoing longitudinal profile is helpful for rapid tuning and monitoring of the beam. The profiles generated are expected to have structure on the order of 1 ps or less, so high time resolution is also required. Beyond the obvious advantage in acquisition speed, single-shot measurements can also provide a benefit over fast multi-shot or integrating techniques by avoiding the accumulation of statistical error that can effectively wash out the temporal resolution.

2.4 Transition radiation

As stated in the introduction, information about the electron distribution can be inferred by observation of a radiative process in the beam line. From Eq. (1.1) we note that far from the beam, the dominant field component is related to the radiative $\dot{\boldsymbol{\beta}}$ term whenever there is a change in trajectory. Using Eq. (1.1) we can estimate the field $\mathbf{E}(\mathbf{r} - \mathbf{r}')$ that would be observed at the distant point $\mathbf{r}$ for a single electron located at point $\mathbf{r}'$. Jefimenko's equation (1.4) then describes the radiation from the bunch as the 3D convolution of this response function with the bunch distribution $\rho(\mathbf{r}')$.

In our experiment the diagnostic signal is generated by colliding the beam with an aluminized target located at diagnostic cross X24 (Fig. 2.1). As the relativistic electrons undergo the rapid transition from vacuum to metal, it emits a burst of what is referred to as transition radiation (TR).

2.4.1 Single-electron transition radiation response

In the approximation derived by Ginzburg and Frank [22, 23], the response is modeled as an electron encountering an infinite conductive plane. They regard the phenomenon using the method of images with the negative charge approaching its positive image in the opposite half-space defined by the conductor to satisfy that the potential remain zero across the surface. The moment of collision corresponds to an infinite deceleration of infinitesimal duration as the two annihilate so that the $\dot{\beta}$ of Eq. (1.1) can be regarded as a Dirac delta function directed counter to the initial velocities. The resulting spectral intensity distribution is found to be radially polarized with observed intensity [7, 8, 22, 23]

$$\left|\mathbf{E}_e\right|^2 (\omega,\ R,\ \theta) = \frac{e^2\beta^2 \sin^2\theta}{4\pi\epsilon_0 c R^2 \left(1-\beta^2\cos^2\theta\right)^2} \tag{2.16}$$

where e is the electron charge, β is the relativistic velocity factor, θ the polar observation angle, and R the observation distance with $R \gg \gamma\lambda$. The distribution is rotationally symmetric and therefore takes the form of a hollow cone with the maximum occurring at a half-opening angle of $\theta_{TR} = 1/\gamma$ [8], where γ is the relativistic factor of the beam. (In our case $\gamma \approx 32$ so that $\theta_{TR} \approx 2°$.) The intensity is constant in frequency, corresponding to the delta function in time.

The image charge approach for the more general case of oblique incidence at an infinite, perfectly conducting foil is shown in Fig. 2.4. As noted by [24, 25], this can be described using the rapidly accelerated image charge approach. The trajectory of the image charge is chosen to be the mirror of the incident electron to maintain zero potential across the interface. Immediately upon striking the foil, the image must change trajectories to match the electron to maintain charge neutrality within the conductor. Where the duration of the interaction is very short compared to the wavelength observed, the radiative fields can then be calculated using Jackson's description of scattering and bremsstrahlung [7, 24, 25].

A conical distribution similar to that of the Ginzburg-Frank formula (2.16) is emitted in the forward direction of image charge incidence $\boldsymbol{\beta}_{+,1}$ (backward TR) and then in the direction of the reflected trajectory $\boldsymbol{\beta}_{+,2}$ as the inverse process occurs on the opposite face of the foil (forward TR), but with some asymmetry

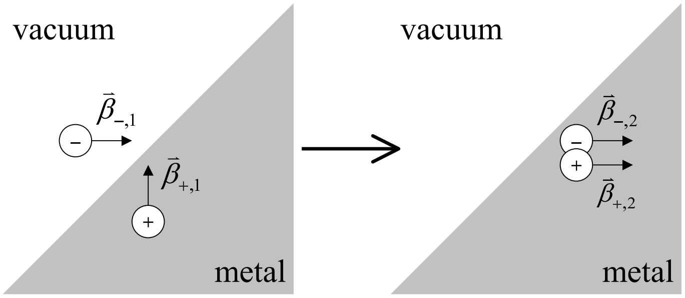

Figure 2.4: Illustration of method of images approach to transition radiation. Before the electron strikes the foil (left), the image charge mirrors the incident electron. After crossing the boundary (right), the image charge co-propagates with the electron. TR is generated by the effectively instantaneous acceleration of the image at the boundary.

in the direction of the plane of incidence. Far from the collision point, again with $R \gg \gamma\lambda$, the intensity can be written as [7]

$$\left|\mathbf{E}_e\right|^2(\omega,\ \mathbf{R}) = \frac{e^2}{16\pi\epsilon_0 c R^2}\left|\frac{\boldsymbol{\beta}_{+,2}\times\hat{R}}{1-\boldsymbol{\beta}_{+,2}\cdot\hat{R}} - \frac{\boldsymbol{\beta}_{+,1}\times\hat{R}}{1-\boldsymbol{\beta}_{+,1}\cdot\hat{R}}\right|^2 \tag{2.17}$$

where $\mathbf{R}$ is the vector to the observation point, assuming the transition occurs at the origin. In the case of normal incidence $\boldsymbol{\beta}_{+,2} = -\boldsymbol{\beta}_{+,1}$, this reduces to the Ginzburg-Frank form of Eq. (2.16).

For typical beams, the far-field condition $R \gg \gamma\lambda$ can be easily met for optical wavelengths. However, for wavelengths emitted in the mm to sub-mm range, this can be violated for high-energy beams. The long wavelength also begins to compare with the diameter of the aluminum target introducing finite radiator effects that breakdown the infinite foil approximation. And for typical laboratory optics with tens-of-millimeter apertures, the subsequent propagation of such radiation is strongly effected by diffraction.

Attempts to account for both the finite size of the radiator and the diffraction losses incurred in the imaging optics have been explored by the accelerator community in recent years [25–32]. Our own model was developed [33, 34] based on the theory of virtual photons for modeling the emission of radiation at a metal interface [8] and the vector diffraction theory developed by Marathay and McCalmont [35] for the propagation of the THz waves.

In the virtual photon approach, the radiated field is approximated as the reflection of the Fourier components of the Lorentz-boosted Coloumb field. In polar coordinates with a relativistic electron at the origin the transverse, radial electric field $\widetilde{E}_r$ is [8, 25, 33]

$$\widetilde{E}_r(\omega,\ r,\ z) = \frac{q\omega}{(2\pi)^{3/2}\epsilon_0\beta^2c^2\gamma}K_1\left(\frac{\omega}{\beta c\gamma}\right)\exp\left(\frac{i\omega}{\beta c}z\right). \tag{2.18}$$

The propagation of this effective source is then treated by the chosen expression for scalar or vector diffraction. For example, following the treatment of [28], for scalar diffraction we apply the integral [7, 8]

$$\widetilde{\mathbf{E}}(k,\mathbf{r}) = \int_{S'} \widetilde{\mathbf{E}}(k,\mathbf{r}')\,\frac{e^{ikR}}{R}d^2r', \tag{2.19}$$

where $k = \omega/c$, $\mathbf{r}$ is again a distant observation point, $\mathbf{r}'$ a point on the surface of the aperture S', and $\mathbf{R} = \mathbf{r} - \mathbf{r}'$. This is simply the Huygens-Fresnel principle of secondary spherical waves. Closed-form solutions of this integral for arbitrary fields at an arbitrary distance are frustrated in most cases by the dependence on R, though numerical solutions and some approximations are straightforward.

In Fig. 2.5 we have computed numerically the spectral fluence as a function of polar observation angle ϕ for a $\gamma = 50$ electron at normal incidence to a 50-mm diameter metal target as seen at a distance of $R = 50$ mm using instead the more detailed vector diffraction expressions provided by [35]. This distance roughly corresponds to that from the foil to the diamond window in Fig. 2.6. Both the finite radiator and diffraction effects are observed at low frequencies as the amplitude decays weakly below $\nu \approx 0.5$ THz while simultaneously beginning to spread out in the transverse plane. For higher frequencies the peak angle converges, though in this near-field case $\theta_{TR} = 3.4°$, about three times larger than that predicted by (2.16).

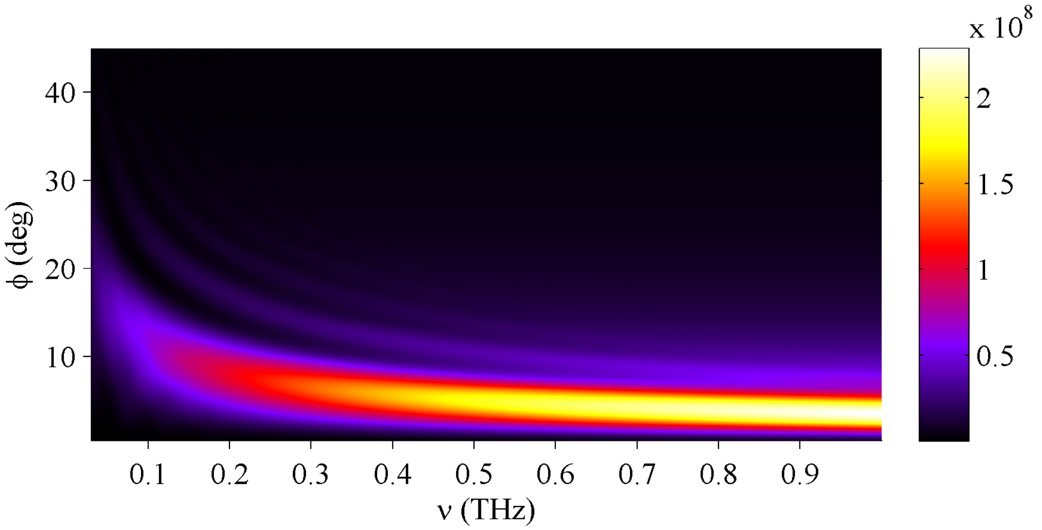

Figure 2.5: Spectral fluence [arbitrary units] as a function of polar observation angle ϕ for a $\gamma = 50$ electron at normal incidence to a 50-mm diameter metal target at a distance of $R = 50$ mm from the target.

As the solution provided by [35] preserves the vector nature of the light, repeated propagation through several optics can also be calculated. Such simulations were carried out for previous studies [34] to propagate the field through the imaging optics to the experimental observation point. Initial generation occurs in a 6-way vacuum cross by colliding the beam with an aluminized target, as depicted in Fig. 2.6. We compute the relative power transmission function $T(\nu)$ including effects from fractional emission at the foil, losses from partial transmission of the spatial distribution at the vacuum window, and partial integration over a 6-mm detection surface at the observation point. The resulting $T(\nu)$ is shown in Fig. 2.7.

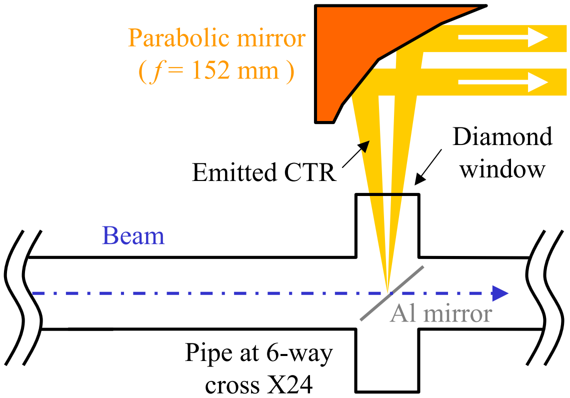

Figure 2.6: Emission of long-wavelength coherent transition radiation (CTR) from an aluminized target inserted 45°to the electron beam. The light leaves the vacuum pipe through a diamond window to be collimated for transport by a gold parabolic reflector.

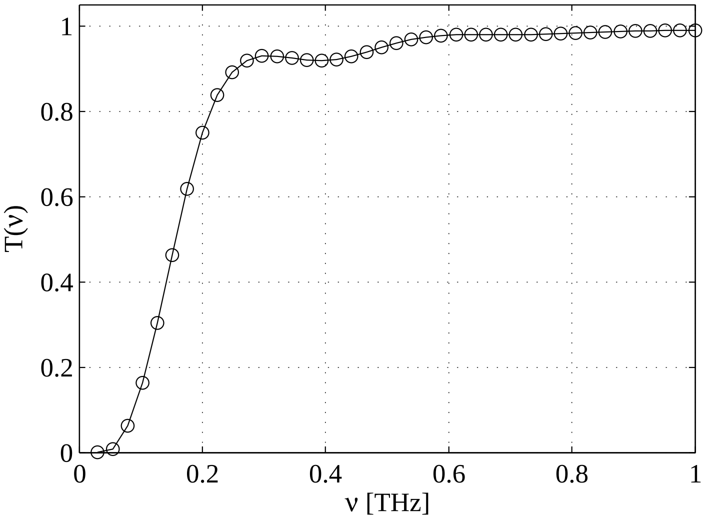

Figure 2.7: Simulated relative power transmission function $T(\nu)$ to a 6-mm diameter experimental observation point for transition radiation including finite foil and diffraction effects in optical system.

We see that the low frequency components in the tens-of-GHz regime are strongly suppressed. The transverse masking of the long wavelengths becomes an effective amplitude modulation in frequency. This complicates any measurements relying on the low-frequency spectrum of the TR.

2.4.2 Transition radiation of a bunch

The significance of the long-wavelength components comes to bear as many electrons strike the foil. By superposition we sum over all contributions to the total radiation field component $\mathbf{E}(k)$ of wavenumber $k = \omega/c$ from a distribution $\rho(z)$ normalized to unit charge e and bunch of total charge $Q = eN$ at the foil,

$$\mathbf{E}(k) = N \int_{-\infty}^{\infty} \mathbf{E}_e(k)\rho(z)e^{ikz}dz \tag{2.20}$$

where $\mathbf{E}_e(k)$ is the single-electron contribution to the image field at our observation point. The resulting measured intensity will be given by the modulus-squared. This is found to be [24]

$$I(k) = N(N-1)I_e(k)f(k) + NI_e(k) \tag{2.21}$$

where we have introduced the 1D bunch form factor $f(k)$

$$f(k) = \left| \int_{\infty}^{-\infty} \rho(z)e^{ikz}dz \right|^2 . \tag{2.22}$$

This is the modulus-square of the Fourier transform of the bunch distribution. The first term in Eq. (2.21) is proportional to both $f(k)$ and N^2. It becomes dominant in the regime where the wavelength is longer than the duration of the bunch. Physically it describes the TR of the individual electrons being radiated approximately in phase with each other creating a coherent enhancement. Therefore this is referred to as the coherent transition radiation (CTR) with spectral components ideally given by

$$\widetilde{E}_{CTR}(k) \propto \int_{-\infty}^{\infty} \rho(z)e^{i\,kz}dt \tag{2.23}$$

For compact electron beams with bunch lengths on the order of a few picoseconds and smaller as at A0PI, this then implies coherent emission into the THz regime. Of course, the effect of diffraction losses that can be introduced via the single electron transfer spectrum $E_e(k)$ as discussed in Sec. 2.4.1 then also need to be taken into account.

For the coherent portion of the spectrum, this is attractive to the high-brightness accelerator community as, among other things, a longitudinal diagnostic tool. One can in principle measure the power spectrum of the emitted radiation which is the modulus-squared of (2.23). This can be a strong signal for bright beams as the intensity of this portion of the spectrum scales with the square of the total bunch charge. At the very least an estimate of the bunch duration can be inferred by the inverse of the bandwidth of the measured spectrum.

Further, spectral techniques in conjunction with reconstruction algorithms can recover the phase information lost by measuring the modulus-squared of the distribution's Fourier transform with some success (c.f., [36]). From this additional temporal profile information is inferred. Fortunately the technique developed here is regarded as a sign-resolving time-domain approach, as we will see in Sec. 4.1, allowing one to circumvent the need for such reconstruction.

In the optical range wavelengths become much shorter than our bunch length. This is the incoherent regime and is referred to as optical transition radiation (OTR). When using ordinary optical detectors, there is little time-frequency correlation in the light observed. We extend Eq. (2.22) to the two-dimensional case and preserve only the second, incoherent term. In this case we define a charge distribution that can be decoupled in time $t \approx z/c$ and transverse vector $\mathbf{r}_\perp$ as

$$\rho(\mathbf{r}) = N\rho_t(t)\rho_\perp(\mathbf{r}_\perp) \tag{2.24}$$

with ρ_t and $\rho_\perp$ again normalized to a unit charge e so the total bunch charge is $Q = Ne$. The second, incoherent term of (2.22) becomes [24, 26, 32]

$$I_{incoh}(\mathbf{r}_\perp, t) = N\rho_t(t) \int_{S'} \left|\mathbf{E}_e(\mathbf{r} - \mathbf{r}')\right|^2 \rho_\perp(\mathbf{r}'_\perp) d^2 r'_\perp. \tag{2.25}$$

For optical wavelengths we note the 2D convolution of the transverse distribution with the effective point spread function given by the intensity that would be seen for the imaging of a single electron via $|E_e|^2$. Using an ordinary imaging system and camera we can therefore produce an image of the beam subject to the spatial resolution imposed by this effective transfer function. In the optical regime and using an ordinary imaging lens of focal length f and radius a, it has been shown that where $\gamma \gg a/f$ that the FWHM spatial resolution Δr is [26]

$$\Delta r \approx 1.44\frac{\lambda f}{a}. \tag{2.26}$$

In the optical regime, resolution on the order of microns is regularly achieved.

2.5 Existing diagnostics

We now describe some relevant conventional diagnostics installed at A0PI used for these experiments. The first is a longitudinal bunch distribution measurement that, like the diagnostics developed here, are sensitive to the millimeter-wave CTR. Alternatively, the incoherent OTR pulses can be sent to the time-resolved streak camera to determine their duration. And finally, by transverse imaging of the OTR with an ordinary CCD camera, a technique to determine the beam profile and divergence will be described.

2.5.1 Martin-Puplett Interferometer

The Martin-Puplett interferometer at A0PI [37] is an existing longitudinal bunch distribution diagnostic that is also based on probing the CTR transient E_{THz}. This is accomplished by measuring the total power of the interference pattern generated by the signal $E_{THz}(t)$ and its time-delayed replica $E_{THz}(t-\tau)$. This is a slow, multi-shot technique requiring that the delay τ be stepped between successive measurements and assumes that the bunch structure remains stable between shots. One complete scan takes about 15 to 20 minutes to complete, emphasizing the appeal of real-time, single-shot measurements. A recent thorough analysis of such a system is given, e.g., in [38].

To generate the interferogram, the incoming signal E_{THz} is split by a wire mesh polarizer at 45°to the vertical polarization of the incident light. One pulse traverses a path with a delay that is variable relative to the other before recombining. This is again split by a vertical polarizer. The two resulting signals are then focused onto a pair of pyroelectric detectors sensitive to the mid-IR wavelengths, as illustrated in Fig 2.8.

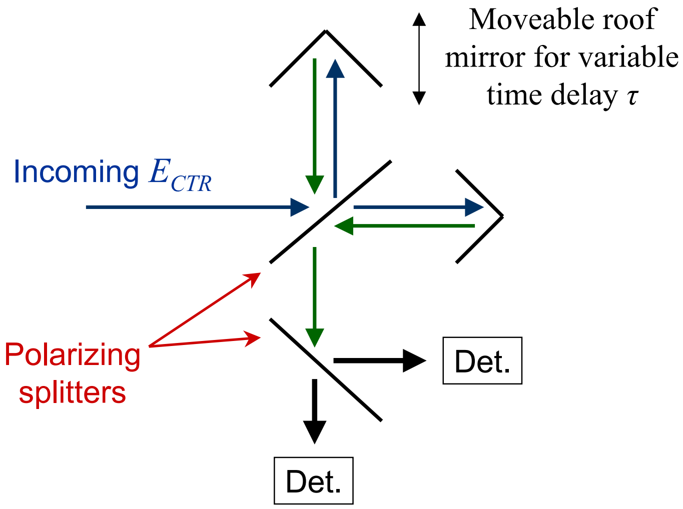

Figure 2.8: Optical layout for a Martin-Puplett interferometer. See text for complete description.

Taking the difference of the integrated power seen by the two detectors divided by their sum yields an interferogram (IF) that, when assuming real $E_{THz}(t)$, can be expressed in the time domain as

$$IF(\tau) \propto \int_{-\infty}^{\infty} \left| E_{THz}(t) + E_{THz}(t-\tau) \right|^2 dt \tag{2.27}$$

$$= 2\int_{-\infty}^{\infty} \left| E_{THz}(t) \right|^2 dt + 2\int_{-\infty}^{\infty} E_{THz}(t) E_{THz}(t-\tau) dt. \tag{2.28}$$

This is the form of the autocorrelation of the signal E_{THz} plus a DC offset related to the integrated power of the pulse.

The width of the IF is therefore directly proportional to the bunch length within a scaling factor determined by the bunch shape and subject to similar low-frequency diffraction losses as described in Sec. 2.4. As a frequency-domain technique, the phase information required to directly deduce the E_{THz} is lost. This can be recovered to some degree by applying the Kramers-Kronig relations [36, 39, 40].

However, the diagnostics developed here in principle recover the profile E_{THz} directly, including sign. From this data we can forward compute a theoretically equivalent interferogram using (2.27) and compare results to those measured by the interferometer. In this way the interferometer will be used to provide an independent measurement, testing the consistency of the new single-shot diagnostics.

2.5.2 Streak Camera

Where a very broad bandwidth of the optical spectrum can be collected, Eq. (2.25) shows that a weak temporal modulation related to the original bunch duration should be observed for even the incoherent part of the spectrum. Measurement of this sort incoherent temporal profile requires a highly sensitive time-resolved measurement of the pulse that's insensitive to incident wavelength.

The streak camera is such a fast, time-resolved imaging system, ordinarily used for bunch length measurements at A0PI [41–43] by imaging the incoherent OTR from the beam with reflective optics. A simple schematic of streak camera operation is shown in Fig. 2.9. The light pulse is incident on the entrance slit of the unit and imaged to a photocathode. The photoelectrons generated are subject to a small accelerating field. These are subsequently deflected by an alternating electric field to sweep out the pulse, introducing a spatio-temporal correlation. As there are very few photoelectrons, the pulse then strikes a microchannel plate to multiply them before they collide with a phosphor screen. The resulting optical pulse is imaged to a camera. Depending on the amplitude and phase of the applied deflecting field, the temporal structure of the original light pulse is thereby imaged in the transverse plane.

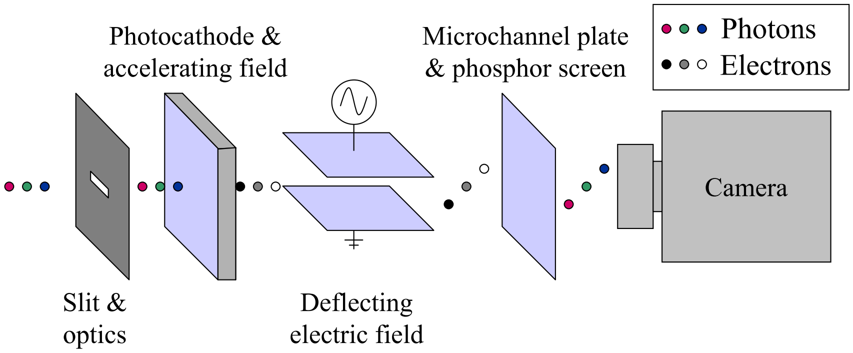

Figure 2.9: Schematic overview of streak camera operation showing signal propagation from left to right. A light pulse is incident on the slit and imaging optics, striking the photocathode under a small accelerating field to produce electrons. These are deflected by an alternating gradient to sweep out the pulse, introducing the spatio-temporal correlation. The electrons then strike a microchannel plate to multiply the electrons before striking a phosphor screen. The resulting optical pulse is imaged to a camera.

The sweep unit that generates the alternating deflecting field is equipped with synchroscan and phase lock loop (PLL) electronics to maintain synchronization with the 81.25-MHz subharmonic of the A0PI master oscillator [41]. To adjust temporal range and resolution the sweep rate is adjusted which changes the amplitude of the deflecting field to increase or decrease the magnitude of the deflecting kick. Four settings are available with the fastest sweep range, referred to as range 1, having a single-sweep resolution of 540 fs RMS with the next-fastest sweep rate (range 2) having a temporal resolution of 2.5 ps.

As the streak camera sweep unit is phase locked to the RF, it is also used in this analysis to perform synchronization measurements by tracking the centroid of images. In principle, if the sweep unit is perfectly synchronized the accelerator RF, light generated by the beam should always be imaged to the same screen position. In practice the standard deviation of shot-to-shot changes in streak image position from tracking a similarly phase-locked laser pulse train is typically found to be $\sim$1 pixel. This corresponds to 320 fs in sweep range 1 and 1.5 ps in range 2.

Besides the time resolution introduced by imaging and the electronics, pulse integration can also dilute the resolution when determining the duration of a single streak image. Such pulse stacking is frequently used when making measurements of the relatively weak OTR pulses. Where a train of pulses enters the camera, each is stacked onto roughly the same screen position and their intensities summed, generating more light from the phosphor screen. However, as this is not a truly single-shot approach, timing fluctuations in the signal or sweep unit over the scale of several RF cycles cause a broadening of the stacked images on the screen. This can therefore degrade single-image temporal resolution as one approaches measurements on the order of the system stability.

2.5.3 Emittance measurement

For longitudinal emittance measurements in the straight-ahead line (Fig. 2.1), bunch length is determined by streak camera using OTR from X09. A Gaussian fit to the streaked image is used to determine $\langle z^2 \rangle$.

The mean beam momentum and fractional momentum spread are determined in the spectrometer at the end of the line. Upstream horizontal focusing is used to produce the minimum width in the energy direction on a camera image of the spectrometer OTR screen. Again a Gaussian fit is used to determine the energy spread $\langle \delta^2 \rangle$.

When measuring the longitudinal emittance, the beam is tuned to produce an up-right phase space as inferred by minimizing the total fractional momentum spread observed in the spectrometer. In the absence of correlations between z and δ the emittance can then be found from the measured widths by

$$\epsilon_z^* \approx \beta\gamma \sqrt{\langle z^2 \rangle \langle \delta^2 \rangle} \tag{2.29}$$

where β and γ are the relativistic factors, computed from the mean momentum determined in the spectrometer.

In the transverse directions, the multi-slit method is used [12, 44–46]. An image of the beam is taken from an OTR screen inserted just after the booster cavity in Fig. 2.1. This provides the transverse distribution in that plane. The screen is removed and a tungsten mask with either horizontal or vertical slits is inserted in the beam to generate beamlets. 0.8 m upstream of the slits another OTR screen is inserted to capture an image of the beamlets, as illustrated from a side view in Fig. 2.10.

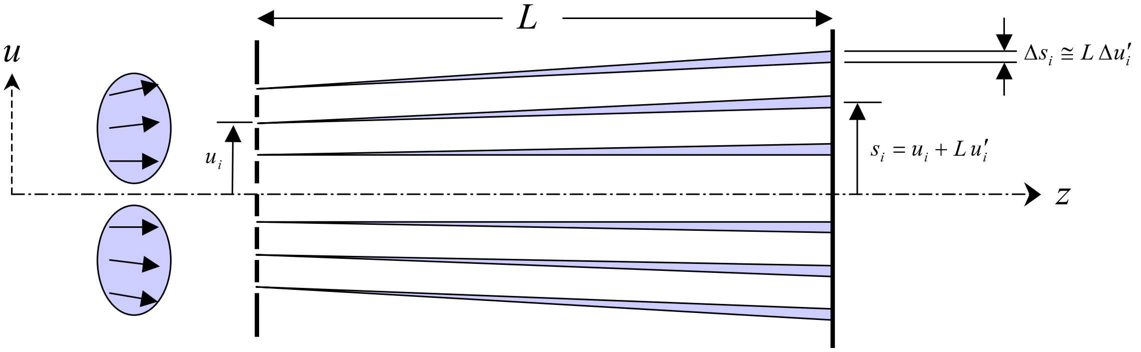

Figure 2.10: Geometry for transverse emittance measurement by the slit method.

Assuming negligible space charge so that the contribution from divergence dominates, the beamlets produced will individually deviate from the axis at the rate given by the divergence u_i' at the associated i-th slit position u_i. They will also individually broaden at the rate given by the uncorrelated beam divergence Δu_i. By measuring the positions s_i and widths Δs_i of the beamlet associated with the i-th slit, one can infer the points in the beam sampled by the slits as

$$u_i' = \frac{s_i - u_i}{L} \tag{2.30}$$

$$\Delta u_i \approx \frac{\Delta s_i}{L} \tag{2.31}$$

The expression for Δu_i is only approximately true as the initial finite width of the slit will also contribute to the width of the beamlet observed downstream. Where the slit width w is much smaller than the measured beamlet width, this can be neglected. As they become similar, one can make minor corrections by subtracting the slit width in quadrature from the measured width so that Eq. (2.31) becomes

$$\Delta u_i \approx \sqrt{\left(\frac{\Delta s_i}{L}\right)^2 - w^2} \tag{2.32}$$

The effect of a drift on the ellipse is a shearing in the spatial direction [17]. An illustration of this and how the sampled values s relate to the phase space ellipses in u are shown in Fig. 2.11 for the spatially masked distribution. The spread in u is therefore known from the image taken of the beam in the slit plane. The slope of the correlated divergence can be determined by a fit through the sampled $x_i'(x_i)$ with the uncorrelated divergence spread determined via Eq. (2.31). This is sufficient to fully define a phase space ellipse in the plane of the slits and determine the Courant-Snyder parameters and emittance there.

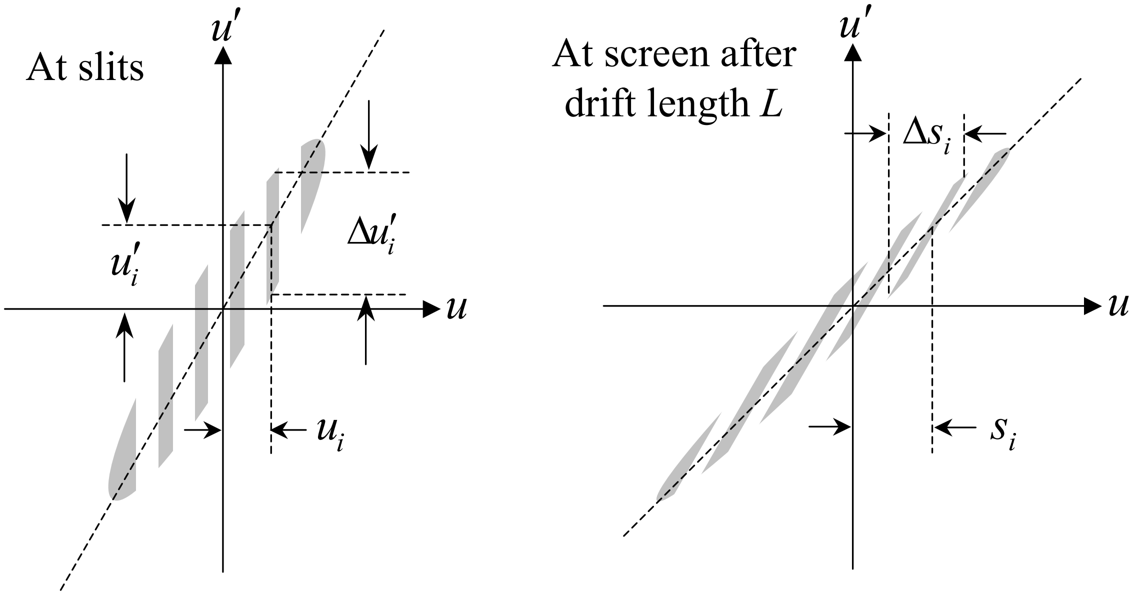

Figure 2.11: Transverse phase space ellipses for the slit measurement with parameters shown corresponding to those illustrated in Fig. 2.10. (Left) shows the ellipse immediately after being masked. (Right) shows the shearing of the ellipse from the drift of length L and the measured beamlet positions s_i and widths Δs_i.

2.6 Ellipsoidal bunch

As it effects details on the installation of the Ti:sapph laser used as an ultra-fast probe for our diagnostics, we note that the system was chosen to alternatively drive the formation of ellipsoidal bunches in the "blow-out regime" [47–49]. Ellipsoidal bunch distributions have the desirable quality of minimizing the growth of the phase space under the repulsive Coulomb force referred to as the space charge effect as these internal forces remain linear for ordinary beam propagation.

The distribution is generated by utilizing space charge itself during the process of bunch formation inside the RF gun. When a very short duration laser pulse strikes the photocathode, a thin pancake distribution of charge is emitted. This distribution is initially low energy prior to full acceleration. In the laboratory frame, one finds that the space charge effect causes the dense bunch to expand, generating an ellipsoidal distribution [47]. This distribution is then effectively frozen in the laboratory frame by the final acceleration stage.

Results of ASTRA simulations [50] for this process are shown in Fig. 2.12 for a drive laser pulse with a root-mean-squared (RMS) duration of 200 fs and 100 pC of total bunch charge after both the RF gun (beam energy $E = 4$ MeV) and booster cavity (15 MeV). Each time-projection is plotted in comparison of the temporal profile of the laser used to drive photoemission. The expansion of the bunch from the originating laser duration is apparent, as is the parabolic temporal profile expected for a bunch that is a 3-dimensional ellipsoid.

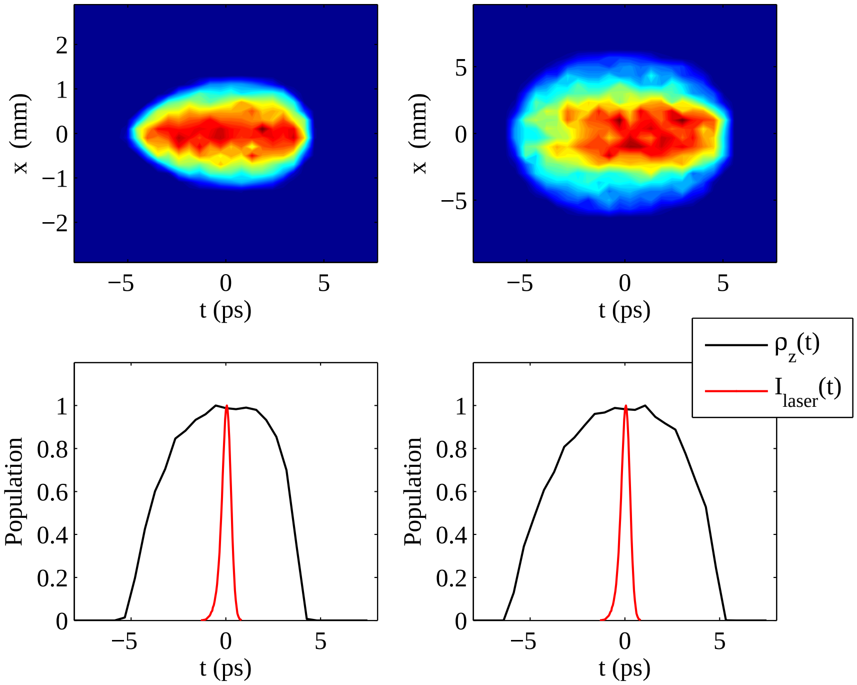

Figure 2.12: ASTRA simulation of ellipsoidal bunch formation in the blow-out regime at A0PI showing the resulting $x - t$ distribution (top) and temporal profile (bottom) for a 100 pC after the RF gun (left) and booster cavity (right). Profiles are compared to the 200-fs (RMS) laser pulse used for the simulation.

The titanium-sapphire laser installed is capable of generating the requisite ultra-short pulse. In this case the amplified 800-nm infrared (IR) laser output must be frequency tripled to the ultraviolet (UV, 266 nm) as required for photoemission from our Cs_2Te photocathode, then delivered to the accelerator tunnel.

Many of the demands regarding machine synchronization and delivery of the laser pulse to the accelerator tunnel overlap for these experiments. Therefore, where it impacts the design of our installation, we will also mention related details on the alternative use of the newly requisitioned Ti:sapph system as an ultra-short photoinjector drive laser.

CHAPTER 3

OPTICAL THEORY

The diagnostic method used here will employ the use of a broadband laser pulse to act as an ultra-fast probe of the CTR from the beam. We have also just mentioned the alternate use of this laser to generate a short drive laser pulse for the photoinjector. Pursuant to these applications, some basic laser science is needed.

It is helpful to begin with the description of some fundamental optics then, as much for the sake of review as detailing our notation and assumptions. A variety of descriptions for all of the following basic phenomena are available in the standard texts. Even in these cases, we frame things by the same first principles to connect the terminology in a meaningful way. This will also ultimately demonstrate the systematic approach to nonlinear optics problems that we will use to describe the measurement of the CTR.

Management and diagnosis of a broadband, coherent laser pulse is most strongly linked to behavior in the time-frequency domain. For simplicity we constrain ourselves to the time-frequency analysis of our optical wave beam for ultra-fast optics in general. This is analogous to the study of the one-dimensional, longitudinal dynamics in the vernacular of particle beam physics.

We start with the general wave equation and solution for free-space propagation of an electromagnetic field. For the infinite plane wave-case we can then describe the temporal and spectral properties of a broadband pulse. Dispersion in amorphous glass is then explained with a simple example of laser pulse broadening. Linear birefringence in a medium is presented leading to the tensor and Jones calculus formalisms for polarization analysis along with the example of bulk wave plates. Many recurring terms used in ultra-fast and nonlinear optics will then be established.

3.1 The wave equation

All of the problems described in this chapter reduce to the solution of freely propagating electromagnetic waves interacting with a given medium. We therefore begin by closely following the familiar treatments presented in [51, 52].

In the absence of any free charge, the differential form of Maxwell's equations in a medium are

$$\nabla \cdot \mathbf{D} = 0 \tag{3.1}$$

$$\nabla \cdot \mathbf{B} = 0 \tag{3.2}$$

$$\nabla \times \mathbf{E} = -\frac{\partial \mathbf{B}}{\partial t} \tag{3.3}$$

$$\nabla \times \mathbf{H} = \frac{\partial \mathbf{D}}{\partial t} \tag{3.4}$$

with the electric displacement **D**, magnetic field **B**, electric field **E** and magnetizing field **H**. In the context of nonlinear optics, we assume all solutions are in nonmagnetic materials with relative permeability $\mu = 1$ so that

$$\mathbf{B} = \mu_0 \mathbf{H} \tag{3.5}$$

where μ_0 is the permeability of free space. However, the dielectric displacement takes the general form

$$\mathbf{D} = \epsilon_0 \mathbf{E} + \mathbf{P} \tag{3.6}$$

where ϵ_0 is the permittivity of free space and the induced polarization **P** in general can depend linearly or nonlinearly on the local electric field **E**, depending on the interactions allowed by the material within which the electromagnetic wave propagates. In sections to follow, we will consider several types of materials and how they relate **E** to **P**.

By differentiation and substitution of Eq. (3.1)- (3.4) and using $\mu_0 = 1/\epsilon_0 c^2$, we arrive at the general wave equation

$$\nabla \times \nabla \times \mathbf{E}_t(\mathbf{r}) + \frac{1}{c^2}\frac{\partial^2 \mathbf{E}_t(\mathbf{r})}{\partial t^2} = -\frac{1}{\epsilon_0 c^2}\frac{\partial^2 \mathbf{P}_t(\mathbf{r})}{\partial t^2} \tag{3.7}$$

where we use the subscript to denote $\mathbf{E}_t(\mathbf{r}) = \mathbf{E}(\mathbf{r},\ t)$.

We can also write $\mathbf{E}_t\left(\mathbf{r}\right)$ in terms of its Fourier decomposition everywhere in space.

$$\mathbf{E}_t\left(\mathbf{r}\right) = \frac{1}{\sqrt{2\pi}} \int_{-\infty}^{\infty} \widetilde{\mathbf{E}}_\omega\left(\mathbf{r}\right) e^{-i\omega t} d\omega \tag{3.8}$$

As $\mathbf{E}_t(\mathbf{r})$ is a real, measurable quantity and related to $\widetilde{\mathbf{E}}_\omega(\mathbf{r})$ by inverse Fourier transform, it is necessary that

$$\widetilde{\mathbf{E}}_{-\omega}\left(\mathbf{r}\right) = \widetilde{\mathbf{E}}^*_\omega(\mathbf{r}) \tag{3.9}$$

From this, we note a frequently used alternative convention [51] where Eq. (3.8) is written in the form of integrating over only positive frequencies and adding the complex conjugate. The temporal field is written by first splitting (3.28) into positive and negative components.

$$\mathbf{E}_t(\mathbf{r}) = \frac{1}{\sqrt{2\pi}} \left\{ \int_{-\infty}^{0} \widetilde{\mathbf{E}}_\omega(\mathbf{r}) e^{-i\omega t} d\omega + \int_{0}^{\infty} \widetilde{\mathbf{E}}_\omega(\mathbf{r}) e^{-i\omega t} d\omega \right\} \tag{3.10}$$

Using the change of variable $\omega \to -\omega$ in the first integral,

$$\mathbf{E}_t(\mathbf{r}) = \frac{1}{\sqrt{2\pi}} \left\{ \int_{0}^{\infty} \widetilde{\mathbf{E}}_{-\omega}(\mathbf{r}) e^{i\omega t} d\omega + \int_{0}^{\infty} \widetilde{\mathbf{E}}_\omega(\mathbf{r}) e^{-i\omega t} d\omega \right\} \tag{3.11}$$

and inserting (3.9), we have

$$\mathbf{E}_t(\mathbf{r}) = \frac{1}{\sqrt{2\pi}} \int_{0}^{\infty} \widetilde{\mathbf{E}}_\omega(\mathbf{r}) e^{-i\omega t} d\omega + \text{c.c.} \tag{3.12}$$

where c.c. denotes the complex conjugate of the first term in the sum.

We will see that the presence of both positive and negative frequency components and assertion of their being related by (3.9) has several implications which will become important later in discussion of sum- and difference-frequency generation. It further allows us to break (3.12) into two components as

$$\mathbf{E}_t(\mathbf{r}) = \frac{1}{2} \left[\widetilde{\mathbf{E}}_t(\mathbf{r}) + \widetilde{\mathbf{E}}^*_t(\mathbf{r}) \right] \tag{3.13}$$

where a complex temporal field is then given by the sum over only positive frequencies

$$\widetilde{\mathbf{E}}_t(\mathbf{r}) = \sqrt{\frac{2}{\pi}} \int_{0}^{\infty} \widetilde{\mathbf{E}}_\omega(\mathbf{r}) e^{-i\omega t} d\omega \tag{3.14}$$

This complex temporal solution can be useful, for example, in describing the slowly varying envelope of an optical pulse, as we will see in Sec. 3.2.3.

Returning to the wave equation, we insert our expansions (3.8) back into (3.7) to find in the frequency domain defined above

$$\nabla \times \nabla \times \widetilde{\mathbf{E}}_\omega(\mathbf{r}) - \frac{\omega^2}{c^2}\widetilde{\mathbf{E}}_\omega(\mathbf{r}) = \frac{\omega^2}{\epsilon_0 c^2}\widetilde{\mathbf{P}}_\omega(\mathbf{r}) \tag{3.15}$$

The double curl terms in both (3.7) and (3.15) can be expanded identically as

$$\nabla \times \nabla \times \mathbf{E} = \nabla\left(\nabla \cdot \mathbf{E}\right) - \nabla^2\mathbf{E} \tag{3.16}$$

When **D** is linear in **E**, the first term on the right hand side of Eq. (3.16) will vanish as we are using a charge-free description. However, for the more general nonlinear case this is not true. As Boyd points out [51], this term still vanishes identically under the infinite plane wave approximation or can be made negligible under the slowly-varying amplitude approximation. We will introduce these explicitly as necessary later, but when such approximations can be made (3.7) and (3.15) simplify to

$$\nabla^2\mathbf{E}_t(\mathbf{r}) - \frac{1}{c^2}\frac{\partial^2\mathbf{E}_t(\mathbf{r})}{\partial t^2} = \frac{1}{\epsilon_0 c^2}\frac{\partial^2\mathbf{P}_t(\mathbf{r})}{\partial t^2} \tag{3.17}$$

$$\nabla^2\widetilde{\mathbf{E}}_\omega(\mathbf{r}) + \frac{\omega^2}{c^2}\widetilde{\mathbf{E}}_\omega(\mathbf{r}) = -\frac{\omega^2}{\epsilon_0 c^2}\widetilde{\mathbf{P}}_\omega(\mathbf{r}) \tag{3.18}$$

Solutions to this equation can be used to describe a number of physically interesting cases. To find these solutions, one must make appropriate choices for the induced polarization **P** (dependent on the electronic properties and symmetry of the medium) with the initial conditions set by the wave incident at the medium's boundary.

3.2 Free-wave solution and 1D description of an optical pulse

The most straightforward solution to Eq. (3.7) is found in vacuum where, in the absence of a medium, $\mathbf{P} = 0$ and Eq. (3.18) is exactly true becoming

$$\nabla^2\widetilde{\mathbf{E}}_\omega\left(\mathbf{r}\right) = \frac{-\omega^2}{c^2}\widetilde{\mathbf{E}}_\omega\left(\mathbf{r}\right) \tag{3.19}$$

Eq. (3.19) is still of a very general form. In conjunction with the same solution for **B**, it describes the source-free propagation of an electromagnetic wave. The initial wave should be regarded as the boundary conditions imposed on the above differential equations. The general solution of this formula is highly complex for arbitrary initial conditions, that is to say, for any given incident wave. Describing free propagation of light, the general solution leads to the subject of vector diffraction.

We note, however, that the solution with spatial dependence

$$\widetilde{\mathbf{E}}_\omega\left(\mathbf{r}\right) = \widetilde{\mathbf{E}}_\omega e^{i\,\mathbf{k}\cdot\mathbf{r}} \tag{3.20}$$

satisfies Eq. (3.19) where $\mathbf{k} = (\omega/c)\,\hat{k}$, $\hat{k}$ being the direction of propagation, and $\widetilde{\mathbf{E}}_\omega \perp \hat{k}$ [52]. (In principle $k\ =\ -\omega/c$ is also a solution, but we assume the initial conditions on the derivative of $\widetilde{\mathbf{E}}_\omega$ are chosen such that the positive case is valid.)

In general **k** and $\widetilde{\mathbf{E}}_\omega$ still depend on all three spatial coordinates. We can further restrict ourselves to the infinite plane wave solution where $\widetilde{\mathbf{E}}_\omega$ is everywhere uniform and $\hat{k} = \hat{z}$. Then (3.20) reduces to

$$\widetilde{\mathbf{E}}_\omega(z) = \widetilde{\mathbf{E}}_\omega e^{ikz} \tag{3.21}$$

In our context this is selecting the solution meeting the boundary conditions for a spatially uniform electric field $\mathbf{E}_t(z = 0)$ with vector components only in the $z = 0$, $x - y$ plane. To clarify, we solve explicitly for the time evolution of $\mathbf{E}(z, t)$ in this somewhat unremarkable case.

Inserting (3.21) back into (3.8), we find

$$\mathbf{E}_t(z) \quad = \quad \frac{1}{\sqrt{2\pi}}\int_{-\infty}^{\infty}\widetilde{\mathbf{E}}_\omega(0)e^{ikz}e^{-i\omega t}d\omega \tag{3.22}$$

From (3.8) we find

$$\widetilde{\mathbf{E}}_\omega(0) = \frac{1}{\sqrt{2\pi}}\int_{-\infty}^{\infty}\mathbf{E}_t(0)e^{i\omega t}d\omega \tag{3.23}$$

so that with $k = \omega/c$, (3.22) becomes

$$\begin{aligned}
\mathbf{E}_t(z) &= \int_{-\infty}^{\infty}\int_{-\infty}^{\infty}\mathbf{E}_{t'}(0)\frac{\exp\left[i\left(t' - t + z/c\right)\right]}{2\pi}d\omega\, dt' && (3.24)\\
&= \int_{-\infty}^{\infty}\mathbf{E}_{t'}(0)\,\delta\left(t' - t + z/c\right)dt' && (3.25)\\
\mathbf{E}_t(z) &= \mathbf{E}_{t'-z/c}(0) && (3.26)
\end{aligned}$$

Eq. (3.26) shows that if we define the temporal profile of an electric field in the $z = 0$ plane, it is then defined for all z as just the initial field propagating along z at the speed of light.

$\mathbf{E}_t(z)$ can be regarded as our optical pulse where we neglect transverse effects, a fair approximation of a well-collimated laser. As we will see, should it encounter a different medium as it propagates, the local spectral profile (and therefore the temporal profile) can be altered. The above connection to the Fourier transform is therefore important to understanding terms used to parameterize the temporal and spectral properties of a pulse.

3.2.1 The spectral phase and time-bandwidth product

Having introduced the Fourier decomposition above, we now identify terms commonly used in photonics to characterize what we consider the longitudinal phase space of an optical pulse in this 1-D approximation. The temporal and spectral fields of a plane wave are linked by the Fourier transform as

$$\begin{aligned} \mathbf{E}_t(z) &= \frac{1}{\sqrt{2\pi}} \int_{-\infty}^{\infty} \widetilde{\mathbf{E}}_\omega(z) e^{-i\omega t} d\omega & (3.27) \\ \widetilde{\mathbf{E}}_\omega(z) &= \frac{1}{\sqrt{2\pi}} \int_{-\infty}^{\infty} \mathbf{E}_t(z) e^{i\omega t} d\omega. & (3.28) \end{aligned}$$

If we adhere to seeking a real solution in the time domain, the relation (3.9) for the complex quantity $\widetilde{\mathbf{E}}(\omega)$ is implied. Note that one can only uniquely define either the temporal or spectral amplitude and phase when the other is assumed given by the above Fourier transform relations.

When parameterizing a 1-D optical pulse, the temporal or spectral profile refers to the optical power. This is proportional to the intensity I of the electric fields given above

$$\begin{aligned} I(\omega) &\propto |E(\omega)|^2 & (3.29) \\ I(t) &\propto |E(t)|^2 & (3.30) \end{aligned}$$

It is often useful to specify the spectral bandwidth $\Delta\omega$ and pulse length Δt then in terms of the full width at half-maximum of these intensity profiles. The shortest possible pulse (in an RMS sense) is always given by the transform of the spectral field with $\phi = 0$ which can be computed to give the minimum pulse length and is dependent on the shape of the spectral amplitude.

From these one can define the conventional minimum time-bandwidth product (TBP) of a given pulse shape pulse $\Delta\nu\Delta t$, where $\Delta\nu$ is the ordinary bandwidth related to the circular bandwidth via $\Delta\nu = \Delta\omega/2\pi$. For a given bandwidth and spectral shape, one can then compare the measured TBP to its minimum to assess the compactness of the pulse (c.f. [53]).

The complex spectral field is typically written in terms of its real amplitude $\mathbf{E}_\omega$ and complex phase ϕ_ω with the phase described by the coefficients D_k in the Taylor expansion in angular frequency as

$$\widetilde{\mathbf{E}}_\omega = \mathbf{E}_\omega \exp\left[i\phi_\omega\right] \tag{3.31}$$

$$\phi_\omega = \sum_k \frac{D_k}{k!}\left(\omega - \omega_0\right)^k \tag{3.32}$$

$$D_k = \frac{\partial^k \phi}{\partial \omega^k} \tag{3.33}$$

for an optical pulse with center frequency at ω_0.

Only the first few coefficients in D_k are of particular interest assuming a relatively slowly varying ϕ_ω over the small region where there is strong spectral amplitude. D_0 represents a constant arbitrary phase ϕ_0 while D_1 has units of time and is the group delay (GD) T_g of an optical pulse. In the narrow-band approximation where we use the Taylor expansion above, $T_g(\omega_0)$ can be regarded as the accumulated time delay of a pulse.

In the continuum sense, $T_g(\omega) = \partial\phi_\omega/\partial\omega$ may be loosely interpreted as describing the expectation value for time of a given frequency component. That is, it describes the correlation between frequency and time. Where all terms higher than $k = 1$ are absent, we therefore still have the bandwidth-limited pulse.

We will return to discussing the significance of these phase terms by inspection of a Gaussian spectrum at the end of Sec. 3.2.3. The effect of the second and third order terms on the temporal profile will then be apparent as we analyze resulting profiles and especially when illustrated by the associated Wigner distribution function, which we introduce presently.

3.2.2 Wigner distribution function

If only to illustrate the effect of dispersion, and for comparison to the longitudinal phase space distribution of charged-particle beam physics, we turn to the Wigner distribution function (WDF) for time-frequency domain signal analysis [54–56]. This will provide a 2-dimensional map whose profiles yield the one-dimensional temporal and spectral intensities, helpful in visualizing the distribution of flux in the time-frequency domain.

The WDF $W(t,\ \omega)$ for a signal defined by its complex spectral amplitude $\widetilde{E}(\omega)$ (and corresponding $E(t)$ given by (3.28)) is

$$W(t,\ \omega) = \frac{1}{2\pi} \int \widetilde{E}\left(\omega + \frac{1}{2}\Omega\right) \widetilde{E}^{*}\left(\omega - \frac{1}{2}\Omega\right) e^{-i\Omega t}\, d\Omega \tag{3.34}$$

The history and properties of the WDF and other variations of such spectrograms are detailed in [54]. While we have chosen this only to visualize the $\omega - t$ phase space, a few properties are worth noting.

$W(t,\ \omega)$ is found to be everywhere real, though not positive definite. Further, the marginals $M(\omega)$ and $M(t)$ generated by integrating over either t or ω, respectively, are found to yield the corresponding intensities $I(\omega)$ and $I(t)$. Finally, the mean values $\langle t(\omega)\rangle$ and $\langle \omega(t)\rangle$ from computing the first-order moments in t and ω are identically equal to the group delay $T_g(\omega)$ and what is referred to as the instantaneous frequency $\Omega_{inst}(t)$ (the latter true when a complex temporal phase is considered). To summarize these:

$$\int W(t,\ \omega)\, dt = I(\omega) \tag{3.35a}$$

$$\int W(t,\ \omega)\, d\omega = I(t) \tag{3.35b}$$

$$\int t\, W(t,\ \omega)\, dt = \frac{d\phi_\omega}{d\omega} = T_g(\omega) \tag{3.35c}$$

$$\int \omega\, W(t,\ \omega)\, d\omega = \frac{d\phi_t}{dt} = \Omega_{inst}(t) \tag{3.35d}$$

3.2.3 Example: the Gaussian pulse

Thus far we have presented analytical definitions for a number of quantities. We now demonstrate them as a whole by calculating the temporal profiles from spectral components for an actively mode-locked, Ti:sapph laser output which can be approximated by a Gaussian spectral distribution [57]. First we show the analytical transform of the transform-limited Gaussian pulse ($\phi_\omega = 0$). We will then illustrate the impact of higher order dispersion on such a pulse.

3.2.3.1 Transform-limited pulse

Consider a plane wave propagating along z with the electric field $\mathbf{E}$ directed in x, a purely linear polarization state. For free propagation this polarization doesn't change, as seen by the independence of the vector components of Eq. (3.26), so that we can instead consider the scalar quantity E. Assume a Gaussian spectral intensity and corresponding field distribution of the form

$$\begin{aligned} I(\omega) &= \frac{1}{2\sigma\sqrt{\pi}} \exp\left[-\left(\frac{\omega-\omega_0}{\sigma}\right)^2\right] && (3.36) \\ \Rightarrow |E(\omega)| &= \frac{1}{\sqrt{2\sigma}\,\pi^{1/4}} \exp\left[-\frac{1}{2}\left(\frac{\omega-\omega_0}{\sigma}\right)^2\right] && (3.37) \end{aligned}$$

for a center frequency ω_0 and a root-mean-squared (RMS) spectral field width of σ. The normalization of (3.36) is chosen so that integrating $\int I(\omega)d\omega$ over all frequencies (positive and negative) is one. Note that this results in a FWHM bandwidth (in intensity) of

$$\Delta\nu_{Gaussian} = \frac{\sqrt{\ln 2}\,\sigma}{\pi} \tag{3.38}$$

and that only $I(\omega > 0)$ is measurable. By Eq. (3.9) we then presume that $I(-\omega) = I(\omega)$. We now compute what is seen in the time domain.

It's simple to analytically solve for the transform-limited pulse where $\phi_\omega = 0$. For the real Gaussian amplitude of Eq. (3.37) and assuming that for $\omega_0 \gg \sigma$ we can make the approximation

$$\int_0^\infty \exp\left[-\frac{1}{2}\left(\frac{\omega-\omega_0}{\sigma}\right)^2\right] e^{-i\omega t}\, d\omega \approx \int_{-\infty}^\infty \exp\left[-\frac{1}{2}\left(\frac{\omega-\omega_0}{\sigma}\right)^2\right] e^{-i\omega t}\, d\omega \tag{3.39}$$

we use Eq. (3.12) to find

$$\begin{aligned} E(t) &= \frac{\sqrt{2\sigma}}{\pi^{1/4}} \exp\left[-\frac{\sigma^2}{2}t^2\right] \cos(\omega_0 t) && (3.40) \\ I(t) &= \frac{2\sigma}{\sqrt{\pi}} \exp\left[-\sigma^2\, t^2\right] \cos^2(\omega_0 t) && (3.41) \end{aligned}$$

so that the temporal intensity appears as a Gaussian envelope on a carrier wave with frequency ω_0. The envelope has temporal intensity FWHM

$$\Delta t_{Gaussian} = \frac{2\sqrt{\ln 2}}{\sigma} \tag{3.42}$$

Alternatively we can compute the complex profile for only positive frequencies using Eq. (3.14) to yield the envelope function $|\widetilde{E}(t)|^2$ alone.

Combining Δt with $\Delta\nu$ from Eq. (3.38) we find the minimum TBP for a Gaussian spectrum to be

$$(\Delta\nu\ \Delta t)_{Gaussian} = \frac{2\ln 2}{\pi} \approx 0.441 \tag{3.43}$$

It's also straightforward to analytically transform a linearly chirped ($D_2(\omega_0) \neq 0$) Gaussian pulse and show dispersive pulse broadening. The new temporal profile is still a Gaussian, but with a modified amplitude and width. In this case it can be shown that the new parameter σ_t specifying the RMS width in time is

$$\sigma_t^2 = \frac{1}{\sigma^2} + \sigma^2 D_2^2 \tag{3.44}$$

so that when GDD dominates, the pulse length grows linearly with the GDD. Where one has the transform-limited pulse length, the linearly chirped pulse length $\Delta t'$ in this Gaussian approximation is typically written in the more convenient form [57]

$$\Delta t' = \Delta t \sqrt{1 + \left(4\ln 2 \frac{D_2}{\Delta t^2}\right)^2} \approx 2.77 \frac{D_2}{\Delta t} \tag{3.45}$$

with the approximation true when the D_2 term dominates. To illustrate how this and higher-order dispersion terms lead to such broadening, we look to the WDF.

3.2.3.2 Optical pulse with higher order dispersion

Consider now the Gaussian spectrum of Eq. (3.37) as we add terms to its complex phase of the form given in Eq. (3.33). While calculations are all done in terms of ω, we plot in wavelength $\lambda = 2\pi c/\omega$ which is easily compared to spectrometer measurements.

Parameters typical of the output of our Ti:sapph laser are a center wavelength $\lambda_0 = 800$ nm and $\Delta\lambda \approx 10$ nm, FWHM. This corresponds to $\omega_0 = 2.355$ Prad/s ("peta-radians per second") and $\sigma = 17.7$ Trad/s ("tera-radians per second") with the resulting spectral profile shown in Fig. 3.1.

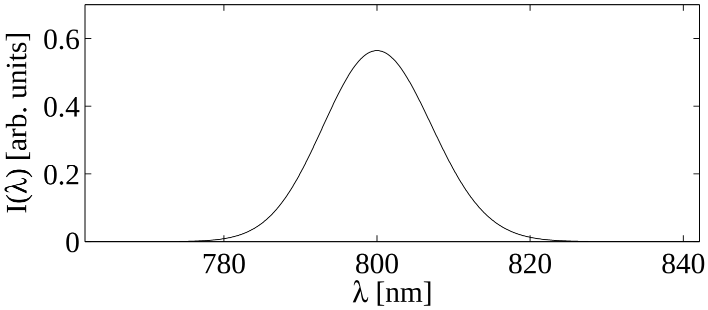

Figure 3.1: Gaussian intensity profile (Eq. (3.36)) where $\lambda_0 = 800$ nm and $\Delta\lambda = 10$ nm.

The form of Eq. (3.33) suggests the scaling of $D_k = \sigma^k k!$ (when working in frequency units normalized to bandwidth) to see effects of a comparable scale for each term. Using the spectrum of Fig. 3.1, we take a complex spectral phase of the form in Eq. (3.33) with only one term $D_k = \sigma^k k!$ present at a time. We compute the resulting complex transient $\widetilde{E}(t)$ by summing over only the positive spectrum around $\omega = +\omega_0$.

To quantify the effect on laser pulse length, the RMS pulse width is computed as the second order moments of the resulting $I(t)$. These are tabulated in Table 3.1 with the corresponding coefficients used. The Wigner distribution from Eq. (3.34) and temporal profile $I(t)$ by Fourier transform are shown in Fig. 3.2, with comparison to the transform-limited case. Also plotted as the green overlaid curves in Fig. 3.2 are the corresponding group delays $T_g(\lambda)$ computed directly from $\partial\phi_\omega/\partial\omega$.

From the identities of Eq. (3.35) we know that summing the WDF over all time to project onto the spectral axis yields the spectrum. This is indeed the case as the projections of all four plots yield the spectrum shown in Fig. 3.1. The projections to the time axis yield $I(t)$, which is also verified. Finally, the mean value in frequency should be $T_g(\lambda)$ (shown as the green curves), which is the case.

Table 3.1: RMS pulse width σ_t for a pulse with center wavelength $\lambda_0 = 800$ nm and $\Delta\lambda = 10$ nm in the presence of higher order dispersion terms $D_k = \sigma^k k!$ (see Fig. 3.2).

D_k used	σ_t [fs]
0	40.0
$D_2 = 6.40 \times 10^3$ fs^2	89.5
$D_3 = 1.09 \times 10^6$ fs^3	120.7
$D_4 = 2.46 \times 10^8$ fs^4	182.0

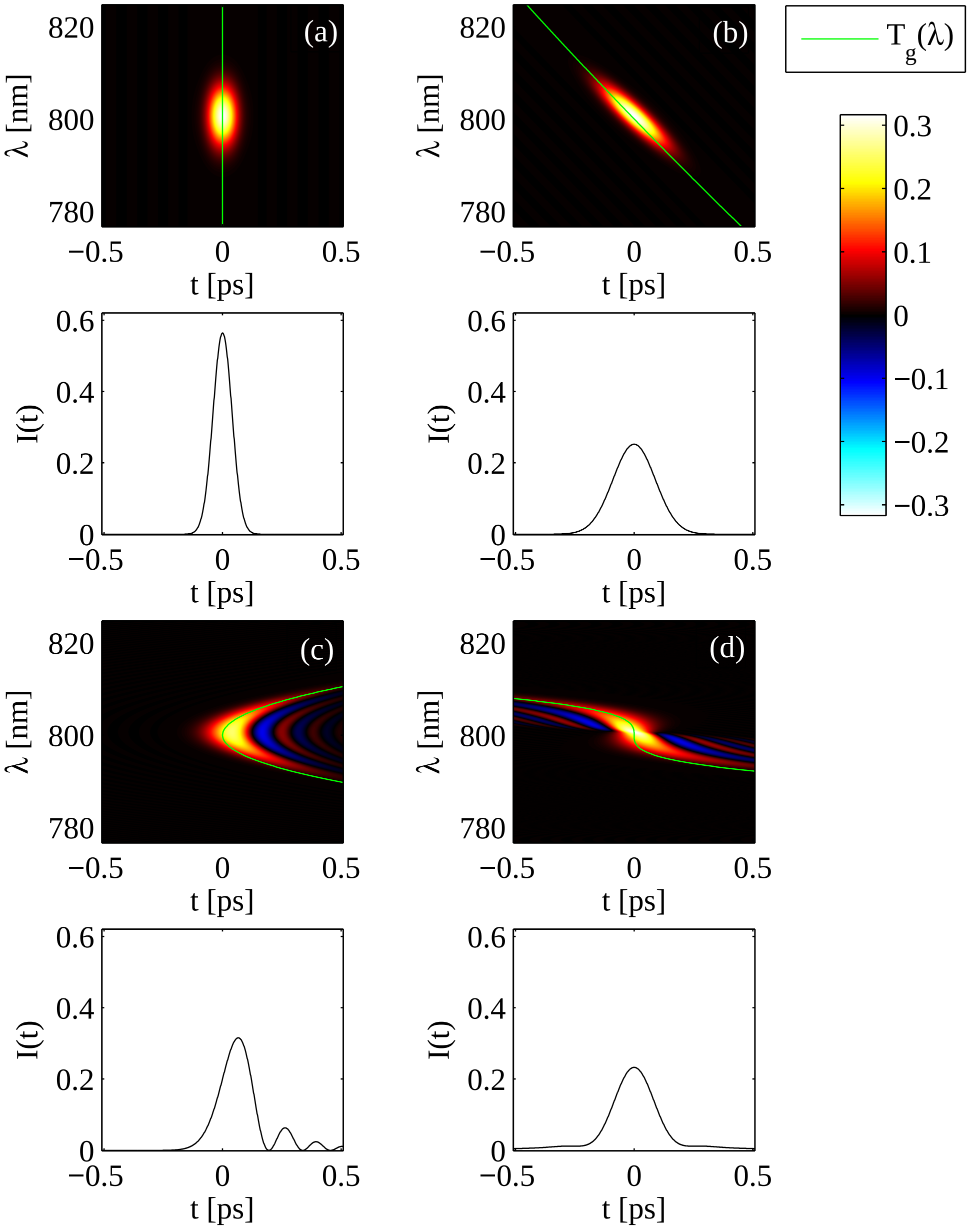

Figure 3.2: WDF (tops) and intensity profiles (bottoms) for a pulse with center wavelength λ_0 = 800 nm and bandwidth $\Delta\lambda$ = 10 nm for (a) the transform-limited case, (b) $D_2 = 6.38 \times 10^3$ fs^2, (c) $D_3 = 1.08 \times 10^6$ fs^3, and (d) $D_4 = 2.45 \times 10^8$ fs^4, with RMS pulse lengths shown in Table 3.1. Each WDF is overlayed with the associated group delay $T_g(\lambda)$ (green curves).

Let us inspect these now, one-by-one. For the transform-limited pulse, Table 3.1 shows the minimum pulse length we expect from Eq. (3.42) of $\sigma_t = 40$ fs ($\Delta t = 94$ fs). The corresponding WDF in Fig. 3.2, plot (a) appears as a compact vertical ellipse with the time projection also of a Gaussian form. By analogy to the phase space distribution of particles in accelerator physics, this is the "upright ellipse" in the $\omega - t$ phase space. The inverse relationship between bandwidth and pulse length implies that larger bandwidth will elongate the ellipse in λ while contracting it in t.

The D_1 term has units of time and simply translates the upright ellipse in time with no effect on the shape. This term is therefore skipped in the illustration.

The second-order coefficient D_2, known as the group delay dispersion (GDD) has units of time-squared. As the derivative of T_g, it describes a linear correlation between frequency and group delay (linear chirp). Plot (b) shows the result is the equivalent of the ellipse in the analogous longitudinal phase space with spectral shearing of the ellipse in time. We now see how the linear chirp leads to the corresponding broadening and diluting of the temporal pulse with the width of the stretched Gaussian projection given by Eq. (3.45).

This leading order term is significant for our studies. Firstly, this is the primary source of pulse broadening. As we will review in Sec. 3.3, propagation of a pulse through simple glasses (such as lenses, polarizers or vacuum windows) can generate GDD. Therefore where an ultrashort pulse is needed, this GDD must be quantified and compensated as needed.

Secondly, the tilted ellipse is what is used in EOSD. So far we have only explained that the EOSD process will encode some other temporal profile we want to measure onto the spectral profile of our linearly chirped laser pulse. From the tilted ellipse of plot (b) we see more clearly how temporal encoding is considered equivalently spectrally encoded for the chirped pulse. (This is not precisely true, which will we will investigate by solution of the wave equation for EOSD in a later section.) Under this approximation, knowledge of the slope of the ellipse, given by the magnitude of D_2, is required to map the measured spectral modulation to a temporal one.

Third-order dispersion (TOD) D_3 is cubic in phase and therefore corresponds to a quadratic chirp. For broadband laser pulses TOD can be generated, for example, by accumulated intracavity dispersion in the laser. Plot (c) of Fig. 3.2 shows the effect. The parabolic distribution tends to weight the temporal distribution to one side. The result is an asymmetric temporal profile with a sharp peak and long tail. This can yield an apparent temporal FWHM that appears shorter, but we note that the oscillatory tail still generates a longer RMS pulse length (Table 3.1).

Aside from complicating our modeling of the optics, TOD can be undesirable when driving nonlinear effects. This includes frequency doubling and tripling, which we have done with our laser to convert our infrared pulse to the ultraviolet. As frequency conversion is an intensity-dependent effect, the long tail may become wasted energy when the weak tail is too weak to drive the harmonic generation.

Finally, though we won't address it explicitly anywhere else, plot (d) shows the effects of fourth-order dispersion. As a cubic chirp, we see that it also tends to symmetrically broaden the pulse. However, unlike the linear chirp of GDD, strong fourth-order dispersion tends to clump the center band of the distribution about $t = 0$ while flinging out the spectral tails. Comparing (b) to (d), the result is a temporal profile that again appears slightly narrower in a FWHM sense, but has a small, much longer symmetric tail in time.

Some sources of higher-order dispersion were suggested here, and of course many others are known and even used in our experiment. Diagnosis of the laser pulse shape is presented in Sec. 5.3. For now we turn to reviewing simple material dispersion which we will encounter throughout our calculations.

3.3 Linear, isotropic medium and dispersion

We now consider the well-known dispersion relations for propagation through a dielectric medium and how we regard them throughout.

When an electromagnetic plane wave encounters the interface between vacuum and the medium, we know the continuity of the wave equations for **E** and **B** at the interface will generate partial transmission and reflection at the boundary. This is in general dependent on the polarization and angle of incidence and yields the well-known Fresnel equations (c.f: Sec. 4.6 of [58] or Sec. 7.2 of [8]). At non-normal incidence this solution also generates refraction, the frequency dependence of the direction of propagating of the transmitted beam.

We will restrict ourselves to the case of normal incidence so that refraction can be neglected. We further neglect the effects of partial reflection, assuming no amplitude or phase modulation at the change of medium so that 100% of the beam is transmitted at both the entrance and exit face of the material.

Propagation through an isotropic medium is then described as the solution for Eq. (3.17) in the case of an infinite plane wave that generates an isotropic, first-order polarization $\mathbf{P}^{(1)}$ directly proportional to the applied field **E**. In the notation of Boyd [51]:

$$\mathbf{P}_t^{(1)}(z) = \epsilon_0\,\chi^{(1)}\mathbf{E}_t(z) \tag{3.46}$$

where $\chi^{(1)}$ is the linear susceptibility. In the case of the plane wave, the Laplacian simplifies as

$$\nabla^2 \mathbf{E} = \frac{\partial^2 \mathbf{E}}{\partial z^2} \tag{3.47}$$

Substituting these into Eq. (3.18)

$$\frac{\partial^2 \widetilde{\mathbf{E}}_\omega(z)}{\partial z^2} + \frac{\omega^2}{c^2}\widetilde{\mathbf{E}}_\omega(z) = -\frac{\chi^{(1)}\omega^2}{c^2}\widetilde{\mathbf{E}}_\omega(z) \tag{3.48}$$

which can be rewritten as

$$\begin{aligned} \frac{\partial^2 \widetilde{\mathbf{E}}_\omega(z)}{\partial z^2} &= -(1+\chi^{(1)})\frac{\omega^2}{c^2}\widetilde{\mathbf{E}}_\omega(z) && (3.49) \\ &= -\frac{\epsilon\,\omega^2}{c^2}\widetilde{\mathbf{E}}_\omega(z) && (3.50) \end{aligned}$$

where we have introduced the (relative) permittivity ϵ, related to the absolute permittivity ϵ, susceptibility, and refractive index n of the material by $\epsilon = \epsilon/\epsilon_0 = 1 + \chi^{(1)} = n^2$.

This has the same plane wave solution as before, but now with a new wavenumber $k^2 = \epsilon\omega^2/c^2 = n^2\omega^2/c^2$. Should n be constant, the wave would simply propagate through the medium at a different rate as it would in vacuum. However, where the response of the material is frequency dependent, as is typically the case, we find the dispersion relation $k(\omega) = n(\omega)\omega/c$. This will distort the temporal profile as it propagates.

Again following the treatment of Sec. 3.2 with our wave incident on the medium at $z = 0$, but with frequency-dependent $k(\omega)$, we find the solution

$$\widetilde{\mathbf{E}}_\omega(z) = \widetilde{\mathbf{E}}_\omega(0)e^{ik(\omega)z} \tag{3.51}$$

Real $\mathbf{E}_t$ further implies here that $n(-\omega) = -n(\omega)$ (with non-dissipative media) so $\widetilde{\mathbf{E}}_\omega = \widetilde{\mathbf{E}}^*_{-\omega}$. The evolution of $\mathbf{E}_t(z)$ along z will again be found from Eq. (3.8).

$$\mathbf{E}_t(z) = \frac{1}{\sqrt{2\pi}}\int_{-\infty}^{\infty} \widetilde{\mathbf{E}}_\omega(0)e^{ik(\omega)z}e^{-i\omega t}d\omega \tag{3.52}$$

so that the right hand side is defined entirely by the wave incident at $z = 0$. If the medium has thickness L and we still neglect boundary effects, the profile of the emerging wave will then be given by $\mathbf{E}_t(L)$. Expressing $\widetilde{\mathbf{E}}_\omega(0)$ by its amplitude and phase we have

$$\mathbf{E}_t(L) = \frac{1}{\sqrt{2\pi}} \int_{-\infty}^{\infty} \mathbf{E}_\omega(0) \exp\left\{i\left[\phi_\omega(0) + k(\omega)L\right]\right\} e^{-i\omega t} d\omega \tag{3.53}$$

where we see that the material contributes only a frequency- and thickness-dependent phase shift.

For an arbitrary refractive index the above does not reduce neatly as it did before because of the frequency-dependence of $k(\omega)$. The resulting signal distortion will have significant impact later in the context of EOSD. We satisfy ourselves for now by considering our model Ti:sapph pulse traversing a thick piece of glass.

Again, as our laser pulse operates at center frequency ω_0 with a finite bandwidth $\sigma \ll \omega_0$, we perform a Taylor expansion of both ϕ_ω and $k(\omega)L$. We then see that the derivatives of the wavenumber k will simply be added into the initial coefficients in the expansion of ϕ_ω.

The constant term and first derivatives will describe the phase shift from propagating through the material at a modified group velocity $v_g = c/n(\omega_0)$. Discarding these and to only second order,

$$\mathbf{E}_t(L) \approx \frac{1}{\sqrt{2\pi}} \int_{-\infty}^{\infty} \mathbf{E}_\omega(0) \exp\left\{i\left[\phi_\omega(0) + \frac{L}{2}(\omega - \omega_0)^2 \left.\frac{\partial^2 k}{\partial \omega^2}\right|_{\omega_0}\right]\right\} e^{-i\omega t} d\omega \tag{3.54}$$

where $\partial^2 k/\partial\omega^2$ is the group velocity dispersion (GVD) [57], the GDD accumulated per unit length. Expressed by the refractive index, material dispersion for a thickness L then yields an additional D_2 to the phase as

$$D_2(\omega_0) = \left(\frac{2}{c}\left.\frac{\partial n}{\partial \omega}\right|_{\omega=\omega_0} + \frac{\omega}{c}\left.\frac{\partial^2 n}{\partial \omega^2}\right|_{\omega=\omega_0}\right) L \tag{3.55}$$

so that we see the resulting pulse after a length L in a medium is approximately the transform of the initial pulse with an additional linear spectral chirp D_2. Under the Gaussian pulse approximation and assuming that $\phi_\omega(0) = 0$, we can then use Eq. (3.45) to estimate the pulse length with this additional dispersion.

The index is typically specified in the literature by Sellmeier relations given as a function of wavelength. Using $\lambda = 2\pi c/\omega$, we then rewrite D_2 as

$$D_2(\lambda) = \left(\frac{\lambda^3}{2\pi c^2}\left.\frac{\partial^2 n}{\partial \lambda^2}\right|_{\lambda=\lambda_0}\right) L \tag{3.56}$$

In conjunction with an optical element's index relation, Eq. (3.56) and (3.45) combined give a way to quickly estimate the broadening of a laser pulse after propagating through the given material. The strength of the added chirp will depend on the curvature of the index of the glass and the thickness being traversed.

For example, we frequently make use of 25-mm thick Glan polarizing prisms [58] as high-quality polarizers that are made of calcite. We may want to verify that this will have a negligible impact on pulse broadening.

Calcite is a birefringent material exhibiting two indices of refraction, something that will be discussed in some detail in the next section. In a Glan prism, the transmitted wave propagates along the natural extraordinary axis in the polarizer with index n_e [58]. To calculate D_2 we use material properties given by the Sellmeier relations with coefficients for n_e in calcite provided by [59] as

$$n_e(\lambda) = 2.18438 + \frac{8730.9}{\lambda^2 - 10180} - 2.4411 \times 10^{-9}\lambda^2 \tag{3.57}$$

when λ is given in nanometers. The resulting n_e and D_2/L in the region of $\lambda_0 = 800$ nm are shown in Fig 3.3.

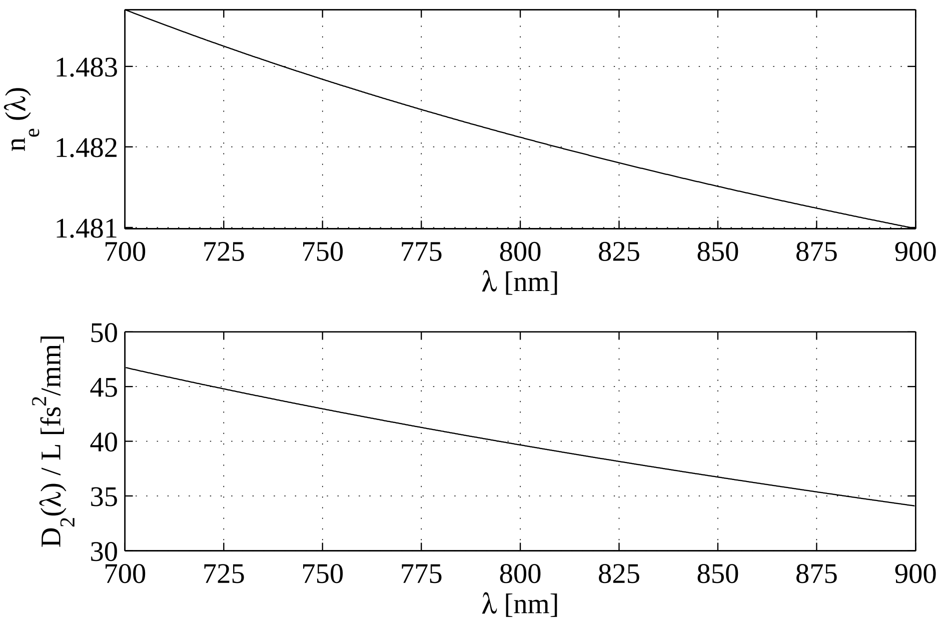

Figure 3.3: Extraordinary index n_e (top) and group velocity dispersion D_2/L (bottom) for a calcite crystal.

The index shows only a very small change over the bandwidth of the laser of less than a part per thousand with a very slight curvature. At 800 nm this yields a GVD of 39.7 fs^2/mm so that for our 25 mm polarizer we have $D_2 = 991.6\ \mathrm{fs}^2$. Using our 10 nm FWHM Gaussian laser pulse (Fig. 3.1) with $\Delta t\ =\ 94.2$ fs, Eq. (3.45) gives an broadened pulse width of $\Delta t'\ =\ 98.6$ fs, a broadening of only 4.4 fs, in good agreement with numerical integration of (3.54) and typically of minor effect.

3.4 Anisotropic medium and birefringence

So far we have considered free propagation in vacuum as well as in other isotropic media with a frequency-dependent response. While dispersion in the latter case can distort the temporal profile through changes in the spectral phase, the polarization state (the direction of **E**) remains unaltered.

We now consider a material with a first-order (in induced polarization) anisotropy. In this case the polarization can be modified. Birefringent behavior will be described while framing our notation in a manner that will be useful as we eventually proceed to second-order nonlinearities and EOSD.

The more general form of the first-order induced polarization is given by

$$\widetilde{\mathbf{P}}_\omega = \epsilon_0\, \boldsymbol{\chi}^{(1)}_\omega \cdot \widetilde{\mathbf{E}}_\omega \tag{3.58}$$

where $\boldsymbol{\chi}^{(1)}_\omega$ is the relative permittivity tensor of rank 2, also dependent on ω. This has geometric implications as an applied field along a given axis can now be mapped into a field along a different direction.

Returning to Maxwell's equations, Eq. (3.15) is now

$$\nabla \times \nabla \times \widetilde{\mathbf{E}}_\omega(\mathbf{r}) - \frac{\omega^2}{c^2}\widetilde{\mathbf{E}}_\omega(\mathbf{r}) = \frac{\omega^2}{c^2}\boldsymbol{\chi}^{(1)}_\omega \cdot \widetilde{\mathbf{E}}_\omega(\mathbf{r}) \tag{3.59}$$

$$\nabla \times \nabla \times \widetilde{\mathbf{E}}_\omega(\mathbf{r}) = \frac{\omega^2}{c^2}\boldsymbol{\epsilon}^{(1)}_\omega \cdot \widetilde{\mathbf{E}}_\omega(\mathbf{r}) \tag{3.60}$$

with relative permittivity tensor $\boldsymbol{\epsilon}^{(1)}_\omega = \mathbf{I} + \boldsymbol{\chi}^{(1)}_\omega$ where **I** is the identity matrix. If we still take solutions with spatial dependence of the form

$$\widetilde{\mathbf{E}}_\omega(\mathbf{r}) = \widetilde{\mathbf{E}}_\omega \exp\left(i\, \mathbf{k} \cdot \mathbf{r}\right) \tag{3.61}$$

then the gradient operator becomes $\nabla = i\,\mathbf{k}$ so that

$$-\mathbf{k}\times\mathbf{k}\times\widetilde{\mathbf{E}}_\omega = \frac{\omega^2}{c^2}\boldsymbol{\epsilon}^{(1)}_\omega\cdot\widetilde{\mathbf{E}}_\omega \tag{3.62}$$

Combining (3.1) and (3.6) we also find

$$\mathbf{k}\cdot\left(\boldsymbol{\epsilon}^{(1)}_\omega\cdot\widetilde{\mathbf{E}}_\omega\right) = 0 \tag{3.63}$$

Note that while Eq. (3.1) tells us that **k** will be perpendicular to **D**, (3.63) shows that **k** is only in general perpendicular to **E** if $\boldsymbol{\epsilon}^{(1)}_\omega$ is proportional to the identity matrix, that is to say the medium is isotropic. In that case the problem reduces to the one presented in the previous section.

In the coordinate basis of an anisotropic crystal, $\boldsymbol{\epsilon}^{(1)}_\omega$ can be written [51, 52]

$$\boldsymbol{\epsilon}^{(1)}_\omega = \begin{pmatrix} n_x^2 & 0 & 0 \\ 0 & n_y^2 & 0 \\ 0 & 0 & n_z^2 \end{pmatrix} \tag{3.64}$$

where n_i are the indices of refraction along a given direction. For an isotropic medium then, $n_x^2 = n_y^2 = n_z^2 = n^2$ with the solution already given. In the case where none are equal, the material is referred to as biaxially birefringent [52]. For our present purposes we consider the classic uniaxial crystal with $n_x^2 = n_y^2 = n_o^2$ and $n_z^2 = n_e^2$ where n_o and n_e are called the ordinary and extraordinary indices of refraction so that $\boldsymbol{\epsilon}^{(1)}_\omega$ is

$$\boldsymbol{\epsilon}^{(1)}_\omega = \begin{pmatrix} n_o^2 & 0 & 0 \\ 0 & n_o^2 & 0 \\ 0 & 0 & n_e^2 \end{pmatrix} \tag{3.65}$$

For uniaxially birefringent materials, the response of electric dipoles along one direction of the crystal is different than the other two. This can be related to the crystal structure itself and is visualized in Fig. 3.4 with the crystal described by (3.65) drawn in its own coordinate basis, extraordinary axis oriented along z. Also shown is the presence of an applied field **E** in the $x-z$ plane incident at an angle θ from the z axis. This is shown in terms of components $\mathbf{E}_p$ and $\mathbf{E}_s$ where $\mathbf{E}_p$ is the component polarized in the plane of incidence and $\mathbf{E}_s$ polarized perpendicular to the plane of incidence.

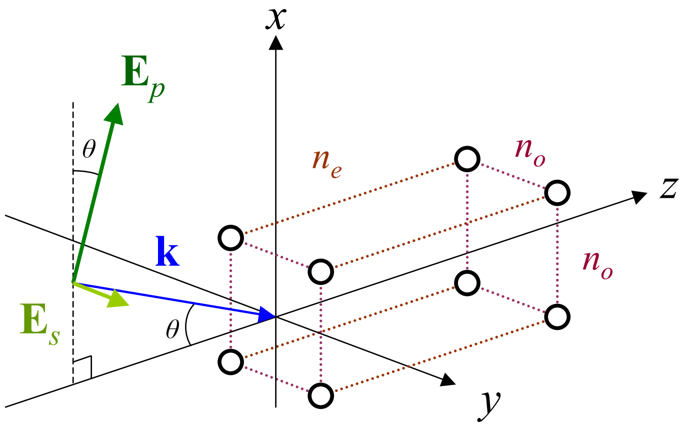

Figure 3.4: Geometry for a field $\mathbf{E} = \mathbf{E}_s + \mathbf{E}_p$ incident at angle θ to the extraordinary axis of a uniaxial crystal with extraordinary index n_e an ordinary index n_o in the coordinate basis of the crystal with n_e oriented along z. $\mathbf{E}_p$ and $\mathbf{E}_s$ are the components of $\mathbf{E}$ polarized parallel and perpendicular to the plane of incidence, respectively.

With this geometry, we consider the solution of (3.62) for the field shown. Inserting (3.65) and rearranging

$$\left[(\mathbf{k}\times\mathbf{k}\times) + \left(\frac{\omega^2}{c^2}\boldsymbol{\epsilon}^{(1)}_{\omega}\cdot\right)\right]\widetilde{\mathbf{E}}_{\omega} = 0 \tag{3.66}$$

$$\begin{pmatrix} \frac{\omega^2 n_o^2}{c^2} - k_x^2 - k_z^2 & k_x k_y & k_x k_z \\ k_x k_y & \frac{\omega^2 n_o^2}{c^2} - k_x^2 - k_z^2 & k_y k_z \\ k_x k_z & k_y k_z & \frac{\omega^2 n_e^2}{c^2} - k_x^2 - k_y^2 \end{pmatrix}\begin{pmatrix} E_{\omega,x} \\ E_{\omega,y} \\ E_{\omega,z} \end{pmatrix} = 0 \tag{3.67}$$

where k_i denotes the cartesian component of a vector. Nontrivial solutions to this equation are given when the determinant of the matrix of coefficients shown is equal to zero. Computing the determinant and collecting terms we find

$$\left(\frac{k_1^2 + k_2^2 + k_3^2}{n_o^2} - \frac{\omega^2}{c^2}\right)\left(\frac{k_1^2 + k_2^2}{n_o^2} + \frac{k_3^2}{n_e^2} - \frac{\omega^2}{c^2}\right) = 0 \tag{3.68}$$

From Fig 3.4 we see that the components of $\mathbf{k}$ are $(k_1,\ k_2,\ k_3) = (-k\sin\theta,\ 0,\ k\cos\theta)$ so that we can simplify

$$\left(\frac{k^2}{n_o^2} - \frac{\omega^2}{c^2}\right)\left(\frac{k^2\cos^2\theta}{n_o^2} + \frac{k^2\sin^2\theta}{n_e^2} - \frac{\omega^2}{c^2}\right) = 0 \tag{3.69}$$

We see there are now two solutions in k^2. One simply yields $k^2 = \omega^2 n_o^2/c^2$, indicating a solution with an index of refraction equal to that of the ordinary index. The other we write using $k^2 = \omega^2 n_e'^2/c^2$ as

$$\frac{1}{n_e'^2(\theta)} = \frac{\cos^2\theta}{n_o^2} + \frac{\sin^2\theta}{n_e^2} \tag{3.70}$$

This is a modified index of refraction. Using these two solutions in the eigenvalues k^2 one can further compute the eigenvectors of the matrix to determine $\mathbf{k}$. One finds [52] that the solution $n = n_o$ corresponds to the wave $\mathbf{E}_s$ in Fig. 3.4, called the ordinary wave. The solution given by (3.70) is the extraordinary wave and is valid for the component with the polarization $\mathbf{E}_p$. It travels with an effective index of refraction that is a function of the angle between the angle of incidence and the extraordinary axis, also referred to as the optic or $\hat{c}$-axis of the crystal, where $\hat{c} = \hat{z}$ as drawn in Fig. 3.4.

Note that if the wave is incident along $\hat{c}$, $\theta = 0 \Rightarrow n_e' = n_o$, and when the extraordinary wave travels perpendicular to $\hat{c}$, $\theta = 0 \Rightarrow n_e' = n_e$.

Also, the solution above with the beam incident at an angle $-\theta$ to the optics axis z, is equivalent to having the beam normal with the crystal basis rotated by θ. In this way we can adjust the index of the extraordinary component by instead fabricating a crystal with the faces cut at the angle θ that adjusts n_e' to suit our application. This way an extraordinary wave incident normal to the surface of the angle-cut crystal will see the designed n_e'.

In solving for the components $\mathbf{k}$, one finds that the asymmetry of the crystal in $x-z$ generates a coupling in these two coordinates. The result is that the power flow for our extraordinary wave E_p in fact propagates at what is referred to as the walk-off angle ρ to the wave vector [52, 57] and is given by

$$\tan\rho = n_e'^2(\theta)\sin\theta\cos\theta\left[\frac{1}{n_e^2} - \frac{1}{n_o^2}\right] \tag{3.71}$$

As noted in [52], for calcite (strong birefringence) this is typically only a few degrees so that when using very thin crystals we assume the spatial walk-off is not significant.

That the behavior of uniaxial crystals can modify the phase of orthogonal polarization directions allows one to fabricate polarizing optics.

3.4.1 Polarization optics and Jones vectors

In this section we review the usual Jones calculus notation for the description of polarization states [58] and illustrate the use of uniaxial birefringence in the construction of polarizing optics. We will use this in the context of EOSD which is found to be, in part, a polarization-modifying effect.

In discussing the polarization of monochromatic plane waves, we note that in principle the direction of $\widetilde{\mathbf{E}}_\omega$ is only constrained to the transverse plane. The Jones vector formalism allows one to keep track of the accumulated phase differences between perpendicular components.

For a given frequency component of a plane wave, such as one from our laser, the transverse components in the laboratory $x - y$ frame can be decomposed in general Jones vector form as

$$\begin{aligned} \widetilde{\mathbf{E}}_\omega(z,t) &= \widetilde{\mathbf{E}}_\omega e^{i\ (kz-\omega t)} && (3.72)\\ &= \begin{pmatrix} E_x e^{i\phi_x} \\ E_y e^{i\phi_y} \end{pmatrix} e^{i\ (kz-\omega t)} && (3.73) \end{aligned}$$

where E_i are the field amplitude in the i direction and ϕ_i the complex phase of that component. Rearranging

$$\begin{aligned} \widetilde{\mathbf{E}}_\omega(z,t) &= \begin{pmatrix} 1 \\ E_y/E_x e^{i(\phi_y-\phi_x)} \end{pmatrix} E_x e^{i\ (kz-\omega\ t+\phi_x)} && (3.74)\\ &= \begin{pmatrix} 1 \\ Re^{i\ \Delta\phi} \end{pmatrix} E_x e^{i\ (kz-\omega\ t+\phi_\omega)} && (3.75) \end{aligned}$$

where we have defined the phase difference $\Delta\phi = \phi_y - \phi_x$ and amplitude ratio $R = E_y/E_x$.

When $R = 0$ and $\Delta\phi = 0$ we have linear polarization in x, an electric field that oscillates in the x direction as it propagates along z. When $R = 1$ and $\Delta\phi = \pi/2$ we have circular polarization. The electric field vector rotates around z once per wavelength λ as it propagates in z. For arbitrary $\Delta\phi$ and R we have elliptical polarizations.

Birefringent materials such as those discussed in the previous section allow us to modify the relative phase of these orthogonal components relative to the orientation of the crystal's optic axis. For example, if we cut a uniaxial crystal so that the extraordinary axis lies along y and ordinary along x, then E_y and E_x

will propagate with indices of refraction n_e and n_o, respectively. While in the crystal the phases will vary as $\phi = kz = 2\pi nz/\lambda$ so that after a distance L through the material we get the retardance $\Gamma = \Delta\phi(L)$ [58]

$$\Gamma = \frac{2\pi L\Delta n}{\lambda} \tag{3.76}$$

with $\Delta n = n_e - n_o$. If we choose the length to be

$$L = \frac{\lambda}{4}\frac{1}{\Delta n} \tag{3.77}$$

then $\Gamma = \pi/2$, a quarter cycle of retardance. A slab such as this is therefore called a quarter wave plate. The effect it has on the relative phases of the polarization can then be related by a 2D Jones matrix operator in the coordinate basis of the crystal as

$$\mathbf{\Gamma} = \begin{pmatrix} e^{i\,\Gamma/2} & 0 \\ 0 & e^{-i\,\Gamma/2} \end{pmatrix} \tag{3.78}$$

with which we can define the new relative polarization state by the operation

$$\mathbf{E}' = \mathbf{\Gamma}\mathbf{E} \tag{3.79}$$

This assumes that **E** is defined in the basis of the crystal. When the crystal is rotated, this is equivalent to a counter rotation of **E**. We can then apply the coordinate transform

$$\boldsymbol{R}_\theta = \begin{pmatrix} \cos\theta & -\sin\theta \\ \sin\theta & \cos\theta \end{pmatrix} \tag{3.80}$$

that rotates **E** into the basis of Γ, then back to the lab frame as

$$\mathbf{E}' \quad = \quad \boldsymbol{R}_\theta\mathbf{\Gamma}\boldsymbol{R}_\theta^{-1}\mathbf{E} \tag{3.81}$$

We see from the form that this is equivalent to a coordinate transform of the Jones matrix in its own basis to that of the laboratory.

For the $\Gamma = \pi/2$ quarter wave plate set to an angle $\theta = 45°$ and a wave incident polarized linearly in x with unit magnitude, Eq. (3.81) yields

$$\mathbf{E}' = \begin{pmatrix} \cos\theta & -\sin\theta \\ \sin\theta & \cos\theta \end{pmatrix} \begin{pmatrix} e^{i\pi/4} & 0 \\ 0 & e^{-i\pi/4} \end{pmatrix} \begin{pmatrix} \cos\theta & \sin\theta \\ -\sin\theta & \cos\theta \end{pmatrix} \begin{pmatrix} 1 \\ 0 \end{pmatrix} \tag{3.82}$$

$$= \frac{1}{\sqrt{2}} \begin{pmatrix} 1 & e^{i\,\pi/2} \\ e^{i\,\pi/2} & 1 \end{pmatrix} \begin{pmatrix} 1 \\ 0 \end{pmatrix} \tag{3.83}$$

$$\mathbf{E}' = \frac{1}{\sqrt{2}} \begin{pmatrix} 1 \\ e^{i\,\pi/2} \end{pmatrix} \tag{3.84}$$

which with reference to Eq. (3.75) is the form of circularly polarized light. The quarter wave plate as a circular polarizer will be of use in our apparatus.

Another optic we will use is the beam-displacing polarizing prism shown in Fig. 3.5. Where a wave plate is a thin crystal, the thick beam-displacing polarizer makes use of the walk-off relation (3.71) to spatially separate the incoming polarizations, as illustrated in Fig. 3.5.

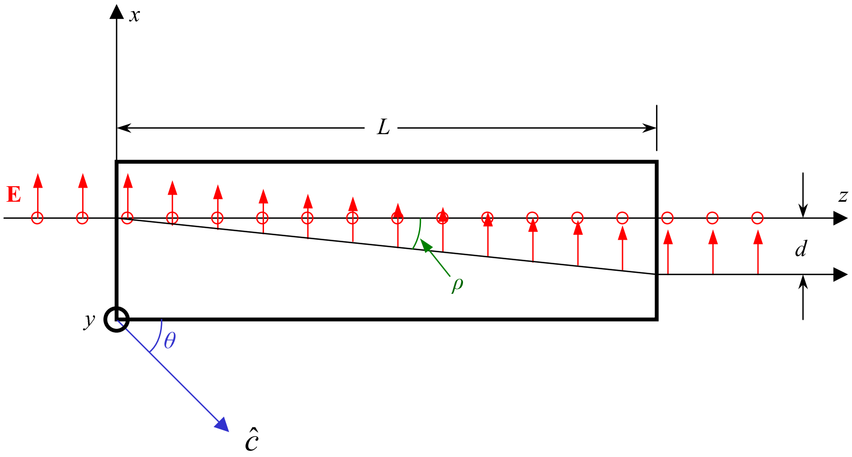

Figure 3.5: Geometry of a beam-displacing prism of length L and crystal cut angle θ illustrating the use of birefringent walk off to separate polarization components into parallel propagating beams. The angle ρ is related to θ by Eq. (3.70) and (3.71).

The beam-displacing prism we used is Thorlabs part number BD27. This is a calcite prism with length $L = 28$ mm. For calcite at our laser wavelength of 800 nm, $n_o = 1.6487$ and $n_e = 1.4821$ [59]. The crystal cut angle θ is not specified. However, the walk-off angle ρ given by (3.71) is generally maximized for a broad range of wavelengths when $\theta = 45°$. Using these, we find that $\rho = 6.11°$ so that the spatial separation of the polarized beams emerging from the prism is d = 3.0 mm at 800 nm.

In this chapter we have illustrated the notation and methodology of some linear optics employed. From here we can proceed with describing the optical setup used for EOSD, the solution of Maxwell's equations for the nonlinear EOSD problem as it relates to our configuration, and how the recovered signal relates to the measurement of the transient signal from the electron beam.

CHAPTER 4

ELECTRO-OPTIC SPECTRAL DECODING

In this chapter we begin with a brief introduction to the technique chosen to measure the transient signal from the electron bunch. With this in hand, we provide further details on some practical matters of the optics installation. We will then return with a more complete description of the measurement process which then identifies additional distortions that may be encountered in our measurements.

4.1 Qualitative description of electro-optic spectral decoding

As previously stated, future collider applications and present high-gradient laser plasma wakefield accelerators and other photoinjector-based accelerators such as free electron lasers operating with picosecond bunch durations place a higher demand on the time resolution of bunch distribution diagnostics. This has led to significant advancements in the field of what is referred to in the literature as electro-optic sampling over the last ten years [30, 60–71].

These methods allow the probing of diagnostic light such as coherent transition radiation (Sec. 2.4) [30, 69] or the bunch wakefields (or "velocity fields") [61, 63] with sub-picosecond time resolution. Primary techniques are based on encoding a THz-regime transient from the electron beam onto the polarization of either the spectral or spatial components of a single broadband Ti:sapph laser pulse. This is done by mixing the laser pulse and signal from the beam in an electro-optically active crystal. Potential applications in shot-to-shot, non-interceptive diagnostics continue to be pursued for live beam monitoring of the bunch distribution.

While a number of approaches are available, we have chosen to employ the variant known as electro-optic spectral decoding (EOSD) with the process illustrated schematically in Fig. 4.1 [30, 60, 65, 68, 69]. Proceeding from left to right, we begin with our ultra-short laser pulse and transient signal $E_{THz}(t)$ from the beam with the latter, in principle, proportional to the longitudinal distribution of the bunch $\rho(t)$ that we aim to measure. The linearly polarized laser pulse is stretched with a strong linear chirp to provide a correlation in the time-frequency domain (c.f. Sec. 3.2.3.2). The laser probe and signal from the beam are then co-propagated through a nonlinear, electro-optically active crystal (EO crystal). From the perspective of the laser pulse, the effect in the crystal can be regarded for our present discussion as a time-dependent wave plate with a retardation proportional to the externally applied $E_{THz}(t)$. Assuming that the laser and signal remain perfectly velocity matched (no dispersion) through the crystal, this results in a time-dependent retardation $\Gamma(t) \ll 1$ in the polarization ellipse along the laser pulse.

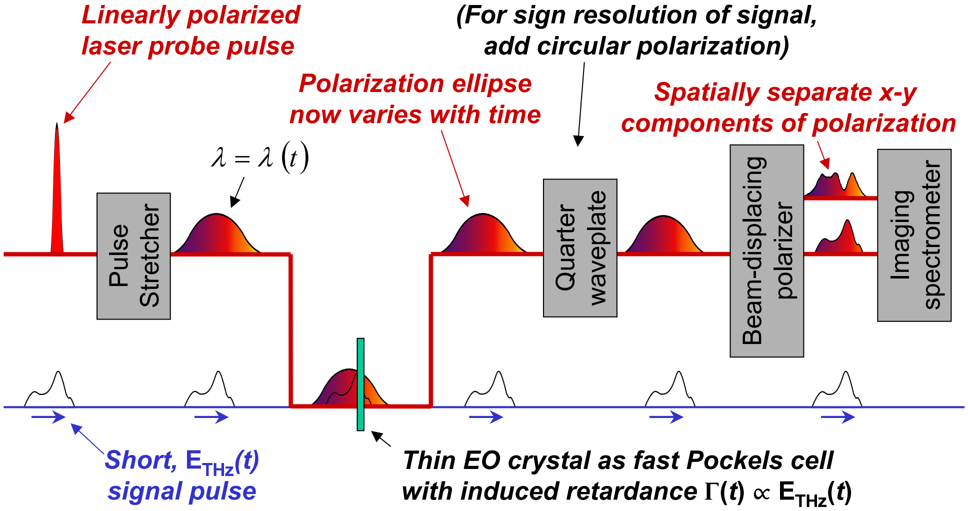
Linearly polarized laser probe pulse
(For sign resolution of signal, add circular polarization)
Polarization ellipse now varies with time
Spatially separate x-y components of polarization
$\lambda = \lambda(t)$
Pulse Stretcher
Quarter waveplate
Beam-displacing polarizer
Imaging spectrometer
Short, $E_{THz}(t)$ signal pulse
Thin EO crystal as fast Pockels cell with induced retardance $\Gamma(t) \propto E_{THz}(t)$

Figure 4.1: From left to right, a step-by-step diagram of the electro-optic spectral decoding process illustrating the mixing of the THz pulse from the accelerator modulating the polarization of a chirped laser pulse with subsequent spectrally resolved, polarization-analyzing optics.

The modulated pulse is then sent through a quarter wave plate oriented to act as a circular polarizer. This is found to enable resolution of the sign of the modulation on the pulse as well as improve the sensitivity of the measurement [62, 69].

With the proper crystal orientation and following a similar treatment of the Jones vectors as seen in [30, 60, 62], the resulting intensities of the horizontal and vertical components at this point can be found to be

$$I_x(t) = \frac{1}{2}\{1 - \sin[\Gamma(t)]\} I_{laser}(t) \tag{4.1}$$

$$I_y(t) = \frac{1}{2}\{1 + \sin[\Gamma(t)]\} I_{laser}(t) \tag{4.2}$$

where $I_{laser}(t)$ is the initial temporal profile of the laser pulse and we assume the incident laser pulse to be linearly polarized in x.

We are then left to resolve this now-modulated laser pulse in measurable terms. In the EOSD approach the change in the temporal profile is considered equivalent to a spectral modulation due to the linear correlation of the spectral and temporal components of the pulse [60]. If one has sufficient information about the initial spectral amplitude and phase, one can find the linear map of wavelength to time from the group delay $t_g(\lambda)$.

In this sense, (4.1) becomes

$$\begin{aligned} I_x(\lambda) &= \frac{1}{2}\left\{1 - \sin\left[\Gamma(t_g[\lambda])\right]\right\} I_{laser}(\lambda) && (4.3) \\ I_y(\lambda) &= \frac{1}{2}\left\{1 + \sin\left[\Gamma(t_g[\lambda])\right]\right\} I_{laser}(\lambda) && (4.4) \end{aligned}$$

Therefore, we then proceed through an analyzing system that probes the change in the polarization state of the spectral profile.

Previously in spectral encoding experiments only one of the two polarizations have been measured. However, in multi-shot experiments it was shown that by recording the intensity of both polarizations one can perform a balanced measurement, improving the signal-to-noise ratio and allowing the correction of shot-to-shot fluctuations in the laser intensity.

We perform a similarly balanced measurement by using a polarization-resolving spectrometer system consisting of our beam-displacing prism (Fig. 3.5) and a near-IR imaging spectrometer [72]. This allows one to simultaneously measure the spectra of both polarization components.

If we take the difference over the sum of the measured spectra, we then find from (4.3)

$$\frac{I_x(\lambda) - I_y(\lambda)}{I_x(\lambda) + I_y(\lambda)} = -\sin\left[\Gamma(t_g[\lambda])\right] \tag{4.5}$$

which is, to first order, proportional to $-\Gamma(t)$. By mapping the measured signal from wavelength to a time axis via $t_g(\lambda)$ we can then determine $\Gamma(t) \propto E_{THz}$.

For completeness we note that a similar analysis in the absence of the quarter wave plate yields

$$\frac{I_x(\lambda) - I_y(\lambda)}{I_x(\lambda) + I_y(\lambda)} = \cos\left[\Gamma(t_g[\lambda])\right] \tag{4.6}$$

so that the measured signal is approximately $1 - \Gamma^2(t)$, an even function in $\Gamma(t)$ and therefore not sign-resolving (a loss of phase information).

In these broad strokes we have not yet addressed a number of other known effects that occur in the nonlinear crystal. We do have an idea of the hardware necessary to perform the measurement, however. We will describe this before returning to a more thorough treatment of the interaction between the probe and signal in the nonlinear crystal.

4.2 Titanium-sapphire laser layout

Our first requirement is a titanium-sapphire laser which provides the requisite, broadband probe pulse. As we describe the laser and layout of the optical systems, we remain mindful of alternately using the Ti:sapph to generate ultra-short UV pulses for use in driving beam generation at the accelerator (Sec. 2.6).

The new titanium-sapphire (Ti:sapph) laser system is a commercially available *Spitfire Pro XP* regen seeded by a *Tsunami* oscillator. These are respectively pumped by a 30 W, Q-switched *Empower* laser and 5 W continuous-wave *Millennia Pro* diode laser, respectively, with both pumps operating at 532 nm. The full system, produced by Newport Corporation, Spectra Physics division, produce 800-nm pulses with output parameters summarized in Table 4.1.

Table 4.1: Optimized Ti:sapph laser parameters.

Oscillator center wavelength	800 nm
Oscillator repetition rate	81.25 MHz
Oscillator pulse energy	14.5 nJ
Oscillator max bandwidth	15 nm (FWHM)
Amplified repetition rate	1 kHz
Amplified pulse energy	3 mJ
Amplified max bandwidth	12 nm (FWHM)

The system is supplemented with a *Dazzler* produced by Fastlite [73], an acousto-optic programmable dispersive filter (AOPDF) for shaping of the IR pulse. This allows one to directly manipulate the spectral phase and amplitude coefficients (Eq. (3.32)-(3.33)) of the Ti:sapph laser pulse.

The layout of the laser system is shown in Fig. 4.2. The seed laser output passes a 75% reflective, 25% transmissive pellicle beam splitter (BS). The reflected beam is used for optional timing feedback (see Sec. 5.2.3) and other diagnostics. The transmitted beam is passed as the amplifier seed.

Where the Ti:sapph system is used as the photoinjector drive laser, a frequency tripler [74] converts the 800 nm IR output of the amplifier to the UV at 266 nm, as required to maximize photoemission at the Cs_2Te photocathode. The tripler consists of a 300-µm β-barium borate (BBO) doubling crystal, a calcite delay-compensation crystal, 800-nm half-wave plate, then the final 150-µm BBO tripling ($\omega + 2\omega \rightarrow 3\omega$)

crystal. In this configuration and using the peak amplifier output, 10% conversion efficiency is realized producing up to 300-μJ UV pulses.

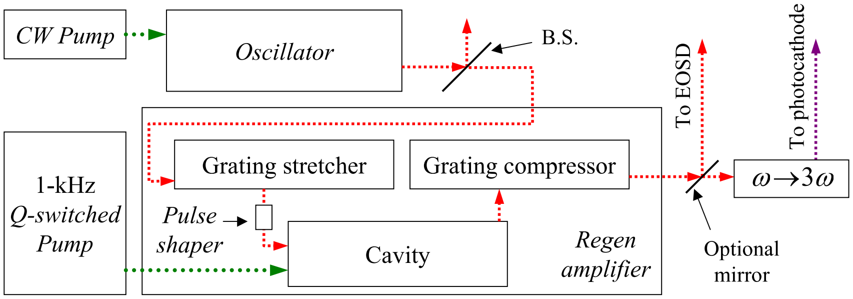

Figure 4.2: Schematic of the modified optical layout for the Ti:sapph laser system including oscillator pick-off beam splitter and pulse shaper.

The amplified IR output was chosen for EOSD where a strongly chirped IR laser pulse will be required. EOSD occurs on a single-shot basis with the signal from the beam modulating the spectrum of the laser pulse. To see the entire pulse, assuming that the relative timing of the beam and laser are perfectly stable, we must at least stretch the laser to envelop the full duration of the signal, on the order of 1 ps or more.

The amplifier's grating compressor in combination with the *Dazzler* can easily produce the required ps-scale chirp. Also, the regen selects only a 1-kHz pulse train (or less with gating) for amplification. This provides suppression of the seed laser's 81.25-MHz repetition rate to the accelerator's 1 Hz. This is advantageous for our single-shot measurements: concerns about the EOSD spectrometer camera integrating many pulses are mitigated as we can easily gate down to only laser pulse per accelerator cycle.

To accommodate concurrent delivery of the Ti:sapph and the existing Nd:YLF and HeNe alignment lasers to the accelerator vault, they are combined before transport; see Fig. 4.3. The combined beams are then sent into an optical transport line to deliver pulses from the A0PI laser lab to an optical breadboard at the photocathode in the accelerator tunnel 20 m away. The transport line consists of five mirrors with a double high-reflectivity (HR) coating at 800 nm and 266 nm and with a 5-m imaging lens at its midpoint.

4.3 Optical apparatus for EOSD

Next we will describe optics specific to EOSD. This includes the geometry of the EOSD optics used to combine our probe and signal pulses at the nonlinear crystal, then the analyzing optics used to determine the resulting modulation of the polarization modulation in the frequency domain.

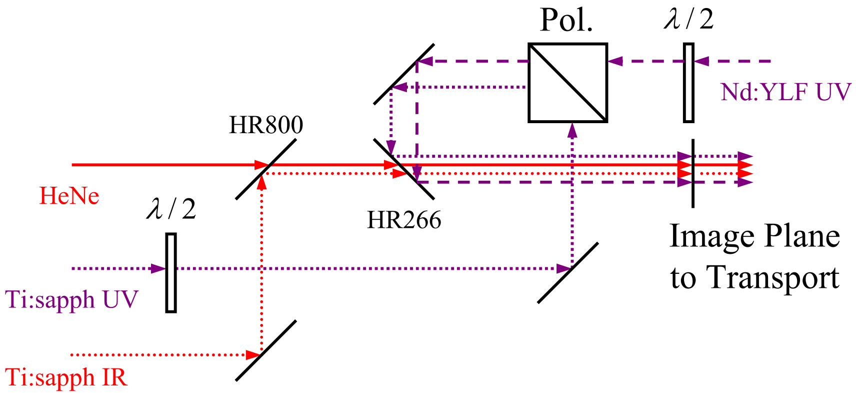

Figure 4.3: Optical layout used to combine the Ti:sapph UV, Ti:sapph IR, Nd:YLF UV and HeNe alignment laser before transport to the accelerator tunnel. Polarization of the two UV beams are controlled independently using the two half-wave plates and combined in a UV polarizing cube. A high-reflectivity (HR) 800-nm mirror combines the IR with the HeNe (632 nm) alignment lasers then joined with the UV beams upon transmission through the HR266 mirror.

Additional optics used to aid in adjusting the relative time of arrival of the laser pulse at the crystal to match that of the CTR pulse are also necessary. While we can make timing adjustments to the laser using relative phase controls detailed later (Fig. 5.1), we are attempting to overlap two events of 1-ps duration with each occurring only once per second. Scanning of the 1-ps EOSD window over the full 1-s range is impractical. We therefore use a three-stage process to narrow this down in large increments using optics overlaid with those used for EOSD.

The arrangement for the relative timing makes use of the OTR, which we have noted is significantly weaker than the CTR emitted from the target (Sec. 2.4). Because of this, we use the Nd:YLF system as the drive laser for the photoinjector in these experiments. This allows the generation of a macropulse train comprised of several tens of electron bunches with a 1-MHz spacing. In this way, existing diagnostics such as the streak camera can easily detect the integrated power of the bunch train to assist in narrowing down the time of arrival.

The laser pulses enter the accelerator bunker at the RF gun (Fig. 2.1). At this point the relative timing is verified to the sub-ns scale using a fast photodiode mounted at the photocathode. The drive laser is then directed to the photocathode for beam generation. The IR pulse is split from the combined laser path and propagates along an imaging system mounted to the tunnel wall to the EOSD breadboard, shown in Fig. 4.4, mounted downstream near diagnostic cross X24.

The breadboard is configured in a two-level arrangement. TR from cross X24 (Fig. 2.6) can be directed by existing insertable mirrors to either level. In the lower level, the OTR from the beam is combined with light leakage from the laser's periscope and sent to the streak camera (Fig. 2.1). This is used to further reduce the uncertainty in the time of arrival from the ns scale to the ps scale.

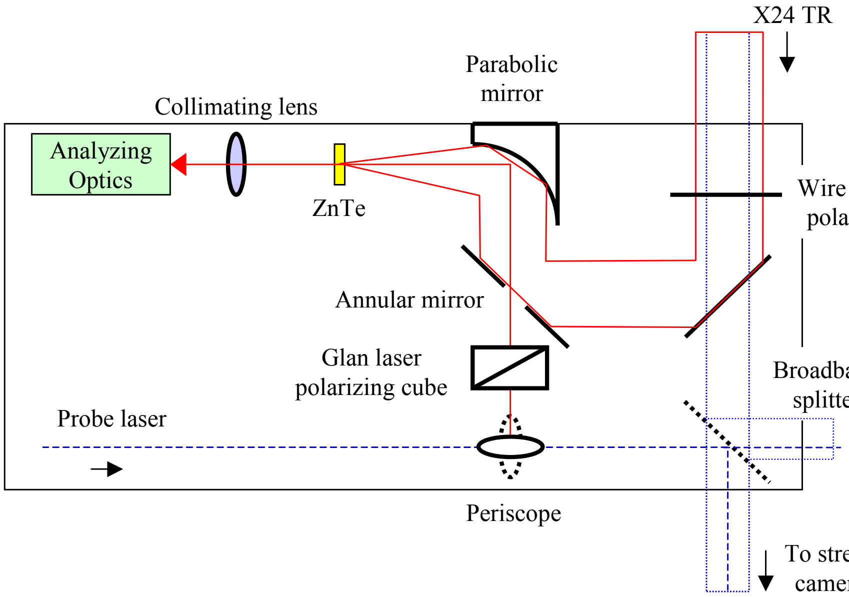

Figure 4.4: Two-level optical layout of dual-purpose EOSD breadboard. Lower level (blue) combines laser leakage from periscope with OTR from beam (Fig. 2.6) to be sent to the streak camera. Upper level (red) combines laser pulse with CTR pulse, focusing collinear beams onto the ZnTe crystal. The modulated laser pulse is then collimated and sent to the analyzing optics.

We first account for a roughly 3.5 ns optical path difference between the laser's path along the wall and the beam's propagation down the beamline. The streak camera then enables us to walk in the time delay of the laser to overlap with the streak image of the OTR. This is straightforward as in its widest temporal range the streak camera covers ~2 ns. As the two signals get closer, one can narrow the sweep range to improve the temporal resolution down to the ps level. At this point we know the TR and laser probe are synchronized at the OTR/laser beam combiner on our EOSD breadboard in Fig. 4.4.

On the second level we combine the optical paths of the CTR from X24 with the laser probe arriving from the vertical periscope using an annular mirror. The CTR first passes a wire mesh polarizer to ensure a pure horizontal polarization state of the signal at the crystal. The laser passes a high-quality polarizing prism to ensure pure vertical polarization.

The combining mirror has an inner diameter of 5 mm to permit transmission of the laser probe. This is designed to fit within the weak hole in the reflected CTR wavefront (Sec. 2.4) which is estimated to be a bright ring with diameter of ~10 mm. The two are then collinearly focused by the parabolic mirror onto a 1-mm thick, zinc-telluride (ZnTe) electro-optic crystal. The modulated laser pulse is then re-collimated and sent to the EOSD analyzing optics.

The crystal is the point at which our signal and probe must overlap in time. Adjusting for another relative optical path difference for the TR and laser of about 270 ps from the previous synchronization point to the crystal, one can scan the laser timing just a few picoseconds until a measurable EOSD signal is observed in the spectrometer. See Fig. 4.5.

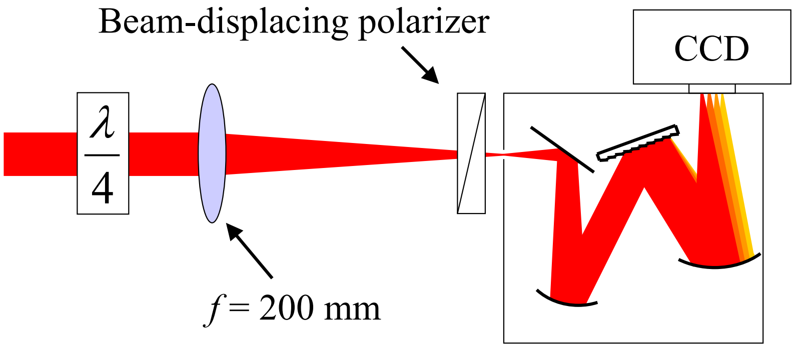

Figure 4.5: EOSD analyzing optics detailing the polarization-resolving spectrometer configuration. Polarization component perpendicular to page is displaced 3 mm into the plane shown.

4.4 Quantitative analysis of electro-optic spectral decoding

With all of the optics defined, we can now present a more quantitative explanation of the EOSD system and, in particular, the response of the EO crystal. How this leads to a mixing of the CTR pulse in the THz regime with the laser pulse in the near IR is found by expanding on the solutions of Chap. 3 to include the second-order, nonlinear polarization term. We can then discuss in detail the effect on the probe laser pulse and how the analyzing optics recover the THz waveform.

4.4.1 Form of the second-order polarization coupling

Continuing the expansion of the induced polarization to second order we now find [51, 52]

$$\mathbf{P}_t = \epsilon_0\,\chi^{(1)} \cdot \mathbf{E}_t + \epsilon_0\,\mathbf{E}_t \cdot \chi^{(2)} \cdot \mathbf{E}_t \tag{4.7}$$

where the final term is a tensor product related to $\chi^{(2)}$, the second order susceptibility, representing the coupling of the induced polarization to the square of the field. The tensor $\chi^{(2)}$ is now of rank 3, describing how two components of an applied field map to the those of the induced polarization **P**. As these are typically given in terms of the coupling strengths of eigenmodes in the material, this is considered in the frequency domain.

We restrict ourselves for now to an applied, real driving field **E** that is the sum of two monochromatic waves at different frequencies ω_1 and ω_2

$$\mathbf{E}(t) = \widetilde{\mathbf{E}}_1 e^{-i\,\omega_1\,t} + \widetilde{\mathbf{E}}_2 e^{-i\,\omega_2\,t} + \text{ c.c.} \tag{4.8}$$

As the second-order induced polarization is of a higher-order tensor nature, it is helpful to diverge from our previous notation and instead write it in component form as

$$P_i^{(2)}(t) = \epsilon_0\,\chi_{ijk}^{(2)}\,E_j(t)\,E_k(t) \tag{4.9}$$

where we use the Einstein implied summation over repeated indices convention to express the dot products. Inserting (4.8) and expanding we find [51]

$$\begin{aligned} P_i^{(2)}(t) \quad = \quad & \epsilon_0\,\chi_{ijk}^{(2)}\,[\tilde{E}_{1,j}\,\tilde{E}_{1,k}\,e^{-2i\omega_1 t} \;+\; \tilde{E}_{2,j}\,\tilde{E}_{2,k}\,e^{-2i\omega_2 t} \\ & + 2\tilde{E}_{1,j}\,\tilde{E}_{2,k}\,e^{-i(\omega_1+\omega_2)t} \;+\; 2\tilde{E}_{1,j}\,\tilde{E}_{2,k}^{*}\,e^{-i(\omega_1-\omega_2)t} \\ & + \tilde{E}_{1,j}\,\tilde{E}_{1,k}^{*} + \tilde{E}_{2,j}\,\tilde{E}_{2,k}^{*}] + \text{ c.c.} \end{aligned} \tag{4.10}$$

The product yields a polarization with a number of frequency components. Writing these individually as

$$P_i^{(2)}(t) = \sum_n \tilde{P}_i(\omega_n)e^{-i\omega_n t} + \text{ c.c.} \tag{4.11}$$

the allowed components $\tilde{P}_i(\omega_n)$ are

$$\tilde{P}_i(2\omega_1) = \epsilon_0\, \chi^{(2)}_{ijk}(2\omega_1; \omega_1, \omega_1)\tilde{E}_{1,j}\, \tilde{E}_{1,k} \quad \text{(SHG)} \tag{4.12a}$$

$$\tilde{P}_i(2\omega_2) = \epsilon_0\, \chi^{(2)}_{ijk}(2\omega_2; \omega_2, \omega_2)\tilde{E}_{2,j}\, \tilde{E}_{2,k} \quad \text{(SHG)} \tag{4.12b}$$

$$\tilde{P}_i(\omega_1 + \omega_2) = 2\epsilon_0\, \chi^{(2)}_{ijk}(\omega_1 + \omega_2; \omega_1, \omega_2)\tilde{E}_{1,j}\, \tilde{E}_{2,k} \quad \text{(SFG)} \tag{4.12c}$$

$$\tilde{P}_i(\omega_1 - \omega_2) = 2\epsilon_0\, \chi^{(2)}_{ijk}(\omega_1 - \omega_2; \omega_1, -\omega_2)\tilde{E}_{1,j}\, \tilde{E}^*_{2,k} \quad \text{(DFG)} \tag{4.12d}$$

$$\begin{aligned} P_i(0) &= \epsilon_0\, \chi^{(2)}_{ijk}(0; \omega_1, -\omega_1)\tilde{E}_{1,j}\, \tilde{E}^*_{1,k} \\ &\quad + \epsilon_0\, \chi^{(2)}_{ijk}(0; \omega_2, -\omega_2)\tilde{E}_{2,j}\, \tilde{E}^*_{2,k} \quad \text{(OR)} \end{aligned} \tag{4.12e}$$

where we have explicitly added the dependence of $\chi^{(2)}$ on the frequencies ω_1 and ω_2 of the input waves to the output frequency ω_3 as $\chi^{(2)}(\omega_3;\ \omega_1, \omega_2)$. As done by Boyd, the various components are labeled by their corresponding phenomena. The first two are second-harmonic generation (SHG), output waves that are at twice the frequency of the inputs. Similarly we have sum-frequency generation (SFG) and difference-frequency generation (DFG). Finally is optical rectification (OR), a DC bias signal.

Note that for all of these the real monochromatic wave in time is composed by adding its complex conjugate, consistent with (4.11). As the OR signal is already real, adding its complex conjugate simply doubles the total OR signal, in agreement with the expression given by Boyd [51].

Eq. (4.12) shows in a very general way the behavior of the second-order susceptibility tensor and how it relates the spatial and spectral components of the incident wave(s) to the generation of a secondary wave via polarization of the crystal. The polarization couplings and the allowed frequency transitions are found to be related to the arrangement and allowed energy transitions of electric dipoles in a given crystal.

Concentrating first on the frequency dependence, of particular interest for our purposes are the behavior of zinc-blende structure materials such as zinc-telluride (ZnTe) or gallium-phosphide (GaP) which allow transitions of the near IR broadband laser pulse to and from the broadband THz regime. Specifically, DFG of the IR components to the zero-offset THz regime ($\omega_{IR,1} - \omega_{IR,2} \rightarrow \omega_{THz}$) are allowed, as well as SFG and DFG of the THz regime to generate IR ($\omega_{IR,1} \pm \omega_{THz} \rightarrow \omega_{IR,2}$).

The first of these is frequently referred to as "optical rectification" in the literature as it converts the laser with center frequency in the near infrared down to an optical pulse with effectively zero optical bias. The intense, broadband laser can therefore generate ultrashort pulses of THz light [75].

The second is the coupling of interest for our application as it can describe a change to the frequency and/or polarization content of a laser pulse in the presence of an externally applied THz field. In the description given by Gallot and Grischkowsky [76], the process is treated in the frequency domain as the sum- and difference-frequency generation of the THz field with the laser under the assumption that neither the laser nor signal are depleted. This has the advantage of allowing straightforward analysis of the distortion of the signals due to dispersion in the crystal [66, 69, 77].

We therefore assume that the OR portion allowing the laser to be converted to an additional THz wave remains negligible compared to the signal we're measuring over the full length through the crystal. Further we make the undepleted-pump approximation [51] for the THz signal while still allowing for dispersion. These combined assume the spectral amplitude of the signal does not change, though its spectral phase can change with z depending on the index of refraction, as discussed in Sec. 3.3. In this way, the variation in z of the spectral components for our THz signal linearly polarized in y is written (Eq. (3.51))

$$\tilde{E}_2^{THz}(\omega, z) = \tilde{E}_2^{THz}(\omega, 0)e^{ik(\omega)z} \tag{4.13}$$

with the other polarization components $\tilde{E}_1^{THz} = \tilde{E}_3^{THz} = 0$.

Neglecting the OR term means that in terms of frequency coupling we only need to consider the SFG and DFG terms with $\omega_{IR,1} \pm \omega_{THz} \to \omega_{IR,2}$. Assuming both couplings are constant in frequency over the range of both the signal and probe spectra, we write it in component form as simply $\chi^{(2)}_{ijk}$ in the laboratory frame and can neglect all the other frequency couplings.

Finally, we will allow for the laser polarization to change by studying a solution that admits a polarization that can in general have an arbitrary orientation. To do this in a form familiar from our earlier formalism, we next simplify the form of the tensor components $\chi^{(2)}_{ijk}$ in the lab frame.

On our optical breadboard for EOSD 4.4 we mix a horizontally polarized THz signal from the electron bunch with our vertically polarized laser collinearly onto a 1-mm thick ZnTe crystal. ZnTe is of the zinc-blende structure (class $\bar{4}3$m), illustrated in Fig. 4.6, left.

The crystal is cut so it surfaces lie in the $\langle 110 \rangle$ plane of the crystal, that is, a 45 °cut. We will orient our lab system so that this is across the surface normal in the direction $\hat{n} = (\frac{1}{\sqrt{2}},\ 0,\ \frac{1}{\sqrt{2}})$ with our wave then propagating along the same direction. The view along the $\hat{n}$ propagation direction is shown in Fig. 4.6, right.

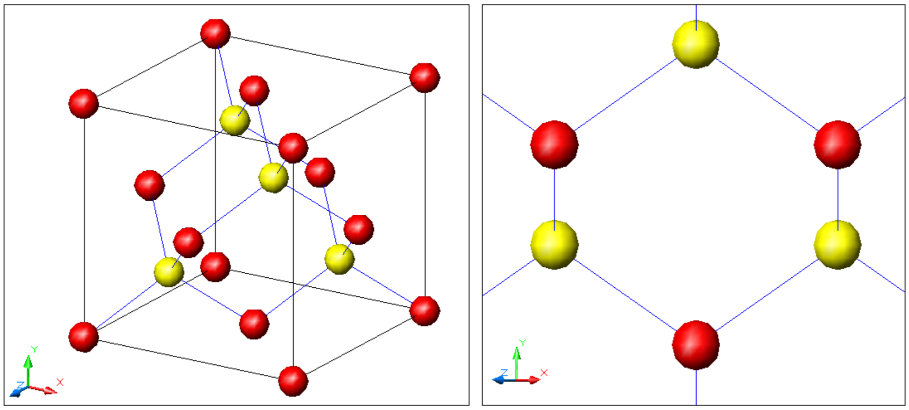

Figure 4.6: *Left:* The structure of ZnTe in its own coordinate basis showing arrangement of cubically arranged anions (red) and cations (yellow) with bonds (blue). *Right:* View of lattice along propagation direction for ⟨110⟩-cut ZnTe.

To first order, ZnTe is not birefringent. However, under the applied THz field the structure is distorted (from the IR probe's perspective) due to the second-order polarization. In the crystal's own coordinate basis $\mathbf{r}_c$, $\chi^{(2),c}_{ijk} = \chi^{(2)}$ for $i \neq j \neq k$ and 0 otherwise for this class of crystals [51, 64]. This means that waves initially polarized in x and y, respectively, map to an induced second-order polarization in z (as well as all other permutations).

As the incident signal and probe polarizations are fixed to components in the lab frame, it's useful to performing a full coordinate transform of $\chi^{(2),c}_{ijk}$ to the same frame. As discussed in Sec. 4.3, we mix our signal and probe with initially orthogonal polarizations, as illustrated in Fig 4.7, with an overlay of the crystal in its own basis $\mathbf{r_c}$. The crystal is rotated 45° about its own y_c axis to reflect the ⟨110⟩ cut of the crystal. We further allow a rotation about the lab z axis by angle θ which is critical in establishing coupling for the two waves [30, 64, 69].

The coordinate transform T_{ij} from $\mathbf{r}_c$ to $\mathbf{r}$ is given by first rotating 45° about the y axis, then a subsequent rotation θ about the z axis. This is written as

$$T_{ij} = \begin{pmatrix} \cos\theta & -\sin\theta & 0 \\ \sin\theta & \cos\theta & 0 \\ 0 & 0 & 1 \end{pmatrix} \begin{pmatrix} \frac{1}{\sqrt{2}} & 0 & -\frac{1}{\sqrt{2}} \\ 0 & 1 & 0 \\ \frac{1}{\sqrt{2}} & 0 & \frac{1}{\sqrt{2}} \end{pmatrix} \tag{4.14}$$

$$= \begin{pmatrix} \frac{\cos\theta}{\sqrt{2}} & -\sin\theta & \frac{\cos\theta}{\sqrt{2}} \\ \frac{\sin\theta}{\sqrt{2}} & \cos\theta & -\frac{\sin\theta}{\sqrt{2}} \\ \frac{1}{\sqrt{2}} & 0 & \frac{1}{\sqrt{2}} \end{pmatrix} \tag{4.15}$$

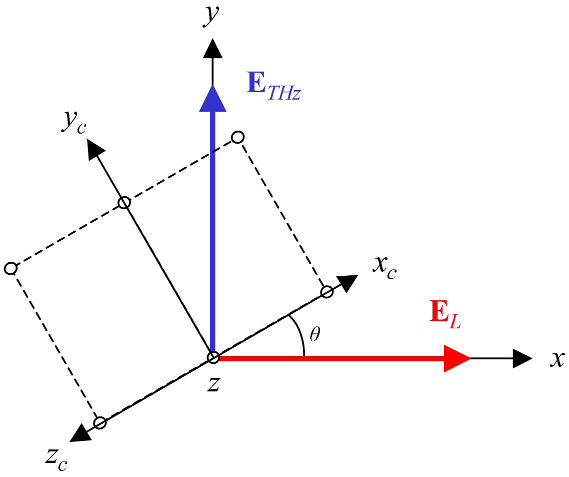

Figure 4.7: Lab coordinate system **r** showing the initial orientation of the polarizations of the orthogonally polarized THz signal and laser probe as well as the orientation of the crystal coordinate basis for the ⟨110⟩-cut ZnTe with an additional rotation θ about the lab's z-axis.

Our tensor can then be written in the laboratory frame by recomputing the elements from the sums

$$\chi^{(2)}_{ijk} = T_{ir}T_{js}T_{kt}\chi^{(2),c}_{rst} \tag{4.16}$$

Simplification is straightforward as, for zinc blende-ordered crystals, $\chi^{(2),c}_{rst}$ has only the six elements where $rst = 123$ (and its permutations). Furthermore, this will be then dotted in the lab frame with the THz waveform of the form of (4.12)

$$\tilde{P}_i = 2\epsilon_0\,\chi^{(2)}_{ijk}\tilde{E}^{THz}_j\,\tilde{E}_k + 2\epsilon_0\,\chi^{(2)}_{ijk}\tilde{E}^{THz}_j\,\tilde{E}^*_k \tag{4.17}$$

where the field $\tilde{E}^{THz}_j$ has only a $j = 2$ component and the components of the laser field $\tilde{E}_k$ are left arbitrary. Therefore one only needs to include the nine elements for i and k, each summed over the six elements on the right hand side. Symmetries in the components of T_{ij} also help simplify the solution.

Inserting the dot product with the THz field, we then find the 2D tensor

$$\chi^{(2)}_{ijk}\tilde{E}^{THz}_j = \chi^{(2)}_{i2k}\tilde{E}^{THz}_2 \tag{4.18}$$

$$= \chi^{(2)}\tilde{E}_{THz}\begin{pmatrix} 3\cos^3\theta - 2\cos\theta & 2\sin\theta - 3\sin^3\theta & 0 \\ 2\sin\theta - 3\sin^3\theta & 3\cos\theta - 3\cos^3\theta & 0 \\ 0 & 0 & -\cos\theta \end{pmatrix} \tag{4.19}$$

We define an effective second order coupling tensor $\chi^{(2),eff}(\theta)$ as

$$\chi^{(2)}_{eff}(\theta) = \chi^{(2)} \begin{pmatrix} 3\cos^3\theta - 2\cos\theta & 2\sin\theta - 3\sin^3\theta & 0 \\ 2\sin\theta - 3\sin^3\theta & 3\cos\theta - 3\cos^3\theta & 0 \\ 0 & 0 & -\cos\theta \end{pmatrix} \tag{4.20}$$

so that we can now return to our previous notation and write the second order polarization in frequency as

$$\widetilde{\mathbf{P}}^{(2)}(\omega_{THz} + \omega) = 2\epsilon_0\, \tilde{E}(\omega_{THz})\, \chi^{(2)}_{eff}(\theta) \cdot \widetilde{\mathbf{E}}(\omega) \tag{4.21}$$

$$\widetilde{\mathbf{P}}^{(2)}(\omega_{THz} - \omega) = 2\epsilon_0\, \tilde{E}(\omega_{THz})\, \chi^{(2)}_{eff}(\theta) \cdot \widetilde{\mathbf{E}}^{*}(\omega) \tag{4.22}$$

where $\widetilde{\mathbf{E}}(\omega)$ is the complex component of our laser. These look similar to the form of the first order polarization in birefringent materials (Eq. (3.58)), but with a strength now proportional to $\tilde{E}_{THz}$.

4.4.2 Dependence of coupling strength on crystal rotation

To see the effect of crystal rotation on the coupling between the Ti:sapph and THz signals in the crystal, we now treat both as monochromatic waves and apply Maxwell's equations. A similar solution is presented in [64, 69] by allowing for the rotation of the applied THz field instead of the crystal. However, this yields a solution in the coordinate basis of the birefringence induced by the signal, which does not in general coincide with the laboratory frame. While a result in the lab frame can be computed the solution numerically, an analytical answer can be approximated with this approach.

The broadband laser is regarded as a monochromatic wave with frequency given by it's center wavelength $\lambda_0 = 800$ nm ($\omega_0 \approx 2.35$ Prad/s) and the THz signal to be near-DC ($\omega_{THz} \rightarrow 0$). Again returning to Maxwell's equations, Eq. (3.7) with first and second order polarizations is written

$$\nabla \times \nabla \times \mathbf{E}_t(\mathbf{r}) + \frac{1}{c^2}\frac{\partial^2 \mathbf{E}_t(\mathbf{r})}{\partial t^2} = -\frac{1}{\epsilon_0 c^2}\frac{\partial^2 \mathbf{P}_t(\mathbf{r})}{\partial t^2} \tag{4.23}$$

$$= -\frac{1}{\epsilon_0 c^2}\frac{\partial^2}{\partial t^2}\left[\mathbf{P}_t^{(1)} + \mathbf{P}_t^{(2)}\right] \tag{4.24}$$

For each we use a t and z dependence $\mathbf{E}_t(z) = \widetilde{\mathbf{E}}_\omega e^{k(\omega)z-i\omega t} +$ c.c. and note that to first order the polarization is isotropic. We denote the THz frequency as $\omega_{THz} = \Omega$. From Eq. (4.21) and (4.22) we see that for finite Ω we will have solutions at two waves with frequencies $\omega_\pm = \Omega \pm \omega$ indicating the generation of sidebands.

$$\begin{aligned} \mathbf{k}_+ \times \mathbf{k}_+ \times \widetilde{\mathbf{E}}_{\omega_+} + \frac{\left(1+\chi^{(1)}_{\omega_+}\right)\omega_+^2}{c^2}\widetilde{\mathbf{E}}_{\omega_+} &= -\frac{2\tilde{E}_\Omega \omega_+^2}{c^2} \exp\{i\left[k(\Omega)+k(\omega)-k(\omega_+)\right]z\}\,\chi^{(2)}_{eff}(\theta)\cdot\widetilde{\mathbf{E}}_\omega \quad (4.25)\\ \mathbf{k}_- \times \mathbf{k}_- \times \widetilde{\mathbf{E}}_{\omega_-} + \frac{\left(1+\chi^{(1)}_{\omega_-}\right)\omega_-^2}{c^2}\widetilde{\mathbf{E}}_{\omega_-} &= -\frac{2\tilde{E}_\Omega \omega_-^2}{c^2} \exp\{i\left[k(\Omega)-k(\omega)-k(\omega_-)\right]z\}\,\chi^{(2)}_{eff}(\theta)\cdot\widetilde{\mathbf{E}}^*_\omega \quad (4.26) \end{aligned}$$

For a very narrow-band probe laser and finite Ω, these yield solutions for what is known as electro-optic upconversion [78, 79]. In our DC limit where $\Omega \ll \omega$, $\omega_\pm \to \pm\omega$. Noting that $k(\Omega) = n(\Omega)\Omega/c \to 0$ and using our real monochromatic wave with $\widetilde{\mathbf{E}}^*_\omega = \widetilde{\mathbf{E}}_{-\omega}$ and $k(-\omega) = -k(\omega)$, these become

$$\begin{aligned} \mathbf{k}\times\mathbf{k}\times\widetilde{\mathbf{E}}_\omega + \frac{\left(1+\chi^{(1)}_\omega\right)\omega^2}{c^2}\widetilde{\mathbf{E}}_\omega(\mathbf{r}) &= -\frac{2E_\Omega\omega^2}{c^2}\chi^{(2)}_{eff}(\theta)\cdot\widetilde{\mathbf{E}}_\omega \quad (4.27)\\ \mathbf{k}\times\mathbf{k}\times\widetilde{\mathbf{E}}^*_\omega + \frac{\left(1+\chi^{(1)}_\omega\right)\omega^2}{c^2}\widetilde{\mathbf{E}}^*_\omega(\mathbf{r}) &= -\frac{2E_\Omega\omega^2}{c^2}\chi^{(2)}_{eff}(\theta)\cdot\widetilde{\mathbf{E}}^*_\omega \quad (4.28) \end{aligned}$$

which are simply complex conjugates of each other. In this form we can treat Eq. (4.27) in the same manner as we did for the first-order birefringent materials in Sec. 3.4. Eq. (3.66) becomes

$$\left\{(\mathbf{k}\times\mathbf{k}\times) + \frac{\omega^2}{c^2}\left[n_o^2\boldsymbol{I} + 2E_\Omega\chi^{(2)}_{eff}(\theta)\cdot\right]\right\}\widetilde{\mathbf{E}}_\omega = 0 \quad (4.29)$$

with $n_o^2 = 1 + \chi^{(1)}_\omega$ and $\boldsymbol{I}$ the identity matrix. If we also scale $\mathbf{k}$ by ω/c by defining $\mathbf{n}$ in the same direction as $\mathbf{k}$ with magnitude from $n = kc/\omega$ we can normalize this as

$$\left\{(\mathbf{n}\times\mathbf{n}\times) + \left[n_o^2\boldsymbol{I} + 2E_\Omega\chi^{(2)}_{eff}(\theta)\cdot\right]\right\}\widetilde{\mathbf{E}}_\omega = 0 \quad (4.30)$$

Noting that our applied field has wavevector $\mathbf{k} = k\hat{z}$, we can find the modified index n as before by writing out the matrix of (4.30)

$$\begin{pmatrix} n_o^2 + 2E_\Omega\,\chi^{(2)}_{eff,11} - n^2 & 2E_\Omega\,\chi^{(2)}_{eff,12} & 0 \\ 2E_\Omega\,\chi^{(2)}_{eff,12} & n_o^2 + 2E_\Omega\,\chi^{(2)}_{eff,22} - n^2 & 0 \\ 0 & 0 & n_o^2 + 2E_\Omega\,\chi^{(2)}_{eff,33} - n^2 \end{pmatrix}\begin{pmatrix} E_{\omega,x} \\ E_{\omega,y} \\ E_{\omega,z} \end{pmatrix} = 0 \quad (4.31)$$

where $\chi^{(2)}_{eff,ij}$ are the θ-dependent elements of $\chi^{(2)}_{eff}(\theta)$ given by Eq. (4.20). We again have an eigenvalue problem, this time defined in the effective index n^2. Setting the determinant of the matrix of coefficients equal to zero and inserting the elements given by Eq. (4.20) yields three eigenvalues we denote $n_\pm^2$ and n_3^2

$$n_\pm^2 = n_o^2 + \left(\cos\theta \pm \sqrt{1 + 3\sin^2\theta}\right)\chi^{(2)}E_\Omega \tag{4.32}$$

$$n_3^2 = 2\cos\theta\,\chi^{(2)}E_\Omega \tag{4.33}$$

The eigenvector associated with n_3 is (0,0,1), indicating an induced polarization along z. This implies a spatial walk off as before, which we neglect for our thin crystal.

As the second order coupling is weak compared to the dispersion ($\chi^{(2)}E_\Omega \ll n_o^2$), to first order the $n_\pm$ indices can be expanded as

$$n_\pm \approx n_o + \frac{\chi^{(2)}E_\Omega}{2n_o}\left(\cos\theta \pm \sqrt{1 + 3\sin^2\theta}\right) \tag{4.34}$$

For comparison to the literature, we insert the conventionally cited Kleinman coupling parameter which is $\chi^{(2)} = 2d_{14}$. We then find that the induced birefringence $\Delta n = n_+ - n_-$ is

$$\Delta n = \frac{4d_{14}E_\Omega}{n_o}\frac{\sqrt{1 + 3\sin^2\theta}}{2} \tag{4.35}$$

so that the induced birefringence is proportional to

$$\Delta n \propto E_\Omega\frac{\sqrt{1 + 3\sin^2\theta}}{2} \tag{4.36}$$

in agreement with [64, 69]. In our case the solution scales with $4d_{14}E_\Omega/n_o$ instead of $r_{41}E_\Omega n_o^3$. This comes from the choice of working with the susceptibility and not the impermeability tensor, which are inversely related [51] with, $d_{14}E_\Omega$ related to Δn^2 whereas for $r_{41}E_\Omega$ it is $1/\Delta n^2$.

We can continue the solution and solve for the eigenvectors associated with these solutions, which again yield the same θ dependence as in [64, 69]. The angle α of the induced optic axis is found to vary as a function of the crystal rotation. The induced retardance Γ is proportional to Δn (Eq. (3.76)) above so that this is also a function of θ. To compose the Jones matrix **EO** of this effective waveplate one must then first transform the birefringence to the lab system as

$$\mathbf{EO}(\theta) = \mathbf{R}[\alpha(\theta)] \cdot \begin{pmatrix} \exp\left[i\Gamma(\theta)/2\right] & 0 \\ 0 & \exp\left[-i\Gamma(\theta)/2\right] \end{pmatrix} \cdot \mathbf{R}[-\alpha(\theta)] \tag{4.37}$$

One finds this does not readily simplify in θ, though the trend can be plotted numerically [69].

To find an approximate analytical solution we make a small birefringence approximation in Eq. (4.31) by assuming the on-diagonal terms are dominated by the first order index of refraction. Neglecting the on-diagonal $\chi^{(2)}_{11}$ and $\chi^{(2)}_{22}$ terms this yields

$$\begin{pmatrix} n_o^2 - n^2 & 2E_\Omega \chi^{(2)}_{eff,12} & 0 \\ 2E_\Omega \chi^{(2)}_{eff,12} & n_o^2 - n^2 & 0 \\ 0 & 0 & n_o^2 - n^2 \end{pmatrix} \begin{pmatrix} E_{\omega,x} \\ E_{\omega,y} \\ E_{\omega,z} \end{pmatrix} = 0 \tag{4.38}$$

for which the determinant equation in $x - y$ immediately yields the solutions in terms of d_{14}

$$n_\pm^2 = n_o^2 \pm 4d_{14}E_\Omega \left(2\sin\theta - 3\sin^3\theta\right) \tag{4.39}$$

with associated eigenvectors in the laboratory basis that are exactly

$$\hat{n}_\pm = \begin{pmatrix} \frac{1}{\sqrt{2}} \\ \pm\frac{1}{\sqrt{2}} \end{pmatrix} \tag{4.40}$$

We see that the induced optic axes then lie at 45° from the x and y axes, just as a circular polarizer. To first order the strength of the retardance is found from Δn to be

$$\Delta n = 4d_{14}E_\Omega \left(2\sin\theta - 3\sin^3\theta\right) \tag{4.41}$$

which yields again a retardance $\Gamma(\theta)$ per unit length proportional to $\Delta n(\theta)$, as given by Eq. (3.76). In the Jones calculus this is the operator

$$\mathbf{EO}(\theta) = \mathbf{R}(45^\circ) \cdot \begin{pmatrix} \exp\left[i\Gamma(\theta)/2\right] & 0 \\ 0 & \exp\left[-i\Gamma(\theta)/2\right] \end{pmatrix} \cdot \mathbf{R}(-45^\circ) \tag{4.42}$$

For our laser initially polarized in x, we find after the EO crystal

$$\widetilde{\mathbf{E}}'_{\omega}(\theta) = \mathbf{EO}(\theta) \cdot \begin{pmatrix} 1 \\ 0 \end{pmatrix} \tilde{E}_{\omega} = \begin{pmatrix} \cos\left[\Gamma(\theta)/2\right] \\ i \sin\left[\Gamma(\theta)/2\right] \end{pmatrix} \tilde{E}_{\omega} \tag{4.43}$$

If we immediately split these two polarization components, measure their intensities ($|\tilde{E}_{\omega}|^2$) then take the difference over the sum to find a measured signal $S_{lin}(\theta, \omega)$

$$S_{lin}(\theta) = \frac{|\widetilde{E}'_{\omega,x}|^2 - |\widetilde{E}'_{\omega,y}|^2}{|\widetilde{E}'_{\omega,x}|^2 + |\widetilde{E}'_{\omega,y}|^2} \tag{4.44}$$

$$= \frac{\cos^2\left[\Gamma(\theta)/2\right] - \sin^2\left[\Gamma(\theta)/2\right]}{\cos^2\left[\Gamma(\theta)/2\right] + \sin^2\left[\Gamma(\theta)/2\right]} \tag{4.45}$$

$$= \cos[\Gamma(\theta)] \tag{4.46}$$

Which is similar to Eq. (4.47), but now with the crystal orientation dependence as

$$\Gamma(\theta) = \left(2\sin\theta - 3\sin^3\theta\right)\Gamma_0 \tag{4.47}$$

with $\Gamma_0 \propto L\tilde{E}_{THz}$, where L is the crystal thickness.

We can also introduce the circular polarizer before splitting and measuring the polarizations as we do in our setup. This then has the signal taking a form similar to Eq. (4.5) as

$$S_{circ}(\theta) = -\sin[\Gamma(\theta)] \tag{4.48}$$

For comparison, we can follow the same procedure to compute the measured signals $S(\theta)$ numerically using the eigenvalue and eigenvectors provided by [64, 69]. We take the amplitude of the retardance $\Gamma_0 = 0.4$ for each and plot the angular dependence in Fig. 4.8 for the cases with and without the circular polarizer.

From Fig. 4.8 we see that the coupling is strongest for $\theta_{max} = 90°, 270°$. A comparison in the maximum induced change in the amplitude for the two arrangements also suggests a larger signal when measuring with the circular polarizer.

The estimate of the on-diagonal of $\chi^{(2)}$ tied to SFG having little effect on the induced retardance appear to hold based on this comparison. This is identically true at θ_{max} where the on-diagonal terms vanish. Finally we observe that the angular dependence of the signal coupling appears similar to the apparent rotational symmetry of the crystal viewed in the direction of signal and probe propagation seen in Fig. 4.6 which is that of a pinched regular hexagon.

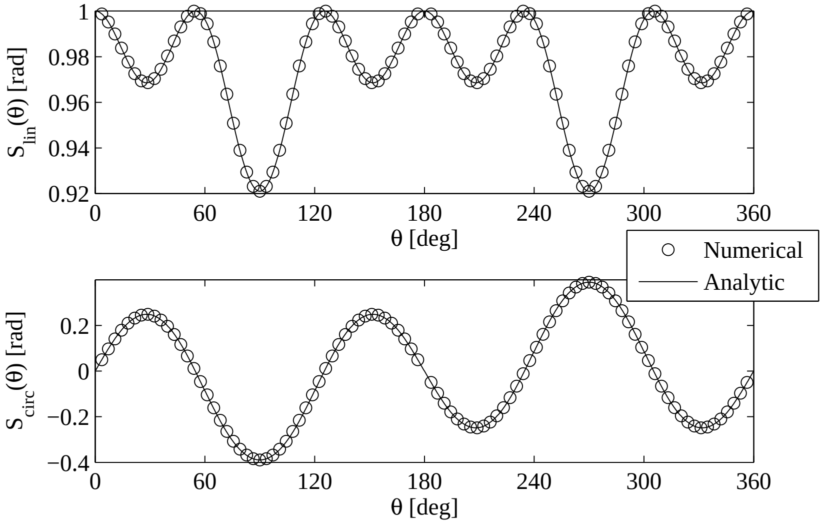

Figure 4.8: EO signal strength as a function of crystal rotation angle θ using numerical solutions from [64, 69] as compared to analytical approximations using Eq. (4.46), (4.48), and (4.47) measured after the EO crystal (top) and with a circular polarizer prior to measurement (bottom) for a retardance amplitude of Γ_0 = 0.4

4.4.3 Spectral decoding approximation

With the geometric coupling between the polarizations determined, we now insert the approximation for EOSD. Both our chirped laser pulse and THz signal have a finite bandwidth and temporal extent. As stated in Sec. 4.1, to first order we therefore assume that each frequency component sees only a birefringence with a strength proportional to the transient of the signal that coincides with the group delay $\tau(\omega)$ with that frequency component. From the preceding section we then introduce

$$d_{eff}(\theta) = \left(2\sin\theta - 3\sin^3\theta\right) d_{14} \tag{4.49}$$

In summary our signal (using our quarter waveplate) is given by the equations

$$S(\theta, \omega) = -\sin\left[d_{eff}(\theta)\Gamma(\omega)\right] \tag{4.50}$$

$$\Gamma(\omega) \propto E_{THz}\left[\tau_g(\omega)\right] \tag{4.51}$$

$$\tau_g(\omega) = \frac{\partial \phi}{\partial \omega} \approx D_2(\omega - \omega_0) \tag{4.52}$$

$$\tag{4.53}$$

where D_2 is the group delay dispersion of our linearly chirped laser pulse (Sec. 3.3). By measuring Γ and converting the frequency axis to time via $\tau_g(\omega)$, we can determine $E_{THz}(t)$.

This assumes that the two pulses stay velocity matched with each other while propagating the full length of the crystal. This may not be true of the index of refraction at the very different wavelengths is significantly different. It further assumes that dispersion does not cause appreciable distortion to either the probe or signal. These can be violated if the material dispersion is strong enough over the range of frequencies covered by the probe and signal spectra.

4.4.3.1 Dispersion effects

In the case studied by [66, 69], the effect of dispersion in ZnTe for a 15-fs laser pulse and THz pulse with a duration of 67 fs were studied. Significant distortion of the THz signal was observed owing to the power spectra extending up to the high-frequency limit of the crystal. Similarly, significant broadening of the large-bandwidth laser pulse was observed due to a comparatively large GDD (see Sec. 3.3).

We repeat this analysis for our less demanding case of a 100-fs laser pulse with expected bunch durations on the order of 1 ps. We see from Eq. (3.52) that the temporal profile of the pulses vary along z via a Fourier transform of the initial spectrum multiplied by an exponential factor related to z and the wavevector $k(\omega)$ which is in turn related to the index of refraction. We can numerically compute $n(\omega)$ as well as the discrete Fourier transform (DFT) so this can be written

$$E_t(z) = DFT\left\{\tilde{E}_\omega(0)\exp\left[i\frac{n(\omega)\omega}{c}z\right]\right\} \tag{4.54}$$

for which we need the form of $n(\omega)$.

The complex index of refraction for ZnTe in the THz regime $\tilde{n}_{THz}(\nu)$ is [66, 69]

$$\tilde{n}_{THz}(\nu) = \epsilon_{el} + \frac{S_0 \nu_0^2}{\nu_0^2 - \nu^2 - i\Gamma_0 \nu} \tag{4.55}$$

with the parameters $\epsilon_{el} = 7.4$, $S_0 = 2.7$, $\nu_0 = 5.3$ THz, and $\Gamma_0 = 0.09$ THz. In the IR regime we have for n_{IR}

$$n_{IR}(\lambda) = \sqrt{4.27 + \frac{3.01\lambda^2}{\lambda^2 - .142}} \tag{4.56}$$

where λ is given in µm. These are plotted in Fig. 4.9 over the THz and IR regimes with the complex index written in terms of its real and complex components n and κ as

$$\tilde{n}(\nu) = n(\nu) + i\kappa(\nu) \tag{4.57}$$

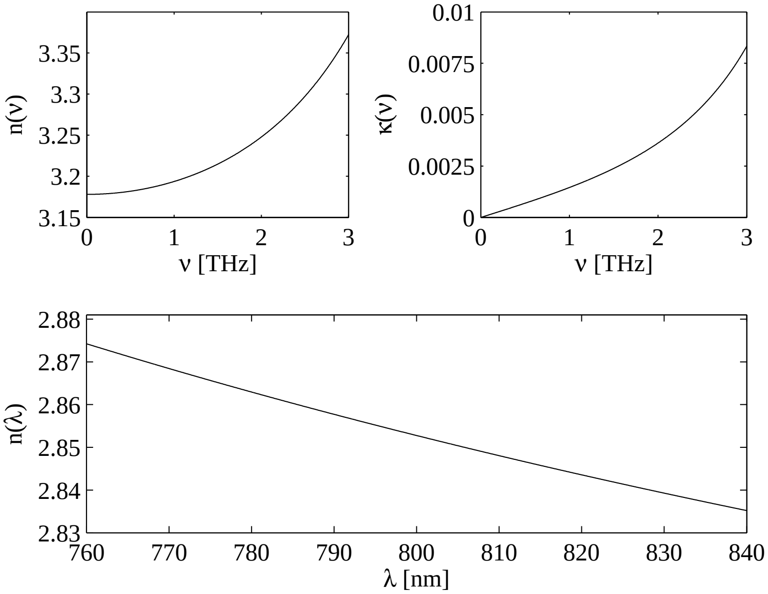

Figure 4.9: Indices of refraction for ZnTe in the THz (top) and near IR (bottom) regimes (Eq. (4.55) and (4.56)). In the THz regime this is plotted as the real and complex components $n(\nu)$ and $\kappa(\nu)$.

Using these and Eq. (4.54) we can compute the propagation of the two pulses through the crystal. As shown in [30, 66, 69], one can use these to compute an effective frequency response for the crystal. For 1 mm-thick ZnTe the FWHM high-frequency limit is found to be $\nu_{max} \approx 2.5$ THz. This corresponds to an approximate temporal resolution of ~200 fs, RMS.

To see the effect, first we consider a 1 ps, FWHM transient propagation through the crystal with our Ti:sapph laser pulse which has been chirped to an intensity FWHM of 3.5 ps. The corresponding transients after propagating a distance L through the crystal in 0.2-mm steps up to our full crystal thickness of 1 mm are shown in Fig. 4.10.

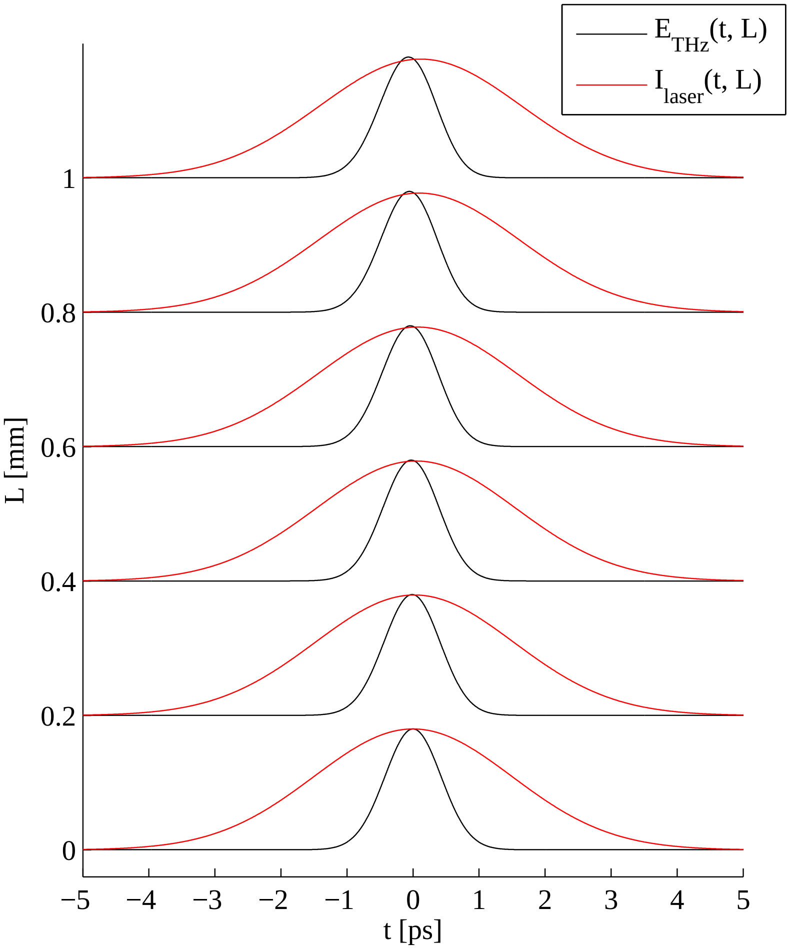

Figure 4.10: Propagation in ZnTe of a 1-ps Gaussian transient (black) with the Ti:sapph pulse linearly chirped to a length of 3.5 ps (red). The vertical offsets indicate the propagation length L at which the transients are computed using Eq. (4.54). The head of the signals in time is to the left, tails to the right. Relative temporal offsets of the pulses is preserved.

Fig. 4.10 shows very little distortion to either transient in this case. However there is a slight group velocity mismatch observed after the full length $L = 1$ mm with the THz pulse leading the laser pulse by 180 fs. As the retardation occurs over the full propagation length, we see that the components of the laser will sample a sliding window along the THz transient, consistent with the expected time resolution. Furthermore, distortion to the laser pulse is minimal compared to the pulse length with a broadening of 85 fs. For the THz pulse, the temporal width changes by <10 fs.

This is a highly idealized case. For further illustration we look at the so-called "spiked bunch." The spiked bunch can occur in the electron beam when second-order chromatic (energy-dependent) effects of the beam optics are considered, generating a distribution with a spiked head and longer tail.

For good measure we also consider the low-frequency losses discussed in Sec. 2.4, in particular as shown in Fig. 2.7.

For this simulation then, we generate the signal from an arbitrary spiked bunch distribution as shown in Fig. 4.11. The distribution is transformed, the square-root of the amplitude response from Fig. 2.7 is applied to the complex field generating the low-frequency losses, and the result is transformed back to the time domain.

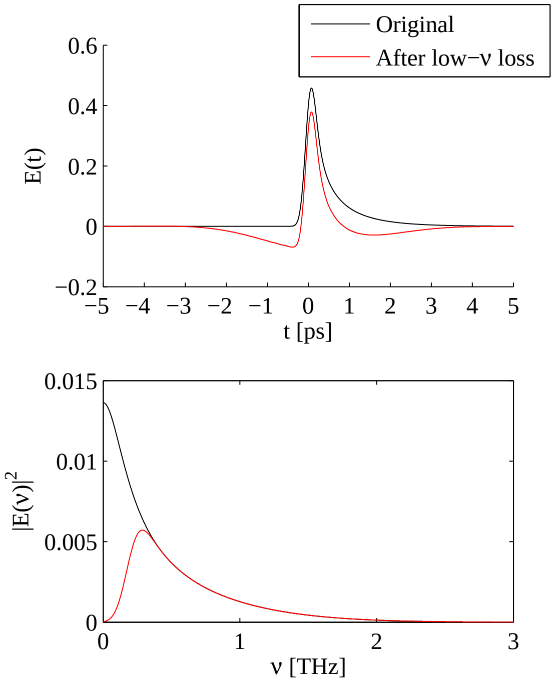

Figure 4.11: The transient of an arbitrary spiked distribution signal in time (top) and corresponding power spectra (bottom). Black curves indicate original signal with red after applying low-frequency losses shown in Fig. 2.7

This now generates a signal with somewhat higher frequency content with a portion of the tail extending beyond the 2.5 THz limit of the crystal. Further, we see that the effect of the DC losses cause the signal to effectively "sink." That is, the original distribution appears to rest within a long, slow dip, allowing the signal to go negative.

We then do as before and propagate this signal through the thickness of the ZnTe crystal, as shown in Fig. 4.12. With respect to the peak values, the THz signal advances on the laser only 60 fs in this case. However, an additional ringing in the transient tail is observed. The short peak is seen to slowly broaden and evolve into a quickly oscillating tail. Such features are observed whenever the signal has temporal structure with a periodicity greater than the 2.5 THz cutoff of the thick crystal. The analysis of [66, 69] demonstrated similar ringing with thinner crystals but where much shorter signals were applied.

Finally, we note that the slow oscillation generated by the DC losses does not appear to translate into any dramatic effect. This is to be expected as the frequency of such structure is well-within the flat response region below 2.5 THz.

4.4.3.2 Chirped pulse distortions

The goodness of the spectral encoding approximation continues to be studied. An effective time resolution for the measurement

$$\tau_{res} = \sqrt{\tau_o \tau_c} \tag{4.58}$$

where τ_o is the transform-limited laser pulse length and τ_c is the chirped laser pulse has been suggested [80–82]. Where the probe pulse is stretched further, the signal measured begins to become a distorted replica of the signal.

To see the effect, we consider that at every point along z, the induced retardance must in fact be summed over the full spectrum of the THz field. Following the treatments of [51, 67, 76] using the slowly-varying envelope approximation, the infinitesimal change to the frequency content of the probe laser with initial polarization in x after a length L is given by the sum-frequency generation integral

$$\begin{aligned} \Delta\tilde{E}_x(\omega) &\approx \frac{2i\omega L}{cn(\omega)} d_{eff}(\theta) \int_{-\infty}^{\infty} \tilde{E}_{THz}(\omega')\tilde{E}_x(\omega-\omega') \left\{ e^{i\Delta k(\omega,\omega')L/2} \mathrm{sinc}\left[\Delta k(\omega,\omega')L/2\right] \right\} d\omega' && (4.59) \\ \Delta k(\omega,\omega') &= k(\omega') + k(\omega-\omega') - k(\omega). && (4.60) \end{aligned}$$

Note that (assuming $\Delta k \ll 1$) the SFG field grows linearly with crystal thickness L so that the intensity of the signal should grow as L^2. This growth is of course only true where the generated signal remains small

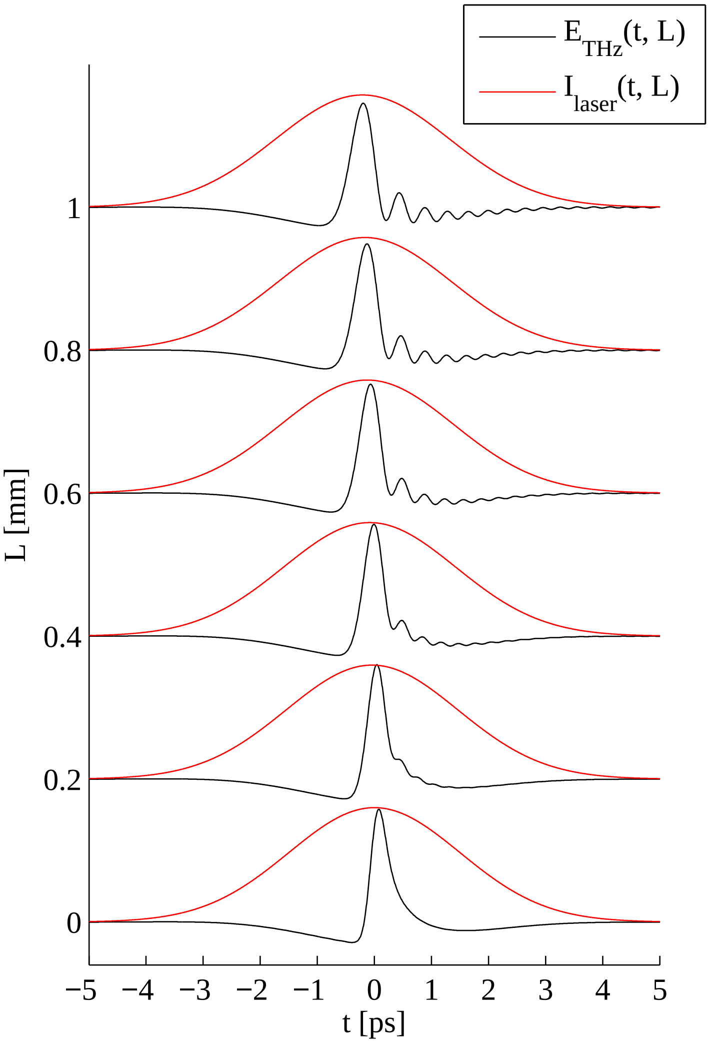

Figure 4.12: Propagation in ZnTe of the DC-suppressed spiked distribution of Fig. 4.11 (black) with the Ti:sapph pulse linearly chirped to a length of 3.5 ps (red). The vertical offsets indicate the propagation length *L* at which the transients are computed using Eq. (4.54). The head of the signals in time is to the left, tails to the right. Relative temporal offsets of the pulses is preserved.

compared to the THz and laser fields beyond which point depletion of these sources sets in, diminishing signal growth.

From the cross-coupling of the polarizations above, we expect an equal and opposite change to the spectrum in the y polarization so that after the ZnTe crystal we have

$$\begin{pmatrix} \tilde{E}_x'(\omega) \\ \tilde{E}_y'(\omega) \end{pmatrix} = \begin{pmatrix} \tilde{E}_x(\omega) + \Delta\tilde{E}_x(\omega) \\ -\Delta\tilde{E}_x(\omega) \end{pmatrix} \tag{4.61}$$

The usual Jones matrix analysis for the subsequent quarter-wave plate and polarizer can then be used to analyze the signal from the difference over the sum of the intensities. We consider then another example of a spiked bunch with low-frequency losses where there are negligible distortions to the signal itself from dispersion. This time we compute the signal numerically using Eq. (4.59) and (4.61) and perform the map to the time axis using our knowledge of the group delay $\tau_g(\omega)$, as would be done in a measurement.

Our signal has an initial FWHM of 1 ps. Again applying the low frequency losses of Fig. 2.7, we then propagate through 1 mm of ZnTe with the result shown in Fig. 4.13. The signal appears relatively unaltered.

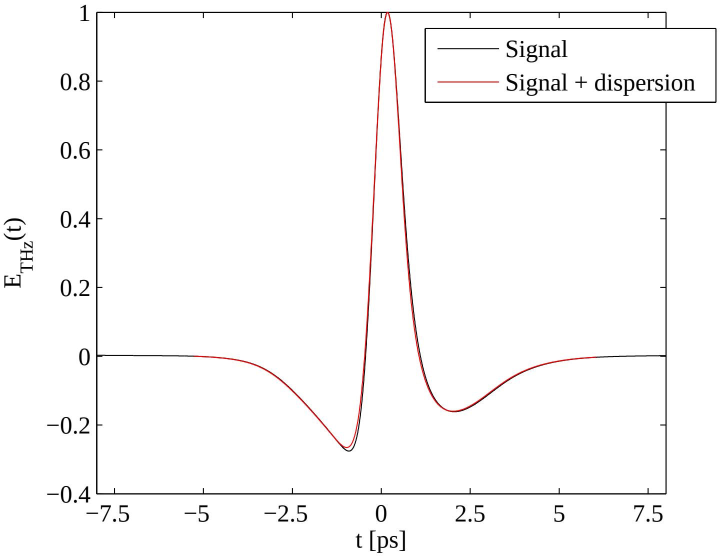

Figure 4.13: Test signal used to simulate EOSD without dispersion (black) and after propagating through 1 mm of ZnTe (red). Original signal is 1 ps FWHM in duration.

To envelope the entire signal, a minimum laser pulse duration of 2 ps is suggested though longer may be preferred, for example, to establish the tail. Simulations using Eq. (4.59) and (4.61) are performed to show the effect of chirp on the measured signal. We start with our Fourier-limited 100-fs pulse. We then compute the signal that would be measured for laser pulses with chirped durations varying from 2 ps to 8 ps in 1.5 ps steps, shown in Fig. 4.14 in comparison to the original signal.

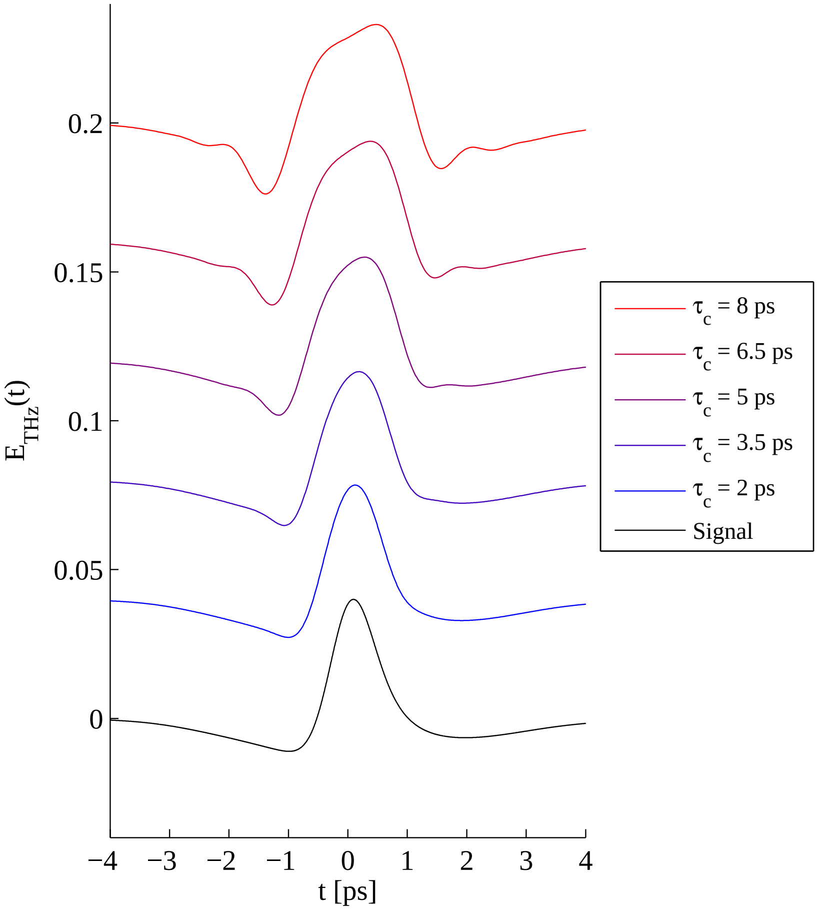

Figure 4.14: Simulations of the signal that would be recovered by EOSD as compared to the original (black, bottom) using varying laser durations τ_c = 2 ps to 8 ps in 1.5 ps steps, from bottom to top. Initial laser pulse duration τ_o = 100 fs. (Vertical offsets arbitrary.)

As we see, if one over-chirps the laser pulse, significant distortions begin to set in. Therefore we require that the laser be stretched as little as possible to envelop the time window of interest to avoid sacrificing temporal resolution.

An attempt to circumvent this via numerical deconvolution by matrix inversion was suggest by Yellampalle, *et al* [77]. This was subsequently met with only partial experimental success on real data [68]. In our own case the algorithm was attempted using the data presented in this paper, but numerical noise was found to dominate the recovered signals. Further the reconstruction approach suggested does not account for the effects of velocity mismatch in the crystal, which we have shown in the preceding section to produce significant distortion when the signal has fine time structure.

So far we have assumed that our laser system is well-synchronized to the CTR pulse, that is to say, both the accelerator and the Nd:YLF drive laser. Where there is some additional shot-to-shot variation in their time of arrival we are forced to extend the chirp of the laser further to keep the signal within our temporal field of view. This can adversely impact the effective time resolution given by Eq. 4.58.

We have additionally presupposed good knowledge of the laser's spectral amplitude and phase for decoding the signal. This however remains to be measured.

To verify these, we now turn to a rigorous analysis of the laser including details on the synchronization electronics used, their performance, and a time-frequency domain analysis of the Ti:sapph laser probe.

CHAPTER 5

LASER SYNCHRONIZATION AND CHARACTERIZATION

To consistently see the beam's full longitudinal profile, we must minimally stretch the pulse to the electron bunch length plus some additional tolerance for shot-to-shot temporal fluctuations so that the signal being measured is within our effective temporal field of view. To maintain sub-picosecond time resolution in the chirped pulse approximation, as given by Eq. (4.58), we find that these fluctuations must be reduced to 1 ps or less.

For our alternative use of the Ti:sapph system as drive laser (Sec. 2.6), the UV output must be synchronized to the L-band RF gun to within at least 1° of the accelerator RF (2 ps), a less stringent requirement.

In this chapter we discuss how synchronization of the Ti:sapph laser system was accomplished and verify that the solution found meets the above requirements. We will also address potential intensity instabilities that can be introduced by unstable triggering of the 1-kHz pulse selection in the Ti:sapph regenerative amplifier (regen). We conclude with measurements of the temporal properties of the individual pulses.

Synchronization with the accelerator requires management of two time scales. The first is ns-scale synchronization of the regen amplifier to the photoinjector 1-Hz event that triggers the accelerator's RF pulse forming network and instrumentation. The regen selects a 1-kHz train of pulses from the 81.25-MHz seed train with the ability to gate any subset of this train. A 1-kHz trigger must be provided to select these pulses at the same time as the 1-Hz event so that both choose the same RF cycle from their higher harmonics. This ensures regular timing of the laser with respect to the gun RF pulse and data acquisition from shot to shot.

The second time scale is fs-scale synchronization of the seed laser 81.25-MHz pulse train to the 1.3-GHz master oscillator that drives the photoinjector RF. This drives the stability of the launch phase at the photocathode when operating in UV drive laser mode and beam-probe laser jitter in the context of EOSD.

As EOSD is to be performed on beam generated using the existing Nd:YLF laser system, good cross-synchronization of the two lasers is as important as timing to the accelerator. The timing of both laser systems are therefore examined.

We discuss the fine temporal stability in the usual parameters of jitter and drift. Jitter refers to the spread of fast, shot-to-shot fluctuations in the output time difference of the seed laser with respect to some reference signal. This is typically less than 1 ps. Drift is the change in the mean time difference from a reference signal over extended periods, of the order ps/hour.

5.1 Coarse triggering of the Ti:sapph amplifier

With the Ti:sapph regen's fine synchronization driven primarily by that of the seed laser, we first look at coarse timing of its 1-kHz repetition rate to the 1-Hz A0PI clock. The 1-kHz trigger is used by the *Dazzler* and *Spitfire* timing electronics to determine which pulses in the 81.25-MHz seed laser pulse train to capture for shaping and amplification.

As the gun RF is fed by an RF macropulse with 400 µs maximum duration and some instrumentation (e.g. beam position monitors) only diagnose the first bunch in each macropulse, only one pulse of a given 1000-pulse regen cycle is relevant to beam physics experiments at the photoinjector.

A block diagram of the full synchronization scheme is shown in Fig 5.1. The 81.25-MHz seed laser output is internally synchronized to the 16th subharmonic of the 1.3-GHz master oscillator. Where additional fine temporal phase monitoring and control are needed, a secondary, external PLL has been added. Details on this are described later in Sec. 5.2.3 with the secondary, external PLL illustrated in Fig. 5.10.

For slow trigger generation the 81.25-MHz sub-master is further divided down to 9.028 MHz and used as the clock for two digital counter synthesizers integrated on a system of field programmable gate arrays (FPGA). The first of these is the existing 10-Hz signal generator and count-down dividers providing 5-, 2- and 1-Hz signals. The signal generator selects the 10-Hz to be in phase with the building's 60-Hz AC.

The 1-kHz trigger is generated by upsampling of the slower 10-Hz clock. This 1-kHz signal fires the regen's Q-switched pump laser, the regen pulse-picking Pockels cells, and the *Dazzler* pulse shaper.

A µs-scale instability is introduced by this synchronization of the 10 Hz to the 60-Hz main line. As will be demonstrated throughout this section, this adds a number of complications to the triggering system with regards to 1-kHz trigger generation, *Dazzler* timing requirements, and the stability of the regen pump laser.

The *Dazzler* diffracts the shaped laser pulse train into the regen cavity for amplification by loading a 33 µs-duration acoustic waveform into the AOPDF. The electronics to load the waveform must be triggered 25 µs before the regen system. Therefore the 1-kHz trigger must provide two output channels with independent time delays to allow the *Dazzler* to be fired in advance of the regen. Where a 1-kHz clock stable to the microsecond is available, this becomes unnecessary as the *Dazzler* can instead be configured to trigger on delay of the previous pulse in the train.

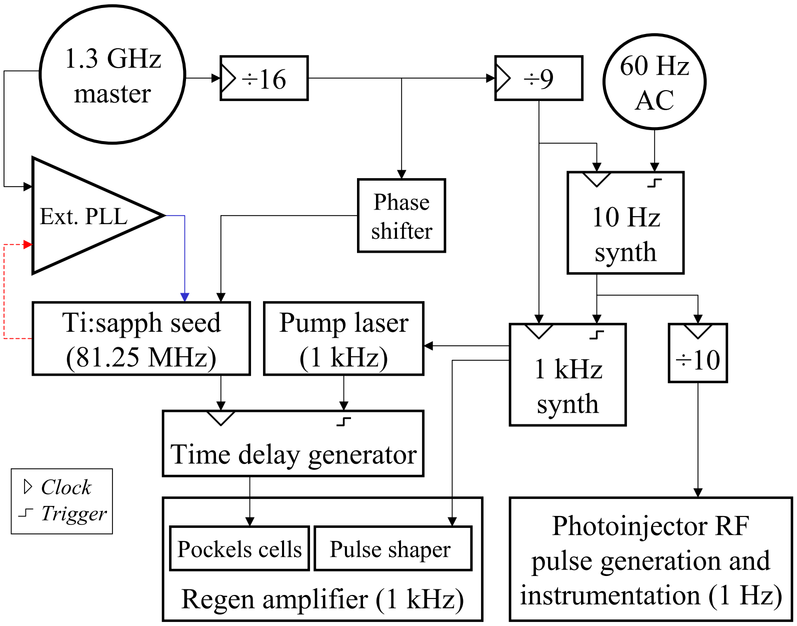
1.3 GHz master
÷16
÷9
60 Hz AC
Ext. PLL
Phase shifter
10 Hz synth
Ti:sapph seed (81.25 MHz)
Pump laser (1 kHz)
1 kHz synth
÷10
Time delay generator
Clock
Trigger
Pockels cells
Pulse shaper
Regen amplifier (1 kHz)
Photoinjector RF pulse generation and instrumentation (1 Hz)

Figure 5.1: Block diagram of timing scheme used to synchronize the Ti:sapph laser system to the photoinjector.

For the Pockels cells, the 1-kHz event is synchronized by the time delay generator (TDG) to be locked with the 81.25-MHz signal of the seed laser for pulse selection. A 1-Hz, 1 ms-duration logical signal is then used to gate only the 1-Hz pulses on-time with the gun RF pulse.

The coarse, 1-kHz trigger signal has been derived passively using a signal generator as well as actively using a preferred custom trigger synthesizer built on an Altera (part no. EPF10K40RC208-3) FPGA for our purposes.

5.1.1 1-kHz burst generation

In the simplest case, an externally triggered signal generator operating in burst mode can produce a train of 1-kHz pulses fired at each 1-Hz event to produce a steady signal. The burst generator is set to fire a fixed number of pulses at a fixed frequency of approximately 1-kHz sufficient to fill the time between slow trigger events.

If at any time a trigger event occurs before a previous pulse train completes firing, that event is ignored by the signal generator causing it to remain low until the following macropulse event. This gap in triggering will cause an under-frequency protection fault in the amplifier pump laser, disabling the regen. Therefore for uninterrupted operation, one must choose the pulse generator's macropulse duration (product of number of cycles and repetition rate) to be smaller than the shortest possible trigger period.

As stated above, this becomes difficult in our case due to the slow frequency fluctuations driven by the dependence of the low repetition rate clocks on the 60-Hz main voltage. Twenty-four hour recording of the period for these, as accumulated with an oscilloscope, reveal that the 1-Hz clock period can vary as much as ±2.5 ms from the nominal 1 s. If the macropulse from the signal generator is set to a 997.5 ms duration there can then be as much as 5 ms of dead time in the limiting case. This is again sufficient to generate an under-frequency fault in the regen pump laser.

We instead upsample the 10-Hz signal which accumulates a smaller phase difference from 60-Hz frequency deviations between clock resets. Measurement over 8-hours shows the 10-Hz period varying up to only 120 µs from the nominal 100 ms with a root-mean-squared (RMS) deviation of 30 µs. This allows for a burst generator operating with 100 pulses at 1.0012 kHz to have a maximum dead time of 1.24 ms for any given shot, sufficient to maintain laser operation.

5.1.2 Intensity dependence on unstable triggering

Using the above burst generator as the 1-kHz trigger means allowing the period before the first cycle in each burst to vary several tens of microseconds. This unstable repetition rate can adversely affect the *Empower* and, therefore, amplified IR output.

The explanation for the transient response from a sudden change in repetition rate can be understood in terms of the population inversion seen from one shot to the next [83]. After a pulse is emitted there is some residual inversion left in the Q-switched cavity. This will then build back up over the pumping period to a new initial inversion before the Q-switch is reopened for pulsing, dropping the inversion down to a new residual.

For a constant pumping period, the initial and residual inversions will reach a steady state. However, a sudden change in this period will temporarily disrupt this as some additional (or lesser) inversion is built up before the next pulse is emitted.

The effect of *Empower* repetition rate on the output power and pulse shape of the Q-switched laser can be modeled with detailed knowledge of cavity properties such as upper state lifetime of the lasing medium, cavity decay rate, inversion threshold and pumping rate [83, 84]. The simple numerical model for a repetitively Q-switched laser suggested in [83] illustrates that for parameters typical of a Nd:YLF system, reasonably steady-state output is reached within the first 2–3 cycles after a change in repetition rate.

The Q-switched build-up time τ_n associated with any n-th pulse will be related to the preceding build-up time τ_{n-1}. For our burst generator configuration we have

$$\tau_n = \begin{cases} \tau_{kHz} & \text{for } n \neq N \\ \tau_{Trig} - (N-1)\tau_{kHz} & \text{for } n = N \end{cases} \tag{5.1}$$

where $\tau_{kHz} \approx 1$ms is the burst generator period, $N = 100$ is the number of pulses in a macropulse, and $\tau_{Trig} \geq N\tau_{kHz} = 100$ ms is the changing, external 10-Hz trigger period. With the repetition rate (build-up time) disrupted only on every N-th cycle, the modeling suggests that only the following $n = 1$ cycle has its pulse energy disturbed greater than a fraction of a percent.

Characterization of how the single-cycle triggering impacts laser performance was done empirically. To control the disruption, two signal generators are used. The first is used as the variable 10-Hz or slower ($\tau_{Trig} \geq 100$ ms) event while the second acts as the burst generator firing $N = 100$ pulses with a fixed $\tau_{kHz} = 999.1$ µs spacing externally triggered by the slow generator.

A fast, 1-ns photodiode is connected to a 2-GHz oscilloscope monitoring the *Empower* output and triggered on the 10-Hz event. In this way we observe the output of the first pulse after the discontinuity in timing as well as its nearest neighbors with a 4-ms sample taken at each shot monitoring the $n = 99, 100, 1$ and 2 pulses of each macropulse train. With a zoomed trace on each of the four pulses, their amplitude and area can be averaged over several shots to record the peak and total pulse energy of each for a given τ_{Trig} and the associated disrupted τ_N, as illustrated in Fig. 5.2.

We expect the output to be steady as it approaches $n = 100$ and to quickly recover after the disrupted $n = 1$ pulse. The $n = 100, 1$ and 2 pulses energies E_n are normalized to the energy E_{99} of the 99-th pulse in each train to monitor relative changes to the steady state output. This data is shown in Fig. 5.3 as a function of the disrupted period τ_{100} from varying τ_{Trig} (Eq. 5.1). To extrapolate to values outside the range measured, a trend line based on cavity parameters roughly estimated using the measured pulse shape on a fast photodiode [84] combined with a fit to this data using the numerical models in [83] is shown.

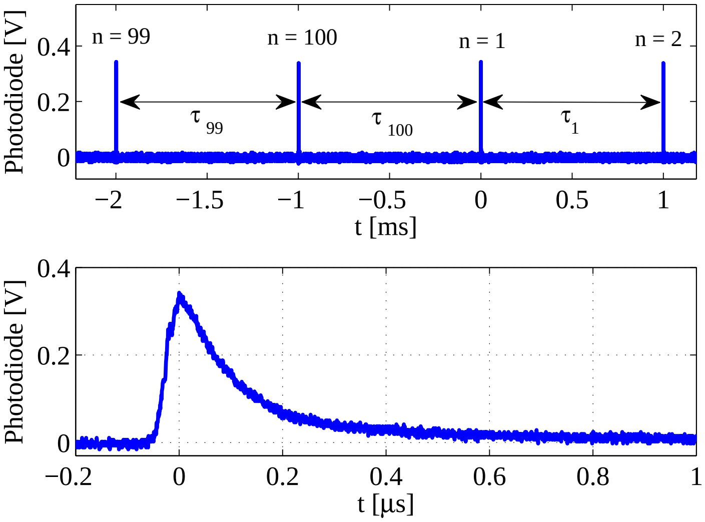

Figure 5.2: Example sweep measuring regen pump laser intensity dependence on the timing disruption introduced by 1-kHz, 100 pulse burst generator being triggered by a >10 Hz event (top). On each sweep, the amplitude and area of the zoomed traces (bottom) of each of the $n = 99, 100, 1$ and 2 pulses in the macropulse are recorded.

We note that the statistical error bars shown in Fig. 5.3 are found to be driven primarily by digital sampling error from the use of the lower time resolution zoomed traces and not indicative of actual energy fluctuations. As evidence of this, contracting the sampling region to cover only one pulse reduced this error to less than 1%.

Fig. 5.3 clearly demonstrates the expected behavior with the energy of the first pulse E_1 deviating from the steady-state output at a rate of 0.023% per µs change in τ_{100}. As the 10-Hz photoinjector trigger (Fig. 5.1) demands operating with as much as 240 µs variation in τ_{Trig}, E_1 can be expected to vary as much as 3–8% from nominal.

As expected, however, the output quickly recovers by the second $n = 2$ pulse. Within error bars there are no observable deviations in output with the fitted model suggesting relative fluctuations are limited to $< 2 \times 10^{-4}\%$ over the range shown.

To verify that this *Empower* behavior translates to an observable effect on the regen amplifier's output, the same measurement was carried out for the *Spitfire* with data shown in Fig. 5.4. As the integrated output of the 1-ns photodiode is still being used to estimate pulse energy for the 100-fs amplified pulses, sampling error becomes much larger and the linearity of the diode response is questionable and not estimated here.

In spite of this, the larger pump energies for the $n = 1$ pulse are resolved as larger amplified pulses, though changes in E_2 are not observed within measurement limits.

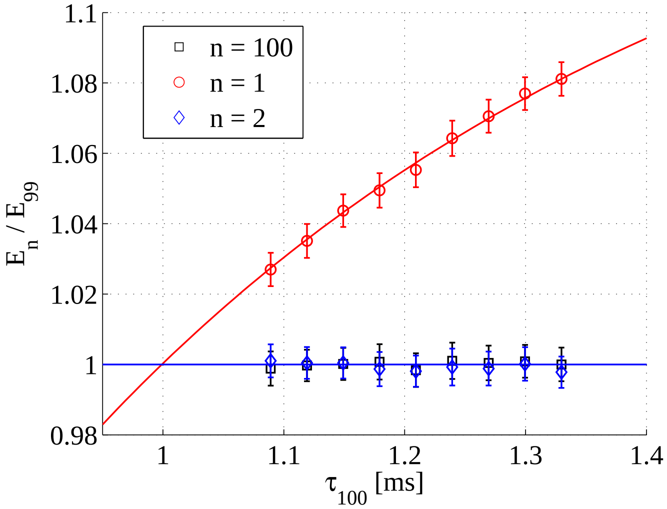

Figure 5.3: Relative deviation of n-th *Empower* pulse energies within the 100-pulse train as a function of τ_{100} from using the burst generator setup. For all other $n \neq 100$ in the train, $\tau_n = 999.1$ μs (see Fig. 5.2).

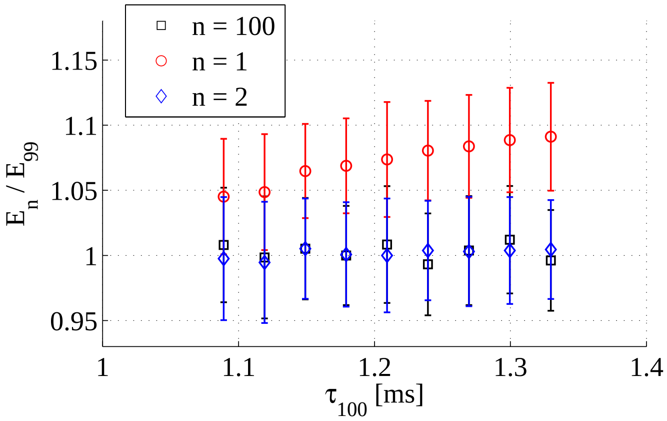

Figure 5.4: Measured relative deviation of n-th *Spitfire* pulse energies within the 100-pulse train as a function of τ_{100} from using the burst generator setup.

From these we see that the first pulse in every burst will see unwanted fluctuations while the second appears acceptably stable. Therefore for both the EOSD probe pulse and UV drive laser pulse generation, a delayed 1-ms duration, 1-Hz gating signal is sent to the TDG to select only the second pulse. With the 1-kHz signal generator delayed 0.5 ms from the 10-Hz signal and the gate delayed 1.5 ms, the second, more stable laser pulse is selected to be synchronous with the 1-Hz photoinjector clock for use with accelerator experiments. Choosing a still-later pulse in the train may be generally preferred, however the 1-Hz master event for the photoinjector is delayed less than 2 ms from the 10-Hz signal, not allowing sufficient time to choose anything later than the second.

5.1.3 1-kHz trigger synthesizer

Using the above trigger generator configuration has been demonstrated to provide reasonable triggering for the regen laser system. As a final solution, the FPGA-based active trigger synthesizer was also developed to further improve reliability. Based on several built-in counters, it includes three primary improvements.

First, unlike an ordinary burst generator, the FPGA is ready to fire the next burst up to one half of a micropulse period before (or after) the end of the previous 100-cycle macropulse. In this way the firing frequencies need not be chosen with an arbitrary offset of the last micropulse duration so that the mean value of τ_N is equal to $\tau_{n \neq N}$.

Second, if the 10-Hz trigger does not fire within this $\pm 1/2$-cycle window, the synthesizer resumes continuous firing of its 1 ms-spaced pulse train while it waits for the next reset. While this may result in a laser pulse not firing in sync with the 1-Hz of the accelerator on a given shot, it ensures that the *Empower* firing rate stays within its specified 500 Hz – 5 kHz range to prevent any under- or over-frequency protection faults from forcing shut down of the laser, regardless of the state of the 10-Hz signal which can suffer occasional disruptions.

Finally, it was observed that τ_{Trig} has a 30 µs RMS jitter with a slow drift of several tens of microseconds. Adaptive feedback was therefore also included to reduce the maximum observed τ_{100} to the level of jitter in τ_{Trig} and ensure that subsequent shots regularly arrive within the 1-ms allowed window. To this end, the synthesizer counts out the difference between the nominal $\tau_{Trig,0} = 100$ ms and the actual time elapsed between successive slow trigger events. For the next burst, this difference is absorbed into a small, fixed change ϵ_τ in the micropulse period $\tau_{\mu P} = 1$ ms over a variable number of cycles in the burst to make the macropulse approximately equal in duration to the previous 100-Hz period.

Explicitly, the adjusted micropulse period $\tau'_{\mu P}$ is

$$\tau'_{\mu P} = \begin{cases} \tau_{\mu P} + \epsilon_\tau & \text{for } \tau_{Trig,prev} \geq \tau_{Trig,0} \\ \tau_{\mu P} - \epsilon_\tau & \text{for } \tau_{Trig,prev} < \tau_{Trig,0} \end{cases} \tag{5.2}$$

A dependence of the pump laser output on changes to the firing rate was demonstrated in the previous section. We have chosen ϵ_τ to be 5 µs, just 0.5% of the regular firing rate, to keep the effect introduced by the adaptive period negligible. The number of cycles N_{cor} the adjusted cycle is used is to correct the macropulse length is then,

$$N_{corr} = \text{int}\left(\frac{\left|\tau_{Trig,prev} - \tau_{Trig,0}\right|}{\epsilon_\tau} \right) \tag{5.3}$$

where int(x) is the nearest-integer rounding function. The synthesizer will switch its repetition rate from $\tau_{\mu P}$ to $\tau'_{\mu P}$ for N_{corr} cycles so that the effective macropulse τ_{MP} length of the next burst will be

$$\tau_{MP} = (N - N_{corr})\,\tau_{\mu P} + N_{corr}\tau'_{\mu P} \tag{5.4}$$

As our application makes use of only the first or second cycle of any macropulse, the adapted period $\tau'_{\mu P}$ isn't applied until later in the burst, running from cycles $n = 20$ to $n = 20 + N_{corr}$ to avoid any complication with the first few shots of interest.

We expect that the difference between the arrival of the next reset trigger from the 10-Hz signal will therefore regularly occur within $\epsilon_\tau \pm \langle \Delta\tau^2_{Trig} \rangle^{1/2} \approx 35$µs. A measurement comparing output from the custom FPGA synthesizer to a burst generator appears in Fig. 5.5 with both being triggered by the A0PI 10-Hz clock. The FPGA reliably matches the end of one burst with the start of the next and without needing the large offset of the burst generator. From Fig. 5.5 we also see that the drift correlated to that of the slow trigger is effectively removed, reducing the maximum observed fluctuations.

Statistics accumulated over a 24-hour period show the FPGA output having a spread in the final period of just 15 µs RMS, an improvement over the 30 µs from the burst generator. The maximum deviation of the period preceding the first shot in each macropulse τ_{100} is ±40 µs for the FPGA over the same 24-hour period, in agreement with expectation and a good improvement over the ±120 µs from the burst generator.

Using the FPGA synthesizer, the IR pulse energy standard deviation for the first pulse of each burst is found to be 3.2% with no measurable intensity drift correlated to 10-Hz triggering drift. This corresponds to a spread of 10.1% for the UV output. Using the more stable $n = 2$ pulse, this is reduced to 1.5% in the IR and 4.0% in the UV.

We find that with the adaptive correction, burst triggering dependably occurs on-time with each cycle. With the FPGA synthesizer and second-cycle pulse selection, reliable operation of the amplifier is realized with no observed amplifier timing faults, missed shots, or reducible intensity fluctuations.

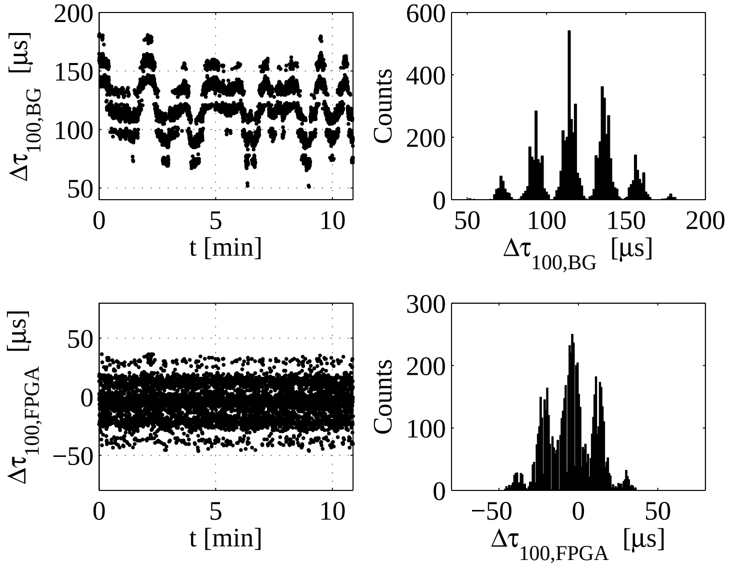

Figure 5.5: Comparison of signals generated using a 1-kHz burst generator (top) and the FPGA synthesizer (bottom) showing the difference of the period of the final shot in the burst from the nominal micropulse period $\Delta\tau_{100}$ over time (left) and associated histograms (right).

5.2 Fine synchronization

We now turn to the fine synchronization of both the added Ti:sapph system and existing Nd:YLF drive laser to the photoinjector RF. Fine phase locking for both starts with the 16th sub-harmonic being counted down from the 1.3-GHz master oscillator and fed to the built-in locking electronics of the respective seed laser (Fig. 5.1). These internal phase mixers compare the phase of the incoming 81.25-MHz signal with that of a photodiode mounted in the oscillator cavity. The resulting difference voltage is used to drive a piezo-mounted intracavity mirror to maintain the phase lock.

The manufacturer specification for the *Tsunami* oscillator's temporal jitter is 500 fs RMS. To verify this a 20-GHz fast photodiode (Hamamatsu G4176-03 photodiode with Picosecond Pulse Labs 5545-107 bias tee) was used. The signal after a custom 1.3-GHz bandpass, Q = 1000 cavity filter (Microwave Filter Co., Inc., 5MNSP-1.3/1.3) was measured using a signal source analyzer (Agilent E502B) consistently yielding an RMS jitter of better than 300 fs. Similar measurements of the Nd:YLF system also yield a typical jitter of 300 fs RMS.

These are in good agreement with specification and with the less than 200-fs RMS jitter measured with the signal source analyzer from the 1.3-GHz master oscillator directly.

5.2.1 Initial phase measurements

To verify long-term stability we begin with measurements using the synchronized streak camera. The laser at the photocathode surface is imaged onto the entrance slit of the streak camera. The time of arrival is inferred from a fit of the digitized streak image.

Details on the resolution of the streak camera were given at the end of Sec. 2.1. However, as the PLL that maintains the streak camera's lock to the 81.25-MHz reference may also suffer from its own drift, a second technique was initially employed to verify the measured time of arrival using the launch phase sensitivity of the total charge emitted from the gun [85, 86].

This "charge technique" is based on operating the RF gun at a low phase with respect to the photocathode drive laser. In this regime, the emitted charge strongly depends on the phase between the laser and gun thereby providing a means to measure the jitter between the two systems.

Consider that some minimum gradient is needed to accelerate photoelectrons excited by the laser pulse to overcome the potential from their image charge at the photocathode. Where the gun RF phase is set such that the sinusoidal gradient provided is lower than this critical value over the duration of the laser pulse, no charge is emitted. As the phase of the RF is advanced, the gradient will increase until it exceeds this value and begins to accelerate the photoelectrons emitted by the head of the laser pulse. Continuing to increase the phase will capture still more of the emitted electrons until the gradient is sufficiently high across the entire pulse and the full charge available by photoemission is accelerated. The total charge emitted can then be related to a partial integration of the laser's temporal profile in this regime [85].

We therefore assume an error-function dependence on the charge emitted as a function of gun phase for the purposes of producing a map of charge to phase. An example of such a phase scan and corresponding fit are shown in Fig. 5.6 with the charge emitted normalized to the shot-to-shot laser intensity.

The phase sensitivity will be highest at the center of the rising edge. For the phase scan shown in Fig. 5.6, the maximum slope of the unnormalized scan is 49.4 pC/degree with a maximum charge of 500 pC.

In our case the charge is monitored by an integrating current transformer (ICT) downstream of the gun. As noise in the ICT maps to a typical effective time resolution of 1.1 ps RMS (~0.5°), this measurement is only sufficient for monitoring drifts of several picoseconds.

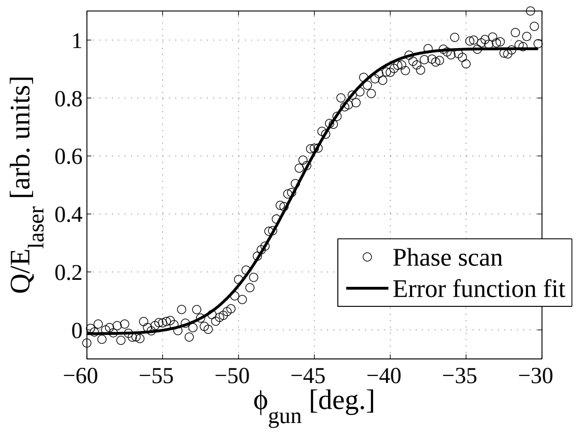

Figure 5.6: Scan of emitted charge normalized by laser pulse energy (Q/E_{laser}) versus RF gun phase scan showing error function dependence on launch phase. For this scan, setting a fixed $\phi_{gun} = -47°$ yields a measurable change in charge for phase fluctuations over a range of a few degrees.

Several measurements were performed simultaneously recording data using both methods for each laser with example results shown in Fig. 5.7. For both of these sets of plots, the respective laser had a full day of warm up prior to data taking. Gaps seen in the data for the Ti:sapph system were later found to be caused by improper setup of the 1-kHz *Dazzler* triggering and have since been corrected.

Shot-to-shot fluctuations for all measurements are found to be dominated by the corresponding measurement noise. For a direct comparison of observed drifts, the moving average of each of the plots is taken to filter out the high frequency jitter. 2D histogram scatter plots of these drifts are shown in Plots (e, f) of Fig. 5.7.

A weak one-to-one correlation is seen in the data taken for the Nd:YLF system. For the Ti:sapph, both methods see a similar drift on the scale of a few picoseconds per hour, however this appears exaggerated by the streak camera. This is likely owing to the streak camera synchroscan unit contributing its own synchronization drift. In any case, real drifts beyond the stated requirements are observed.

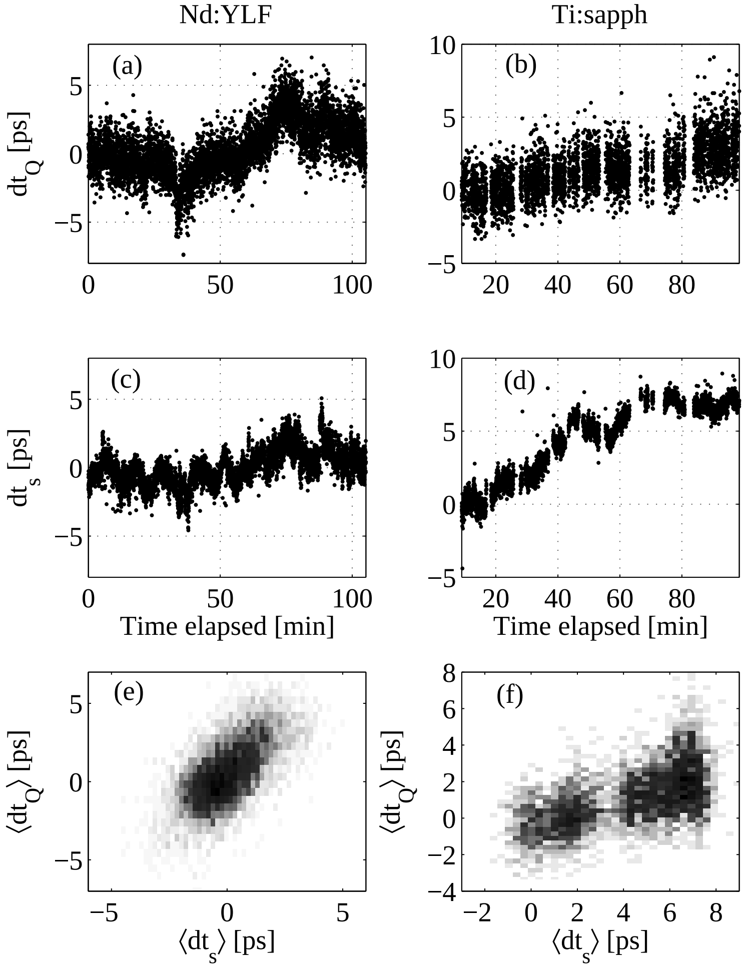

Figure 5.7: Temporal drift data collected with the two techniques for the Nd:YLF (a, c, e) and Ti:sapph (b, d, f) lasers. The phase difference *dt* is measured simultaneously using the charge method (a, b) and streak camera (c, d) when the respective laser is used to drive the photoinjector. For comparison of the drift seen by the two methods, 2D histogram scatter plots of the moving average $\langle dt \rangle$ for each pair of data sets are shown below (e, f).

5.2.2 Simultaneous streaking of two images

As an alternative to eliminate the ambiguity as regards the streak camera synchronization, simultaneous streaking of two light sources was also performed. This is particularly useful in comparing the timing of the optical output from the two lasers. By simultaneously diagnosing the two optical pulses with the same streak camera sweep, the relative phase difference can be measured from shot-to-shot by subtraction thereby eliminating the drift of the images on the screen from the streak camera sweep unit.

To verify this, Fig. 5.8 shows streak data for the Ti:sapph seed laser with OTR from X09 (Fig. 2.1). Here the frequency-tripled output of the *Spitfire* is used as drive laser to produce 1.5 nC, 16 MeV bunches.

The synchronization of the 81.25-MHz seed train with the 1-Hz OTR pulse from X09 at the streak camera is achieved using a double-folded retroreflector providing a variable 12 ns optical path delay of the laser. This is combined with the optical path of the OTR with the delay adjusted to bring both streak images in to view on the same RF sweep. The time-axis projection of the streak image is recorded shot-to-shot for fitting to determine the temporal centroid of each pulse.

For this measurement, the longer streaks produced in range 1 diluted the photon density of the weak, single-pulse OTR at the streak camera's screen. To provide a signal measurable over background, sweep range 2 was therefore used instead. The mean streak widths taken from the Gaussian fits to the OTR and IR data in Fig. 5.8 were 5.22±1.63 ps and 2.98±0.28 ps RMS, respectively. The deviation in the shot-to-shot phase difference were 2.08 ps and 1.09 ps, respectively. The larger jitter seen for the OTR track are attributed to larger measurement and fitting noise for the weak OTR signal.

For the nominal operating phase of the RF gun, we expect the gun will not significantly affect the single-particle longitudinal dynamics that would result in drifts from the photocathode laser being mapped onto drifts of the electron bunch time of arrival. We therefore expect the drifts of the OTR and laser signals to be identical and comprised of the sum of the laser and streak camera synchroscan drifts.

Again applying a high-frequency filter to deduce the drift $\langle t \rangle$, inset (b) of Fig. 5.8 includes the difference in drift over time showing effectively zero phase difference within a 0.63 ps RMS spread. Further, inset (c) shows the scatter plot of the filtered drifts and line of best fit with a slope of 0.99, as expected. Though we cannot decouple the streak camera from laser drift contributions with this information, it reasonably verifies that relative phase measurements can be accomplished with this dual imaging approach with contributions from streak camera PLL drift removed.

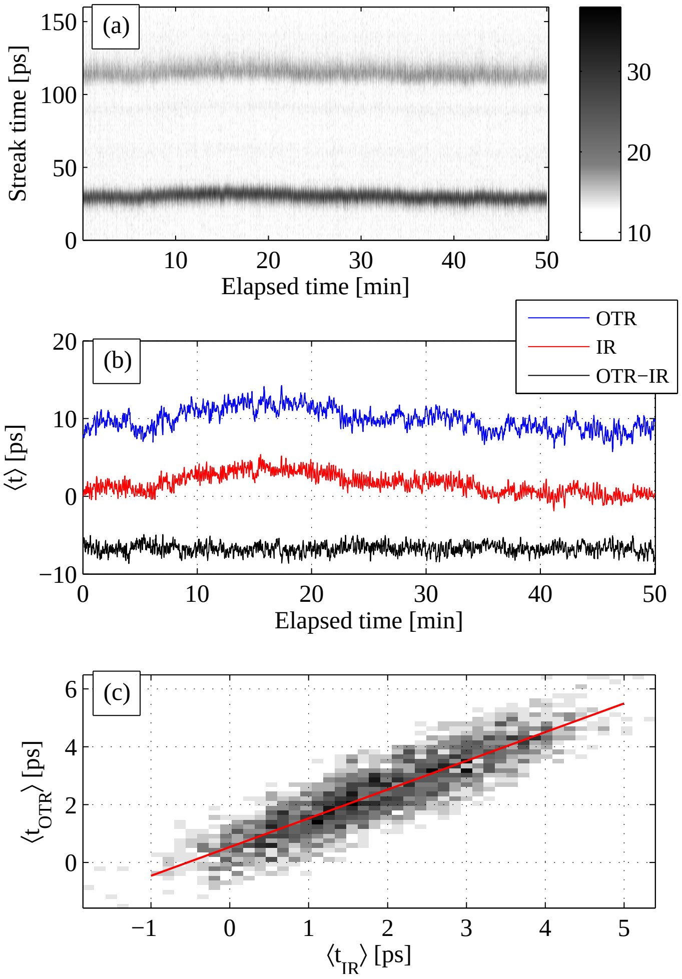

Figure 5.8: Streak camera data (sweep range 2) for simultaneous imaging of the Ti:sapph seed laser IR and OTR from the beam using the Ti:sapph system as drive laser. (a) Raw time-axis projections from the streak camera for the OTR (top) and laser IR (bottom). (b) Drifts $\langle t \rangle$ deduced from the centroid of double Gaussian fitting after high frequency filtering (arbitrary vertical offsets). (c) 2D histogram scatter plot of the drifts with inset line of best fit. Slope of fit line = 0.99.

As relates to phase-locking between lasers for EOSD, we repeat this experiment using the Ti:sapph IR and OTR from the Nd:YLF-driven electron beam. Several sweeps of the streak camera can then be stacked to produce a stronger signal allowing for fast, range 1 measurements assuming negligible phase drift between the 1 MHz-spaced bunches. Results are shown in Fig. 5.9 using 80, 500-pC bunches with the streak camera operating in its fastest, range 1 sweep mode. The 2-min gap in the data for the OTR at 12 min was due to temporary loss of gun RF.

For this set, the streak widths for the IR and OTR were 1.11±0.05 ps and 4.12±.16 ps RMS, respectively. Shot-to-shot jitter was 160 fs and 434 fs, respectively, with the larger value for the OTR signal attributed to the longer streak length leading to a greater inherent measurement uncertainty.

We note in Fig. 5.9 an 8.5 ps/hour relative drift between the two signals manifesting primarily in the OTR signal as well as a 5.5 ps phase jump at 32 min. This has been identified as a signature of the Nd:YLF seed laser's phase lock loop. A frequency difference between the seed cavity's 81.25 MHz and reference to the master oscillator is erroneously fed back into the cavity with the piezo experiencing a relatively constant displacement drift until reaching its limit of travel. At this point the electronics adjust the picomotor stage upon which the piezo mirror is mounted to reset its position to the center of the piezo travel. This movement of the stage causes the phase jump in the seed output.

The periodicity of these resets and the slope of the drift between them have been found to be highly sensitive to the alignment, optical power and warm up of the Nd:YLF oscillator making consistent correction by laser tune up alone difficult.

We observe that the spread from drift contributions in these data sets account for the significant, ps-scale portion of timing instability with drifts exceeding 5 ps/hour observed in the Nd:YLF system.

5.2.3 Secondary laser phase monitor and feedback

To correct the ps-scale drift of the seed lasers while also providing an additional measure of laser phase stability with respect to the RF, we use a setup similar to that demonstrated in [87, 88], shown in Fig. 5.10. For phase detection, optical leakage is sent to a fast photodiode. The resulting signal then passes a 1.3 GHz band-pass cavity filter and low-noise amplifier. The phase is compared to that of the 1.3-GHz master oscillator in a phase mixer with input RF levels attenuated to the operational range of the mixer and a variable phase delay on the diode signal so the phase difference can be set to operate in the mixer's linear response region.

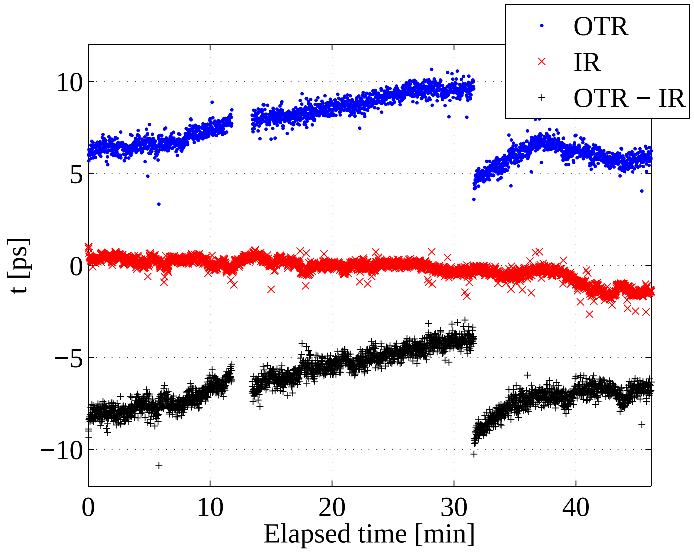

Figure 5.9: Relative time of arrival data from simultaneous (sweep range 1) streaking of the Ti:sapph IR and OTR generated by beam produced using the Nd:YLF system as drive laser (arbitrary vertical offsets).

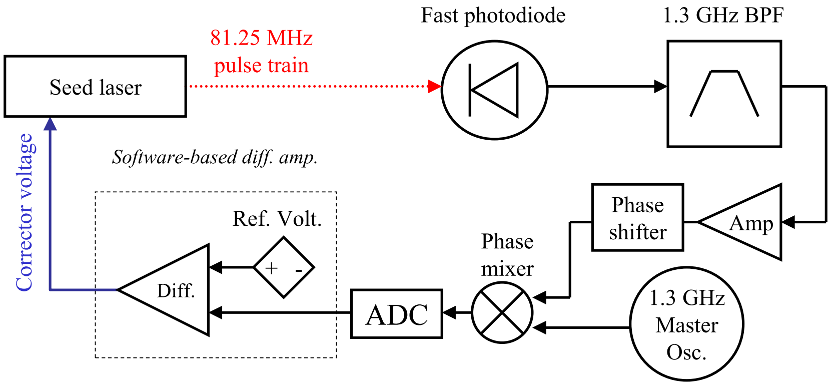

Seed laser
81.25 MHz pulse train
Fast photodiode
1.3 GHz BPF
Corrector voltage
Software-based diff. amp.
Ref. Volt.
+ -
Diff.
ADC
Phase mixer
Phase shifter
Amp
1.3 GHz Master Osc.

Figure 5.10: Block diagram of the laser phase monitor and software-based feedback used to compensate drift in both seed lasers.

Mixer output can be used to monitor the phase difference between the laser and master with a conversion factor of 100 mV/deg. A 4-ms sample is converted by an analog-to-digital converter (ADC) once per second with a sampling rate of 1 MHz. The spread of the sample is recorded to monitor jitter and has resolved noise as low as 200 fs RMS while the mean voltage of each sample is tracked for phase drift.

The synchronization electronics of both systems include input ports to which an external bias can be applied that's added into the signal driving the piezo-mounted mirrors. This is employed in feedback mode using software-based differential amplification of the ADC output. The mean of the sample is compared to a set reference voltage and, with the appropriate programmable gain, generates a corrector voltage sent back to the associated seed laser via an internet rack monitor (IRM) [89] signal.

The digital IRM channels used to provide the programmable corrector voltage have a minimum step size of 5 mV. For the Ti:sapph system, this was found to be too large to provide adequate time resolution given the feedback sensitivity of the electronics. To correct this, a 1/9 analog voltage divider is added to the phase input port of the *Tsunami* to reduce the effective minimum step size of the IRM output to acceptable levels with changes to the effective differential amplifier gain accounted for.

5.2.4 Measurement of corrected laser-to-laser drift

Feedback loop performance for phase stability between the two lasers was verified by again analyzing simultaneous streak imaging of the Nd:YLF UV and amplified Ti:sapph IR outputs. Results for phases tracked by the phase detector in the feedback loop versus that on the streak camera are compared in Fig. 5.11. The phase as recorded by the streak camera and loops are plotted with the concurrent secondary feedback being applied with feedback disabled at 100 min.

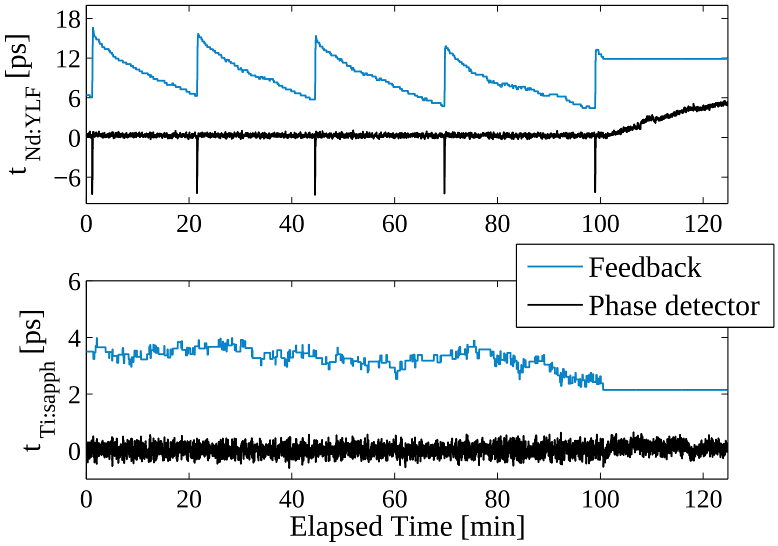

Figure 5.11: Time of arrival data taken simultaneously for the Nd:YLF (top) and Ti:sapph (bottom) laser systems. The feedback corrector signals (blue) are generated in response to the RF phase detectors (black) with feedback disabled at 100 min.

Prior to this measurement, the Ti:sapph system was warmed up over a full day while in use for other experiments. As such, the corrector phase being generated for the Ti:sapph laser is relatively stable to the order of the laser jitter. In fact, the spread of the long-term projection seen on the phase detector is the same (< 200 fs, RMS) whether or not feedback is enabled in this set.

The relatively stable output is nonetheless shown here for comparison to the Ti:sapph output as measured on the streak camera, shown in Fig. 5.12. We observe that the streak camera data shows an abrupt change in the Ti:sapph streak image at 106 minutes that does not appear on the phase monitor which is also the case for the Nd:YLF measurements. This indicates a disruption in the PLL for the streak camera which is indeed removed after taking the difference in the output phases from the streak camera measurement (Fig. 5.12).

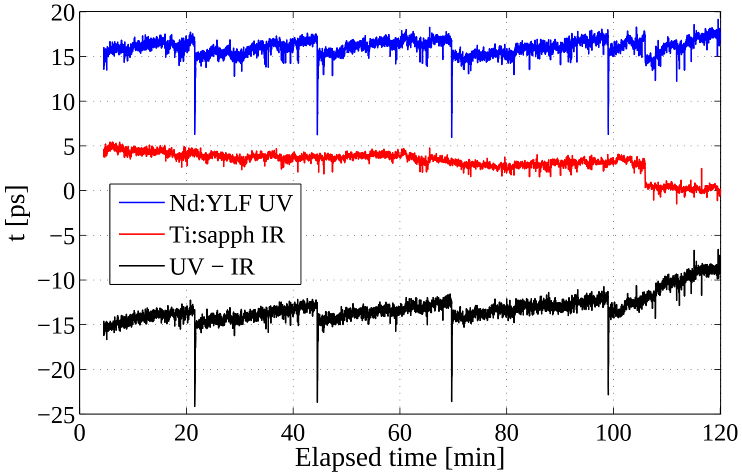

Figure 5.12: Time of arrival t determined from simultaneous streak camera imaging for Ti:sapph (red) and Nd:YLF (blue) lasers and the deduced time difference (black). Both lasers are imaged to the slit of the synchronized streak camera in the accelerator tunnel. Data taken concurrently with that shown in Fig. 5.11 with feedback enabled from 0–100 min.

In the data for the Nd:YLF system (Fig. 5.11), the clear sawtooth pattern as described earlier is observed in the feedback signal. The system tracks several steep drifts with phase jumps of 9.4 ps spaced roughly every 30 min with the periodicity growing a few minutes per cycle. The corresponding output phase as measured by the phase detector appears flat with the spread again on the order of the laser jitter, excepting the few cycles it takes to recover the phase lock after a jump.

The magnitude of these changes are also observable on the streak camera (Fig. 5.12) over the few cycles it takes the feedback to recover the phase. However, the streak camera reveals that the secondary phase lock loop is not fully correcting the drift with the discrete phase jumps instead appearing with a magnitude of 11.2 ps. As a result, a 1.8 ps-amplitude sawtooth drift survives in the difference signal where the few-cycle disruption from the discrete changes are neglected.

With secondary feedback disabled at 100 min, the relative phase immediately begins to run beyond this 1.8 ps drift oscillation. With feedback, however, and excluding extreme outliers from the Nd:YLF laser phase jumps, the spread of all points taken with loops enabled is 0.81 ps RMS. This brings us within the desired sub-ps specification for long-term timing stability.

In this section we have demonstrated how our commercial titanium-sapphire laser and transport optics were installed and successfully commissioned at the A0 photoinjector laboratory at Fermilab. The system is reliably synchronized to the 1-Hz RF pulse generation and instrumentation trigger with the seed laser exhibiting temporal jitter of less than 300 fs RMS.

Long-term phase stability of both the existing Nd:YLF drive laser and new Ti:sapph system has been diagnosed by a number of independent experiments to allow diagnosis of the Nd:YLF-driven beam by EOSD using the Ti:sapph as probe laser. Simultaneous long-term synchronization of the seeds to within 1 ps of the 1.3-GHz master clock is accomplished using independent secondary feedback loops available for both systems. Intensity stability of amplified IR output is found to be 1.5% RMS with a corresponding UV pulse stability of 4%. With the system installed, we now consider the diagnosis of the time-frequency domain of the laser pulse.

5.3 Temporal pulse shape measurement

Unambiguous laser chirp information is of great use for our ultra-fast applications. For EOSD it gives the information required to map wavelength to time for decoding the signal sampled from the electron beam. For the blow-out experiment, it's to verify the laser pulse is as near bandwidth-limited as possible to generate the shortest UV pulse after tripling. Information about the spectral phase can be fed back into the *Dazzler* by subtraction to correct third order dispersion generated in the regen for more efficient tripling and a more uniform UV pulse.

Therefore, to verify the temporal pulse shape of the output laser pulse for a given experiment, frequency-resolved optical gating using second harmonic generation (SHG FROG) was used for complete laser phase reconstruction [90–92].

5.3.1 SHG FROG

Like EOSD, SHG FROG utilizes the second order polarization in an electro-optically active medium. SHG FROG is accomplished by analyzing the spectrum of the light generated from the mixing of the laser crossed with its time-delayed replica in a frequency-doubling crystal. By measuring the resulting spectrum over a range of delays, a two-dimensional interferogram is generated that can be used to deduce the amplitude and phase of a laser pulse.

In this sense SHG FROG is a form of self-referenced spectral interferometry. Other variations have since been developed such as temporal analysis by dispersing a pair of light E-fields (TADPOLE), cross-correlation FROG (XFROG), and spectral interferometry for direct E-field reconstruction (SPIDER) (c.f. [93–96]). All are based on the generation of an interferogram that is subsequently analyzed to reconstruct the amplitude and phase of the laser pulse.

Apparent signal ambiguities and level of difficulty in the interpretation and reconstruction of the interferograms varies from technique to technique, as does the complexity of the experimental set up needed to generate the traces. Still the FROG approach is appealing for its relative simplicity. Some ambiguities exist for SHG FROG in particular [90, 92, 97], but these are of minor consequence for our purposes.

Also like EOSD, FROG is used for ultra-short laser pulse diagnostics due to the relatively fast ($\ll 1$ ps) effective optical switching time of the nonlinear interaction of optical pulses in materials. Other variations of FROG exist with several studied and summarized neatly by Trebino, *et al* [90, 92, 98]. The principle is the same for the scanning delay FROG methods, varying primarily in the optical nonlinearity used with most depending on third-order polarization effects with each of yielding a different form of interferogram. SHG FROG was chosen for the measurement of the Ti:sapph pulse as it depends on the much stronger second-order polarization in a doubling crystal, making it particularly robust and straightforward to set up. Details on SHG FROG in particular were also summarized in [97].

Though referred to as a second harmonic effect, SHG FROG is based on the two-beam sum frequency term in the expansion given by Eq. (4.12c). As the spectra of the pulse and its replica are both primarily at the frequency ω_0 corresponding to the laser's center wavelength $\lambda_0 = 800$ nm, we see that the induced SFG second order polarization of Eq. (4.12c) from the two-beam mixing will generate a spectrum around an optical carrier frequency $\omega_{0,sfg} = \omega_0 + \omega_0 = 2\omega_0$, effectively a second harmonic beam.

As with EOSD, the doubling crystal's dispersive properties can generate measurement artifacts. However we will see that in a (uniaxial) doubling crystal some linearization of these effects is possible at the all-optical wavelengths allowing clearer optimization of the interaction.

5.3.1.1 SHG FROG optical system

To achieve the mixing, the laser pulse must first be split to generate a replica. This is shown in Fig. 5.13 for our optical layout, built on the FROG kit from Newport Corp. (part no. FRG-KT) [99]. After splitting, the transmitted pulse traverses a hollow roof mirror to provide a small vertical displacement. The beam reflected by the splitter is sent to a mirror at normal incidence, mounted on a moveable stage to allow a variable time delay τ. The two beams are then recombined by the splitter with vertically offset, parallel paths. These are sent to a spherical mirror that focuses the beams to the same focal point in a thin doubling crystal. For doubling over the Ti:sapph spectrum, a 200-µm thick β-barium borate (BBO) crystal is used.

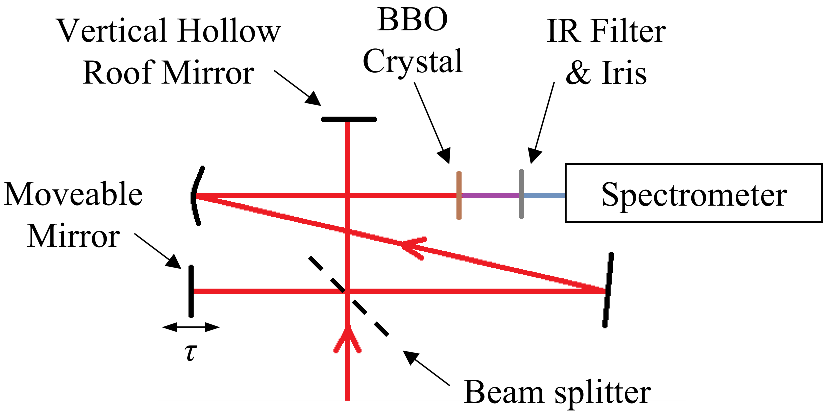

Figure 5.13: Optical layout of the SHG FROG. The laser pulse is split to generate a spatial offset in one beam and time delay in the other. These are then focused onto a BBO doubling crystal with the central, sum-frequency beam sent to a spectrometer for measurement. Detail of the two-beam crossing at the crystal is shown in Fig. 5.14.

The crossing at the crystal is illustrated in Fig. 5.14 including the direction of the incident and generated beams, their polarizations, and the optic axis $\hat{c}$ of the BBO crystal cut at an angle θ to the surface normal of the crystal. Because the crystal is chosen for efficient doubling, additional SHG beams are generated as well, corresponding to the terms given by Eq. (4.12b) from each beam interacting with itself.

The spatial separation of the various second harmonic beams shown in Fig. 5.14 is a result of conservation of momentum for the effective $\gamma + \gamma \to \gamma$ interaction occurring via scattering in the BBO. We label

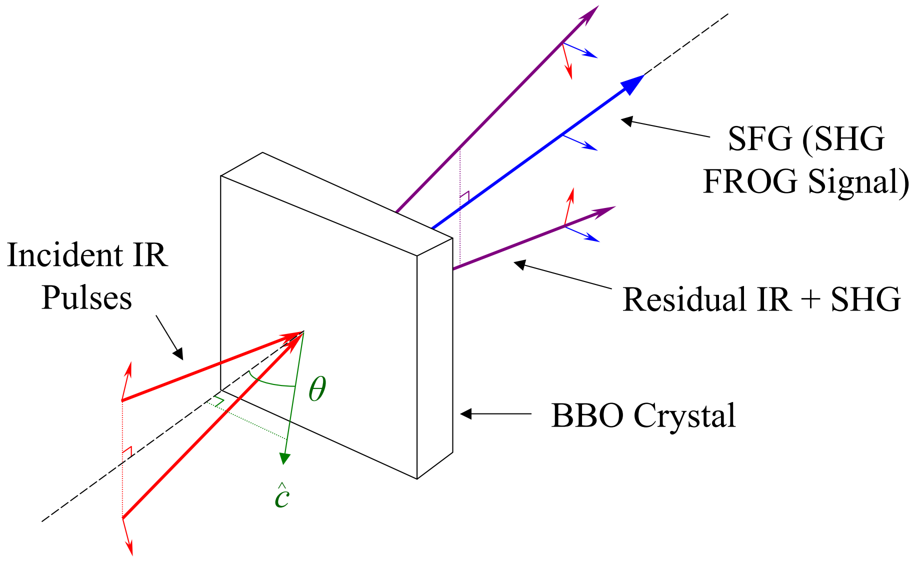

Figure 5.14: Geometry of the crossing of the optical pulse and its delayed replica at the BBO crystal for SHG FROG showing the orientation of the crystal optic axis $\hat{c}$ as well as the propagation and polarization directions for the incident and generated beams. The spectrum of the SFG light varies as a function of the delay τ, generating the FROG trace.

the wavevectors of the two incident beams $\vec{k}_1$ and $\vec{k}_2$. Assume for the moment the index of refraction is well-matched at all wavelengths so that $n(\omega_0) = n(2\omega_0)$. In this case, $k(2\omega_0) = 2k(\omega_0)$. For SHG, a parent beam interacts with itself yielding the subsequent doubled wavevector

$$\vec{k}_{11}(2\omega_0) = \vec{k}_1(\omega_0) + \vec{k}_1(\omega_0) \tag{5.5}$$

$$k(2\omega_0)\hat{k}_{11} = 2k(\omega_0)\hat{k}_1 \tag{5.6}$$

$$2k(\omega_0)\hat{k}_{11} = 2k(\omega_0)\hat{k}_1 \tag{5.7}$$

$$\hat{k}_{11} = \hat{k}_1, \tag{5.8}$$

and likewise for beam 2. These SHG beams are collinear with their respective parents. When the two beams interact instead with each other we have

$$\vec{k}_{12}(2\omega_0) = \vec{k}_1(\omega_0) + \vec{k}_2(\omega_0) \tag{5.9}$$

$$k(2\omega_0)\hat{k}_{12} = k(\omega_0)(\hat{k}_1 + \hat{k}_2) \tag{5.10}$$

$$2k(\omega_0)\hat{k}_{12} = k(\omega_0)(\hat{k}_1 + \hat{k}_2) \tag{5.11}$$

$$\hat{k}_{12} = \frac{1}{2}(\hat{k}_1 + \hat{k}_2). \tag{5.12}$$

The direction of the SFG ray $\vec{k}_{12}$ is therefore the bisector of the two parent rays.

The non-collinear geometry is useful then to spatially separate the SHG beams from the crossed SFG light by use of an iris, shown after the crystal in Fig. 5.13. Finally, though most of the remnant IR light is also blocked by the iris and the measurement is spectrally resolved, a dichroic IR filter is also typically used to block any remnant laser scatter, reducing potential stray light in the spectrometer.

5.3.1.2 The signal and effect of phase mismatch

With the initial optics described, we now consider optimization of the bulk signal. The components of the second-order permittivity tensor for BBO couple the fundamental into orthogonally polarized SFG/SHG light [51]. The choice of the polarization and optic axis orientations are such that both IR beams are ordinary so the doubled light is then extraordinary. This configuration is referred to as Type-I SHG [51]. The choice of phase matching type and crystal cut angle θ in Fig. 5.14 are given by the dispersive properties of BBO in this frequency-doubling configuration.

Following a similar analysis as led to Eq. (4.59) but now assuming our two incident fields are the laser pulse with spectrum $\tilde{E}_1(\omega)$ and its delayed replica $\tilde{E}_2(\omega)$, the SFG spectrum produced yields the FROG signal $\tilde{E}_{FROG}$, given by [51, 90, 91]

$$\frac{d\tilde{E}_{FROG}(\omega)}{dz} \propto \int_{-\infty}^{\infty} \tilde{E}_1(\omega-\omega')\tilde{E}_2(\omega')e^{i\Delta k(\omega,\omega')z}d\omega' \tag{5.13}$$

where we have the wavevector mismatch for SFG

$$\Delta k(\omega,\omega') = k_o(\omega') + k_o(\omega-\omega') - k_e(\omega) \tag{5.14}$$

with k_o and k_e denoting wavenumbers computed using ordinary index n_o and effective extraordinary index n'_e, respectively. If we assume the undepleted pump approximation (the signal remains small compared to the laser) so that $\tilde{E}_1$ and $\tilde{E}_2$ maintain their amplitudes through the crystal, Eq.(5.13) can be integrated in z through the crystal length L to yield

$$\tilde{E}_{FROG}(\omega) \propto L\int_{-\infty}^{\infty} \tilde{E}_1(\omega-\omega')\tilde{E}_2(\omega')\left\{e^{i\Delta k(\omega,\omega')L/2}\text{sinc}\left[\Delta k(\omega,\omega')L/2\right]\right\}d\omega'. \tag{5.15}$$

Making explicit the shift τ in the time domain of the replica E_1 to generate E_2, we use the equivalent frequency-domain expression to write E_2 as

$$\tilde{E}_2(\omega) = \tilde{E}_1(\omega)e^{i\omega\tau}. \tag{5.16}$$

We also define the complex phase matching function $\tilde{\Phi}(\omega, \omega')$ as

$$\tilde{\Phi}(\omega, \omega') \equiv e^{i\Delta k(\omega,\omega')L/2}\text{sinc}\left[\Delta k(\omega, \omega')L/2\right] \tag{5.17}$$

With these and dropping the numerical subscript, (5.15) becomes

$$\tilde{E}_{FROG}(\omega, \tau) \propto L \int_{-\infty}^{\infty} \tilde{E}(\omega - \omega')\tilde{E}(\omega')\tilde{\Phi}(\omega, \omega')e^{i\omega'\tau}d\omega'. \tag{5.18}$$

From the sinc-dependence of $\tilde{\Phi}$, this signal is maximized as $\Delta k \to 0$. Indeed, where the index of refraction is perfectly matched across all wavelengths, the spectral intensity takes the form of the ideal FROG signal [90, 92]

$$I_{FROG}(\omega, \tau) \propto L^2 \left| \int \tilde{E}(\omega - \omega')\tilde{E}(\omega')e^{i\omega'\tau}d\omega' \right|^2. \tag{5.19}$$

A finite Δk in the phase mismatch function describes the slipping of the IR and blue beams away from each other in phase as they propagate through the crystal, preventing the coherent build up of the blue diagnostic ray while broadening the measured signal.

For the realistic case of finite dispersion, this is minimized to first order by ensuring that the indices of refraction at the central wavelengths are equal. Assuming the angle of incidence of the laser is small so that the three beams are approximately collinear, the phase matching condition $\Delta k = 0$ inserted into (5.14) for SFG at the carrier wavelengths becomes

$$\frac{1}{c}\left[\omega_0 n_o(\omega_0) + \omega_0 n_o(\omega_o) - 2\omega_0 n_e'(2\omega_0)\right] = 0 \quad \Rightarrow \quad n_o(\omega_0) = n_e'(2\omega_0). \tag{5.20}$$

Because BBO is uniaxially birefringent, we can modify the effective extraordinary index of refraction n'_e by cutting the crystal at an angle θ from its optic axis, as was given by Eq. (3.70). However, the axes now also correspond to different optical frequencies so that we have

$$\frac{1}{n_e'^2(2\omega_0)} = \frac{\cos^2\theta}{n_o^2(2\omega_0)} + \frac{\sin^2\theta}{n_e^2(2\omega_0)}. \tag{5.21}$$

As θ varies from 0 to 90°, n'_e will vary from n_o to n_e.

The ordinary and extraordinary indices n_o and n_e for BBO are plotted in Fig. 5.15 [100]. BBO is seen to posses negative uniaxial birefringence ($n_e < n_o$) and we note that $n_o(400\text{ nm}) > n_o(800\text{ nm})$. It is for this reason the fundamental is chosen as the ordinary ray, allowing the effective index $n'_e(400\text{ nm})$ to be shifted down toward the extraordinary index n_e to satisfy (5.21).

Adding our condition $n'_e(2\omega_0) = n_o(\omega_0)$, Eq. (5.21) is solved for θ to maximize phase matching at the carrier frequencies [51]. For BBO and an 800 nm fundamental we find $\theta \approx 29.2°$. The corresponding effective index at this angle is also shown in Fig. 5.15.

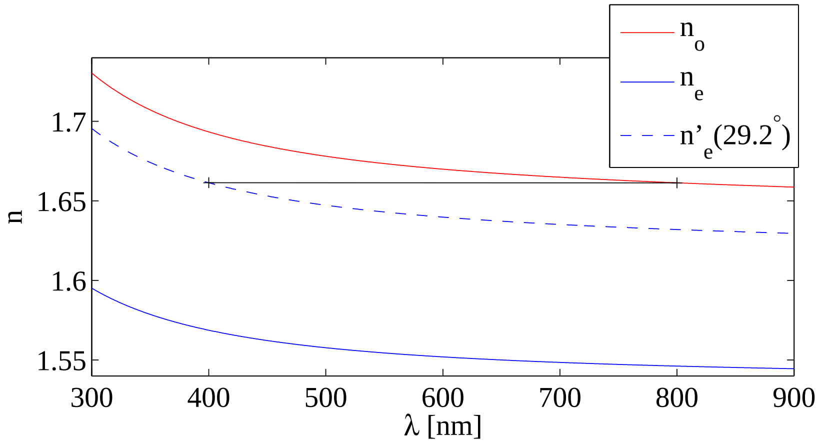

Figure 5.15: Indices of refraction n_o and n_e (solid curves) and the effective extraordinary index n'_e for a crystal cut with optic axis at $\theta = 29.2°$from the surface normal (dashed curve). For this choice of cut angle, $n'_e(400\text{ nm}) = n_o(800\text{ nm}) = 1.661$ (black line).

This cut angle ensures the center band of the doubled light is efficiently matched to the laser fundamental. With the indices now fixed, we can further inspect the impact of $\tilde{\Phi}$ which is effectively convolved into the real FROG field spectrum in Eq. (5.18).

For $\tau = 0$ (perfect overlap in the time domain) we have maximum SFG and $\tilde{\Phi}$ dictates how efficiently the various frequency components over the IR spectrum ω' map into the blue FROG spectrum ω due to the finite thickness and group velocity dispersion. From Eq. (5.17), the phase of $\tilde{\Phi}$ is given by $\Delta kL/2$ and the absolute amplitude by $|\text{sinc}(\Delta kL/2)|$. These are plotted in Fig. 5.16 for our 0.2 mm-thick, 29.2°-cut BBO over the laser spectrum. The functions are relatively constant in the IR signal wavelength λ'.

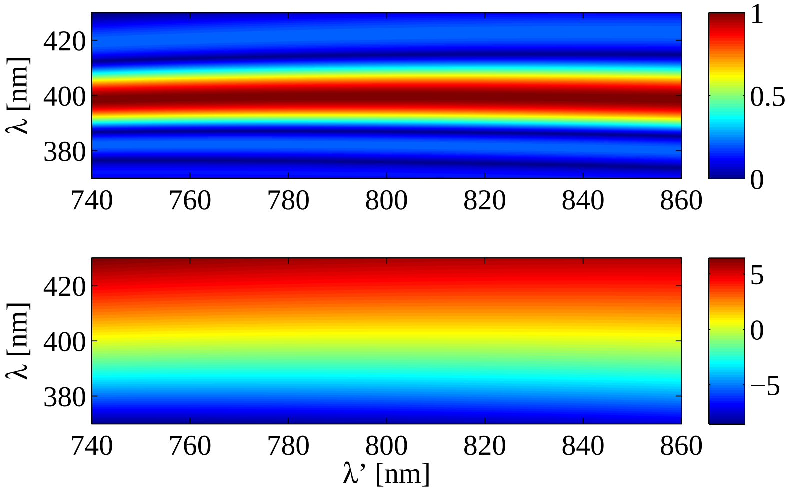

Figure 5.16: Amplitude (top) and phase (bottom) of the phase matching function $\tilde{\Phi}(\lambda, \lambda')$ for a 0.2-mm thick, 29.2°-cut BBO crystal illustrating both are relatively constant in signal wavelength λ'.

As the strong variation is primarily in λ, to first order we presume the effect of group velocity dispersion introduced by the phase mismatch can be factored out of the integral. That is,

$$\tilde{\Phi}(\omega, \omega') \approx \tilde{\Phi}(\omega, \omega_0) \tag{5.22}$$

so that Eq. (5.18) and Eq. (5.19) become

$$\tilde{E}_{FROG}(\omega, \tau) \propto L\tilde{\Phi}(\omega, \omega_0) \int \tilde{E}(\omega - \omega')\tilde{E}(\omega')e^{i\omega'\tau}d\omega'. \tag{5.23}$$

$$I_{FROG}(\omega, \tau) \propto L^2 \left|\tilde{\Phi}(\omega, \omega_0)\right|^2 \left|\int \tilde{E}(\omega - \omega')\tilde{E}(\omega')e^{i\omega'\tau}d\omega'\right|^2. \tag{5.24}$$

As noted in [91, 97, 101], there is a spectral modulation of the FROG signal from the group velocity mismatch. For linearly varying Δk, the blue SFG light falls off as sinc^2 imposing a maximum spectral bandwidth that can be generated. This modulation is shown for our crystal in Fig. 5.17.

This spectral modulation is equivalent to a convolution of the time-domain signal with its Fourier transform, imposing an effective time resolution inversely related to the modulating bandwidth. To estimate the

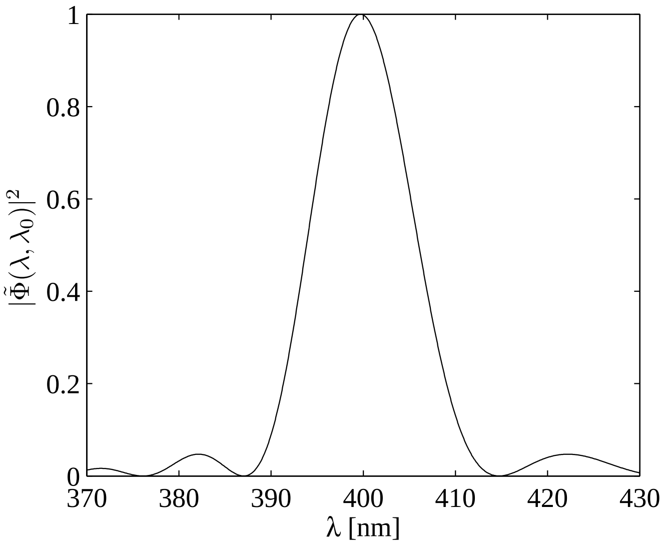

Figure 5.17: Conversion efficiency at the laser fundamental wavelength $\lambda_0 = 800$ nm for a 0.2-mm thick, 29.2°-cut BBO crystal. The resulting phase-matched FWHM bandwidth is $\Delta\lambda = 12.2$ nm at $\lambda = 400$ nm with a corresponding time resolution of $\Delta t = 38.8$ fs.

bandwidth, first we note that $\mathrm{sinc}^2(\Delta kL/2)$ reaches its half-maximum when the argument $\Delta kL/2 \approx 1.39$. By expressing (5.14) in wavelength as the values of $n(\lambda)$ are typically specified, Δk can be expanded to first order in λ for a small change $\Delta\lambda$ about the second harmonic $\lambda_0/2$. We then solve for the value of $\Delta\lambda$ that yields half maximum.

From this the FWHM phase matching bandwidth is found to be

$$\Delta\lambda = 0.221\frac{\lambda_0}{L}\left|\frac{dn_o(\lambda_0)}{d\lambda} - \frac{1}{2}\frac{dn_e'(\lambda_0/2)}{d\lambda}\right|^{-1}. \tag{5.25}$$

The transform to the time domain yields a corresponding temporal FWHM resolution of

$$\Delta t = \frac{\lambda_0 L}{c}\left|\frac{dn_o(\lambda_0)}{d\lambda} - \frac{1}{2}\frac{dn_e'(\lambda_0/2)}{d\lambda}\right|. \tag{5.26}$$

When expressed in terms of the group velocities v and angular velocity ω, these are equivalent to the results of [91, 101]. Using these, the spectral resolution of the FROG crystal (Fig. 5.17) is $\Delta\lambda = 12.2$ nm at $\lambda = 400$ nm for a temporal resolution of $\Delta t = 38.8$ fs. This is sufficient to resolve the bandwidth-limited laser pulse length of ~100 fs.

As a final note, implicit throughout is the assumption that the beam, its replica, and their alignments with respect to the crystal are identical. If one beam differs by a constant scale factor from the other, this only scales the measured signal and can be tolerated. Where different spectral modulations are imparted this is not the case and erroneous asymmetries may arise in the resulting FROG trace.

Regarding the optical system, the process of splitting the beam is largely symmetric. Both beams are transmitted and reflected once by the splitter. The vertically displaced beam (Fig 5.13) undergoes one additional reflection and has its vertical polarization reversed by the roof mirror. The change in field polarity isn't significant to the measurement, but the additional mirror must have a flat response over all laser wavelengths. As the optics are chosen to be broadband to ensure the light reaching the crystal is reasonably identical to the pulse entering the system, this is considered negligible.

The choice of the laser being polarized in the vertical plane of incidence (Fig 5.14) is preferred due to higher order effects arising from the geometric dependence of the phase matching. One might suggest using horizontally polarized light and subsequently rotating the crystal 90°, however in this case the angle between each non-collinear beam and the optic axis of the crystal is not equal. The collinear second harmonic rays for each beam will then have different phase matching efficiencies. As a result the amplitudes will be depleted at different rates by the discarded SHG beams generating a small asymmetry in the encoding of the SFG signal.

Assuming the system to be well aligned to mitigate these effects, we proceed with analysis of the ideally measured trace.

5.3.1.3 SHG FROG traces and reconstruction

Before detailing the reconstruction process, there are properties of the SHG FROG trace that are of special significance for acquisition and pre-processing. Some indicate the limitations of the measurement while others provide indicators of an improperly set up experiment as well as means to correct for certain experimental errors [90–92, 97, 98].

Following from Eq. (5.19), we specify the ideal trace we want to measure $I_{FROG}(\omega, \tau)$ as

$$I_{FROG}(\omega, \tau) = \left| \int \tilde{E}(\omega - \omega')\tilde{E}(\omega')e^{i\omega'\tau}d\omega' \right|^2 . \tag{5.27}$$

From Eq. (5.24) in the presence of crystal dispersion with linear contributions in Δk, we have a measured trace $I_{FROG}^{meas}(\omega,\tau)$ that is

$$I_{FROG}^{meas}(\omega,\tau) = \left|\tilde{\Phi}(\omega,\omega_0)\right|^2 I_{FROG}(\omega,\tau). \tag{5.28}$$

where $\tilde{\Phi}$ is given by Eq. (5.17).

It's easily shown that both traces are symmetric in delay so that $I(\omega,\tau) = I(\omega, -\tau)$. When this isn't the case for an experimentally measured trace, misalignment of the system or crystal is implied and should be corrected.

As a consequence of this symmetry, it is well understood that there is an ambiguity regarding the overall sign of the recoverable phase [90, 91]. In practice this is trivial as one can typically deduce the sign of the dispersion causing pulse broadening by inspection of the optical system. Where this isn't apparent it can be readily determined by adding additional known dispersion (such as a piece of glass) and observing the change in the measured chirp.

It's also straightforward to show that the frequency marginal $M_\omega(\omega)$ for the ideal trace is [90, 97, 98]

$$M_\omega(\omega) \equiv \int_{-\infty}^{\infty} I_{FROG}(\omega,\tau)d\omega = \int_{-\infty}^{\infty} I(\omega')I(\omega-\omega')d\omega'. \tag{5.29}$$

For an ideal SHG FROG trace we see that $M_\omega(\omega)$ is the autoconvolution of the spectral intensity. For $I(\omega)$ with a center band of ω_0, the autoconvolution has a center frequency of $2\omega_0$.

Integrating Eq. (5.28) over τ for the measured trace with some phase matching contributions we have instead the marginal

$$M_\omega^{meas}(\omega) = \left|\tilde{\Phi}(\omega,\omega_0)\right|^2 M_\omega(\omega). \tag{5.30}$$

Remarkably, this indicates that spectral modulations in the measured, doubled signal such as those of crystal dispersion (to first order) can be experimentally corrected if one also measures the incident IR spectrum. This holds true as well for any other spectral modulation introduced to the SFG signal before being recorded such as the effect of the filters or amplitude modulations from the spectrometer being poorly characterized.

Using a well-calibrated near-IR spectrometer, the incident IR spectrum is measured for reference before it enters the BBO crystal. This is used to compute the intensity autoconvolution $A(\omega)$ which is equal to the ideal frequency marginal $M_\omega(\omega)$ by (5.29). Because the ideal and measured traces should differ only in the ratio of their frequency marginals in this estimate, the ideal case is $A(\omega)/M_{\omega}^{meas}(\omega) = $ constant. This would indicate a flat spectrometer response and negligible phase matching losses.

Conversely, large discrepancies typically indicate poor phase matching (possibly bad crystal alignment) or improperly calibrated spectrometers and should be addressed. Where some discrepancy still remains, however, we can also generate a spectrally corrected experimental FROG trace

$$\begin{aligned} I^{corr}(\omega,\tau) &= \frac{A(\omega)}{M_{\omega}^{meas}(\omega)}\, I^{meas}(\omega,\tau) && (5.31) \\ &= I(\omega,\tau). && (5.32) \end{aligned}$$

While there is no substitute for properly taken data, this corrective capability is a rather remarkable feature of the SHG FROG trace used to remove systematic errors in phase recovery [90, 97, 98].

Integrating now over the frequency axis, the delay marginal is

$$M_{\tau}(\tau) \equiv \int_{-\infty}^{\infty} I_{FROG}(\omega,\tau)d\omega = \int_{-\infty}^{\infty} I(t)I(t-\tau)dt, \tag{5.33}$$

which is the autocorrelation of the temporal laser intensity $I(t)$.

Though we can of course provide more meaningful information by eventually using the full trace to reconstruct the temporal profile $I(t)$, this can provide a quick estimate of the pulse width. For example, assuming an approximately Gaussian temporal profile yields an autocorrelation with a width that is $\sqrt{2}$ larger. For a sech^2 pulse, it's $\sim$1.54 times larger. Then by taking the width of the delay marginal and dividing by the assumed factor, the pulse width is estimated.

As an autocorrelation function, $M_{\tau}(\tau)$ is maximum and symmetric in the parameter τ where there is zero delay between the two signals. This may be non-zero for real data. As reconstruction will assume the delay axis is symmetric about zero, the maximum, or more precisely, the first-order moment of the delay marginal [91] is calculated to shift the axis of measured data to zero offset.

This otherwise provides a final consistency check as the autocorrelation of the recovered temporal profile $I(t)$ should agree with the delay marginal $M_{\tau}(\tau)$.

With these consistency checks in mind while data taking, an experimental trace is then generated taking into consideration the Nyquist sampling criterion when selecting the delay range and step size with respect to the spectral range of interest [90]. Recovery of the amplitude and phase is then accomplished using an iterative reconstruction algorithm. The details of efficient computational reconstruction become involved.

Our FROG traces were analyzed using the *FROG* software package by Femtosoft Technologies [102], referenced on the research of Trebino and Kane, *et al* [90, 91, 103, 104].

In summary, the 2D problem of finding the amplitude and phase begins with an initial guess of the complex laser signal $\tilde{E}_{sig}(\omega,\ t)$ with its complex spectral and temporal field profiles related by Fourier transform. A corresponding trace $I_{sig}(\omega,\ \tau)$ is generated computed by Eq. 5.27. The RMS error between this and the recorded trace $I(\omega,\ \tau)$ is minimized with respect to a scaling factor α as

$$G = \sqrt{\frac{1}{N^2} \sum_{i,j} \left| I_{ij}(\omega_i,\ \tau_j) - \alpha I_{ij,sig}(\omega_i,\ \tau_j) \right|}, \tag{5.34}$$

where both are sampled over discrete points i and j. This is referred to as the FROG error [102] and is the standard measure for the goodness of fit for the guessed signal $\tilde{E}_{sig}$.

From here variations of $\tilde{E}_{sig}$ are iterated to further minimize G. The selection criterion for the next best $\tilde{E}_{sig}$ varies depending on the optimization algorithm applied (e.g., a basic steepest decent algorithm or the more rapid method of generalized projections [90, 91]). The software also allows alternating between the various algorithms. Changes in technique are used to help avoid trapping in a local minimum during optimization and can greatly enhance the speed for solutions involving complex structure.

The process is allowed to iterate until the FROG error reaches satisfactory convergence. Assuming the above consistency checks are in reasonable agreement and depending on the level of noise in the experimental data, a final FROG error of $< 1\%$ is considered acceptable.

5.3.2 FROG measurements

For these measurements an Ocean Optics *Jaz* spectrometer with an 1800 lines/mm grating for fine spectral resolution in the 400-nm range was used. To measure the IR spectra for comparison and correction by the frequency marginal, an Ocean Optics *HR4000* spectrometer is used. A MATLAB interface was written to manage data acquisition and reformatting for input and output with the Femtosoft reconstruction software.

5.3.2.1 Pulse length optimization

For ultrashort pulse generation we start by measuring the spectral phase of the maximally compressed *Spitfire* output. To reduce the effect of statistical error, the measurement and reconstruction are repeated ten times with the *Dazzler* operating in self-compensating mode. The average of the recovered spectral phase curves is taken as their mean after setting a constant spectral phase $\phi(\omega)$ and slope $\phi\prime(\omega)$ at $\lambda = 800$ nm for all traces to neglect the known phase and delay ambiguity from SHG FROG reconstruction [90].

This numeric phase curve can then be directly programmed for subtraction by the *Dazzler* and the measurement is repeated. To allow for the overall sign ambiguity of SHG FROG, we analyze the resulting trace using both the positive phase correction file and its negative. Indeed, only one is found to improve pulse compactness.

Before reconstruction, the raw traces are preprocessed by spectrometer background subtraction and by frequency marginal (Sec. 5.3.1.3). The *FROG3* software transparently manages conversion of the data from a constant-wavelength sampling to the constant-frequency sampling required by the Fourier relations [102].

Though the recovered spectral phase before compensation is needed to generate the compensated trace, for illustration all data is shown side-by-side. A comparison of representative raw, preprocessed and recovered traces both pre- and post-correction are shown in Fig. 5.18 with the corresponding marginals for all of these shown in Fig. 5.19.

For consistency we first inspect the marginals. Preprocessed and reconstructed $M(\lambda)$ are nearly identical, as should be the case where the spectral marginal correction has been applied. Also, preprocessing has negligible impact on delay profiles making the raw and preprocessed $M(\tau)$ also nearly indistinguishable. The comparison of raw to reconstructed marginals is reasonable within some clear instrumental noise, and the marginals (and raw traces) are reasonably symmetric in delay.

The corresponding reconstructed amplitudes and phases are shown in Fig. 5.20 for the pulse pre- and post-compensation. All measured traces fit with to a FROG error of $< 0.35\%$. Before adding TOD compensation a cubic spectral phase with TOD of greater than 6×10^5 fs^3 is observed producing a longer tail in the temporal profile. Likewise in the initial trace (Fig. 5.18), “whiskers” appear in the delay direction of FROG traces associated with the initial pulse, yielding the pinched ellipse shape characteristic of the presence of TOD [90]. This also appears in the relatively slower fall off in the tail of the delay marginal (Fig. 5.19, bottom) which are the temporal intensity autocorrelations.

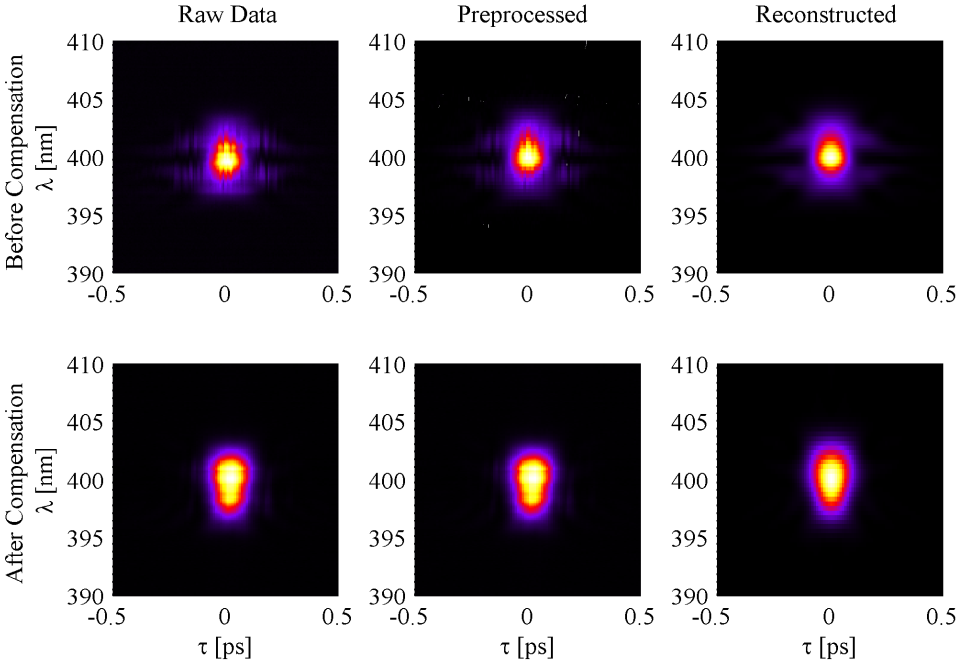

Figure 5.18: Representative raw and preprocessed SHG FROG traces and their resulting reconstructed traces. The nonlinear spectral phase determined from repeated measurements of the top pulse is subtracted by the AOPDF to produce the bottom series.

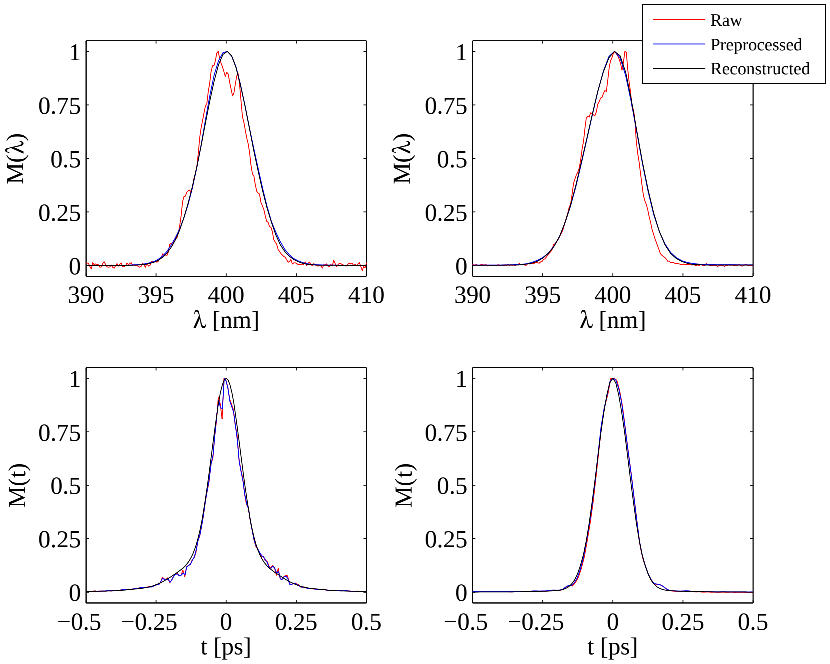

Figure 5.19: Spectral (top) and delay (bottom) marginals of traces (Fig. 5.18) before (left) and after (right) compensating for the dispersion of the pulse on the left.

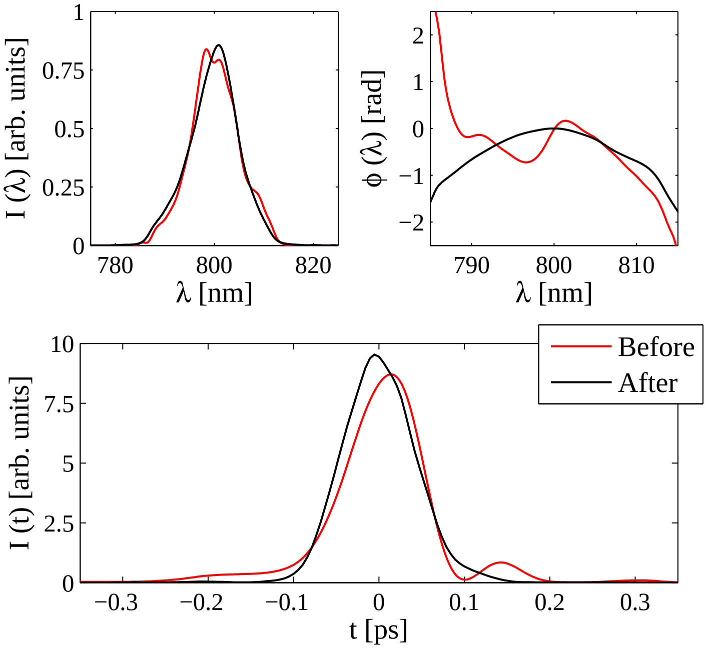

Figure 5.20: Reconstructed temporal and spectral profiles of a maximally compressed pulse before and after subtraction of the measured third order dispersion, shown as $\phi_{before}(\lambda)$ (red curve, top right).

With the measured spectral phase subtracted by the *Dazzler* pulse shaper, the shoulders in the field are suppressed though a small, 827 fs^2 of second order dispersion remains. The associated trace accordingly takes the form of a more compact ellipse. The result is the initial profile standard deviation of 78.7 fs being reduced to 49.2 fs (98.4 fs FWHM) with a more uniform IR pulse.

Repeatability of the FROG traces and subsequent profile reconstruction is also quite good. The ten independently measured and analyzed profiles for the uncompensated pulse are shown in Fig. 5.21. The standard deviation in the temporal FWHM of these is found to be just 3 fs. As this technique requires many shots to acquire each trace, this indicates both excellent laser and diagnostic stability.

With clean pulses of 100-fs duration produced, the laser system has subsequently been used in UV drive mode to successfully produce ellipsoidal bunches [105].

5.3.2.2 Chirped pulse measurement

For EOSD, a pulse length of as much as 5 ps is desired to allow a sufficiently long sampling window. As the *Dazzler* can only produce a maximum chirped length of approximately 2 ps for the given laser bandwidth, the grating compressor of the *Spitfire* was instead adjusted to provide the longer pulse. Moderate variations of the pulse length can then be made on the fly using the programmable *Dazzler*. As the compressor stage of the *Spitfire* provides no readback for pulse length or stage position settings, independent measurement of the under compression is done by SHG FROG.

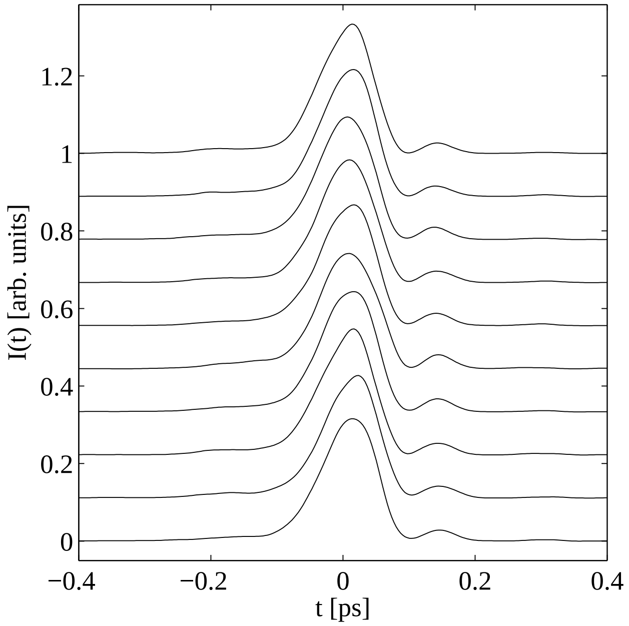

Figure 5.21: Temporal profiles from ten independently measured and analyzed SHG FROG traces used to determine the uncompensated laser dispersion.

Traces for an example chirped pulse measurement are shown in Fig. 5.22. For diagnosing a long pulse such as this, a large 1024 × 1024 pixel FROG grid must be used to satisfy the Nyquist conditions as the spectral bandwidth demands a time step much smaller than the large relevant time scale.

The corresponding reconstructed phases and intensities are shown in Fig. 5.23. The associated FROG error was 0.798% yielding a bandwidth of 10.5 nm FWHM with group delay dispersion of 1.61×10^5 fs^2 and corresponding pulse width of 4.9 ps FWHM. The detailed phase information provided by this measurement alleviates errors in the decoding of EOSD signals as the laser pulse acts as the carrier upon which the diagnostic signal is encoded.

Chirped pulse lengths of 5 ps can be easily set and measured for applications in EOSD experiments to support single-shot measurements of the electron bunch duration downstream of the emittance-exchange beamline, which we report on in the following section.

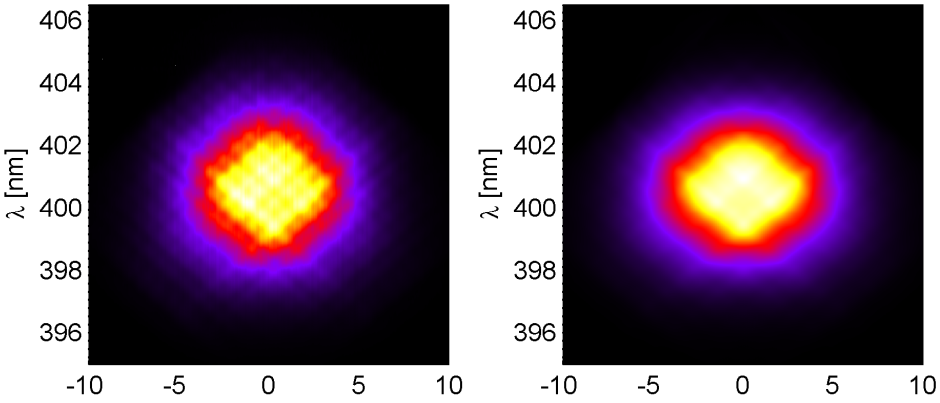

Figure 5.22: Experimental (left) and reconstructed (right) SHG FROG traces for a strongly chirped Ti:sapph laser pulse used for EOSD.

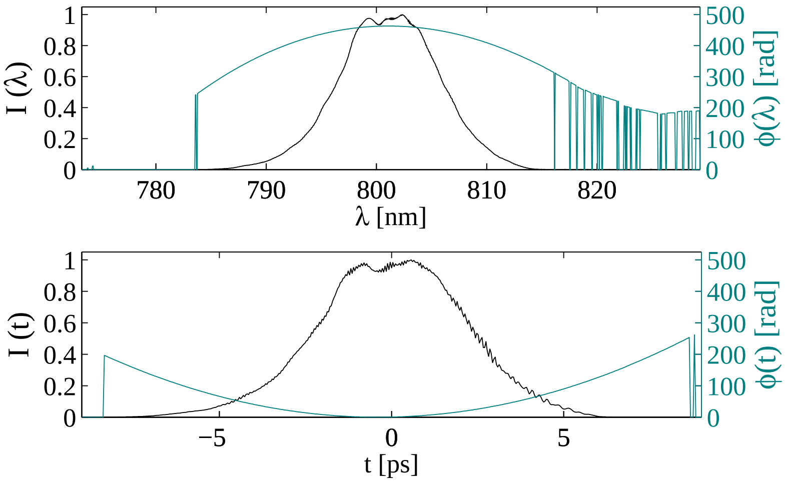

Figure 5.23: Reconstructed spectral (top) and temporal (bottom) profiles and phases for a strongly chirped laser pulse with a spectral bandwidth of 10.5 nm and pulse duration of 4.9 ps, FWHM.

CHAPTER 6

BEAM MEASUREMENTS

With the full system commissioned and characterized, we arrive at measurements taken of ultra-short bunches at A0PI. We initially investigate the use of the EEX beamline (Sec. 2.3) coupled with upstream focusing to tune the final bunch duration downstream of EEX.

For these measurements the photoinjector was setup to generate bunches with 250 pC total bunch charge with an energy of 14.3 MeV. A pyroelectric detector capable of measuring the integrated power of the THz-domain CTR from X24 is initially used to verify the presence of a sufficiently strong diagnostic signal.

A laser probe with chirped pulse length of 4.4 ps with an effective time resolution of 660 fs is then used to probe by EOSD. The CTR from diagnostic cross X24 (Fig. 2.6) is imaged to the EOSD breadboard (Fig. 4.4). Relative TR-to-laser time of arrival at the crystal was made synchronous using the method described in Sec. 4.3. The final timing is adjusted with a short scan of the laser timing over a few picoseconds until a polarization modulation is observed. That the modulation is due to EOSD at the crystal is verified by blocking the CTR signal from the beam to check that the modulation vanishes.

6.1 Establishing synchronization

In searching for the first electro-optic signal there will be many unoptimized factors reducing the strength of the signal. Chief among these is the temporal overlap of the CTR and laser pulses at the crystal. Referring to the synchronization scheme in Sec. 4.3, adjusting the relative delays seen on the photodiode and streak camera are straightforward as the range seen on both spans several orders of magnitude more than the uncertainty in the timing.

At the crystal, however, the detection range is of the order of a few picoseconds with a chirped pulse. The optical path delay difference between the laser pulse and CTR from the EO crystal to the broadband splitter that leads to the streak camera (Fig. 4.4) was estimated to be about -300 ps (the laser path is shorter than the CTR path) with an uncertainty of ~20 ps.

To maximize sensitivity in establishing the delay, simplified analyzing optics were added by a flip-in mirror after the collimating lens and before the spectral decoding analyzing optics in Fig. 4.4. No circular polarizer is used so that in the absence of any encoding at the crystal the laser is still nearly linear. A crossed polarizer is set to extinguish the laser with the light then focused on to a fast photodiode. Any induced birefringence will generate an increase in the orthogonally polarized light with the photodiode measuring the integrated value of the absolute signal (see Eq. (4.6)).

The laser delay is controlled using the Colby RF phase shifter to adjust the seed laser delay (Fig. 5.1) while monitoring peak diode voltage, stepping backward relative to the setting that synchronizes the signals at the beam combiner to the streak camera. The results of the first observed signal are shown in Fig. 6.1.

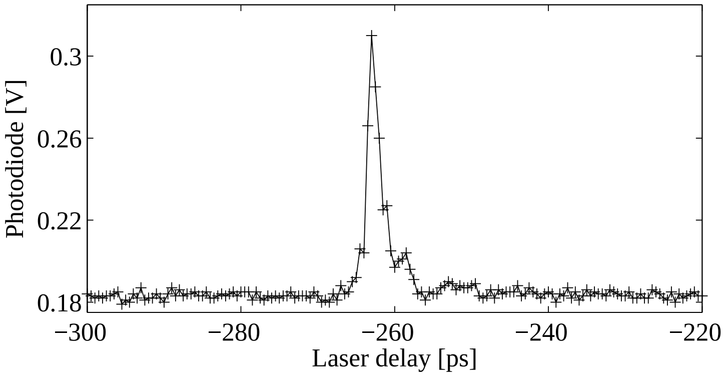

Figure 6.1: Photodiode signal measured after electro-optic encoding and a crossed polarizer as a function of laser delay to determine synchronization between CTR and laser pulses at the ZnTe crystal.

The background level observed is due to imperfect extinguishing of the laser, which easily saturates the photodiode in the absence of the crossed polarizer. A rise in the signal at a time delay of -263 ps is observed at a level 180 times higher than RMS background noise. The result is repeatable, and removing the CTR foil from the beam eliminates the signal indicating the presence of the signal is from the electro-optic interaction.

This multi-shot scanning approach also indicates the maximum width of the CTR. Experiments in multi-shot EOS have relied on this scanning technique (c.f. [61]). The temporal FWHM of the scan in Fig. 6.1 is 1.9 ps. However, because the scan is multi-shot, the 1-ps beam-to-laser jitter can artificially broaden the signal so that this value is only an upper limit.

The relative additional laser advance of ~260 ps was highly repeatable in all experiments and also easily found by observing signals resolved in the spectrometer (Fig. 4.5). With the correct timing and initial signal established, further optimization of other factors can be performed.

6.2 Dependence of signal strength on crystal orientation

The signal is further maximized by adjusting the coupling between the orthogonally polarized CTR and laser pulses in the crystal by remotely rotating the ZnTe crystal to produce the strongest signal. We expect this to have a dependence on the azimuthal rotation angle θ of the crystal given by (4.49) and that this produces only a constant amplitude modulation of the signal $\Gamma(\theta,\ t) = \sin[d_{eff}(\theta)E_{THz}(t)]$ being recorded.

This is verified in the signals deduced by spectral decoding in Fig. 6.2 where the crystal is rotated through 360° in 5° steps in the presence of a signal $\Gamma(t)$. For this plot the time of arrival differences arising from the beam-laser jitter have been removed by shifting the image row-by-row so all peak absolute values coincide on the time axis. We indeed see similar single-cycle oscillating signals for all crystal orientations aside from the difference of a relative amplitude factor.

The analytic dependence given by (4.49) is clear in Fig. 6.3 where we plot only the peak amplitudes of the data in Fig. 6.2 along $t = 0$. Included is a fit of Eq. (4.49) to the data using only a constant amplitude Γ_{peak} and unknown angular offset θ_0 as free parameters, showing excellent agreement. The strongest coupling in this case is observed at $\theta = 11°$ or 191°, with these differing by a sign in amplitude.

6.3 Initial single bunch results with comparison to interferometery

Shot-to-shot bunch duration optimization were then performed. The input quad Q3 is manually adjusted to vary the bunch length after EEX to find the shortest signal that can be achieved. These are shown in Fig. 6.4 for the initial signal we label "bunch 1" and the measurement for the optimized settings denoted "bunch 2."

A clear contraction of the EOSD signal is observed. However, strong signal distortions from phase mismatch in the crystal are also apparent (Sec. 4.4).

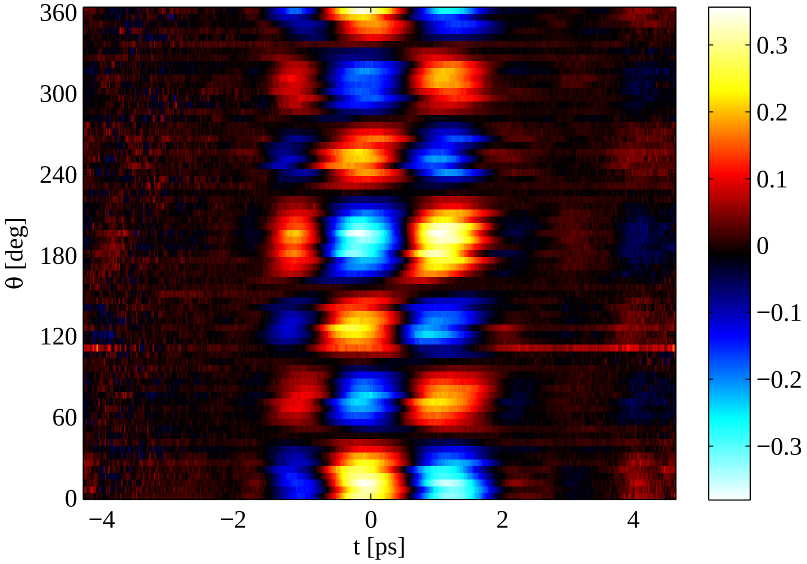

Figure 6.2: Variation of recovered EOSD signal $\Gamma(t)$ with azimuthal crystal rotation angle θ.

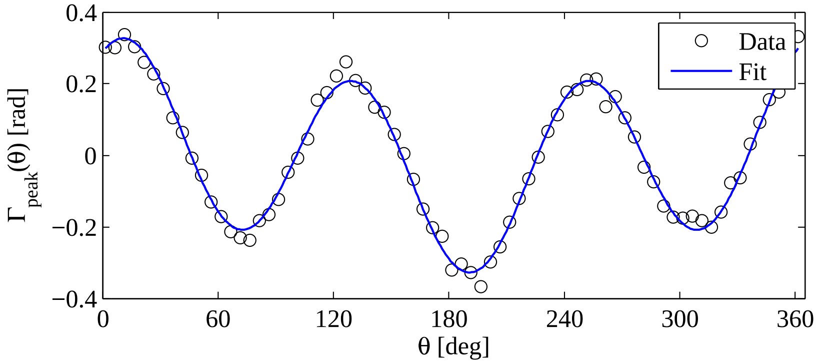

Figure 6.3: Peak amplitudes of $\Gamma(t, \theta)$ at $t = 0$ from Fig. 6.2 as a function of azimuthal crystal rotation angle θ with a fit to Eq. (4.49) with a constant amplitude and horizontal offset taken as the free parameters.

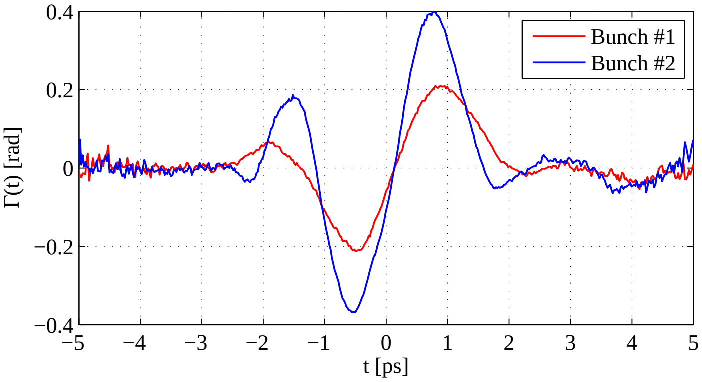

Figure 6.4: Recovered retardances $\Gamma(t)$ for different input quadrupole settings prior to EEX reflecting change in electron bunch length.

For comparison, we estimate the signal FWHM as half the width between extrema of one full cycle of the largest oscillation. For Fig. 6.4 these points occur in the vicinity of -1.8 ps and 0.8 ps in both sets. This results in durations of 1.44 ps for bunch 1 and 1.14 ps for bunch 2.

As an independent measurement, interferometry of the CTR was also performed independently using the Martin-Puplett interferometer (Sec. 2.5.1) also located at X24 for the same machine settings.

From Eq. (2.27) we had the expression for the measured Martin Puplett interferogram

$$IF_{MP}(\tau) \propto \int_{-\infty}^{\infty} \left| E_{THz}(t) + E_{THz}(t-\tau) \right|^2 dt. \tag{6.1}$$

If we assume that $E_{THz}(t)$ is real and that both the interferometer and EOSD are measuring the same transient with the recovered EOSD signal $\Gamma(t) \propto E_{THz}(t)$, we can use the data from Fig. 6.4 to compute an equivalent IF for EOSD as

$$IF_{EOSD}(\tau) \propto \int_{-\infty}^{\infty} \left| \Gamma(t) + \Gamma(t-\tau) \right|^2 dt \tag{6.2}$$

This supposes that the frequency-domain response function of both systems is quite similar, though we expect distortions from phase mismatch in the EOSD that are not present in the interferometer measurement and potentially different low-frequency losses.

We compare features of the measured and inferred interferograms to check for consistency as both signals are in principle derived by measuring the coherent THz spectrum of the TR. The result is shown in Fig. 6.5.

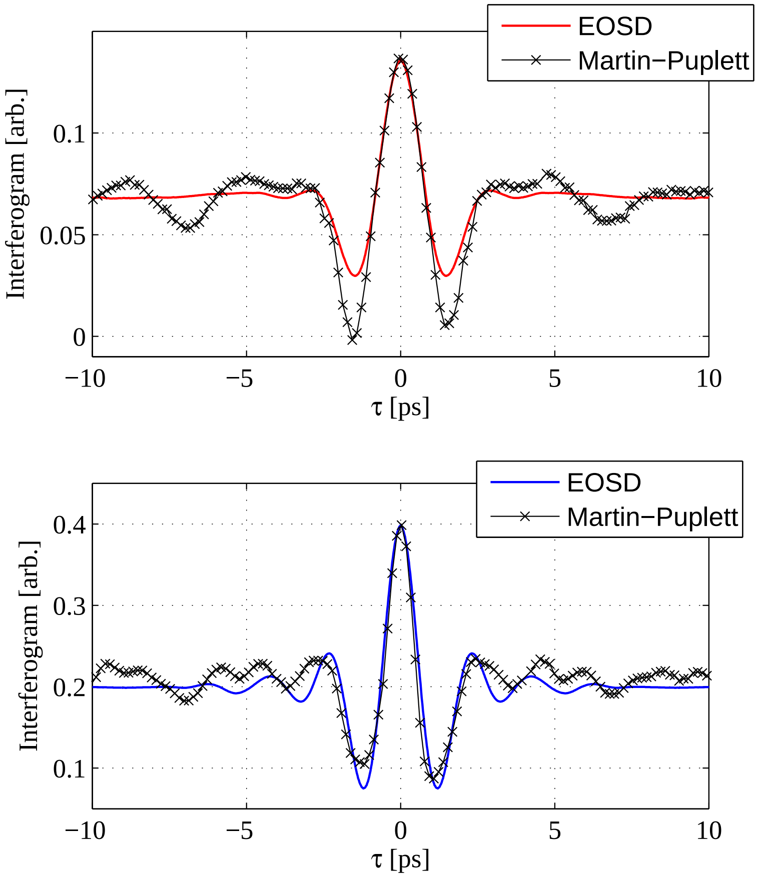

Figure 6.5: Comparison of interferograms measured by the Martin-Puplett interferometer to interferograms computed using the EOSD signals of Fig. 6.4 for the two different beam settings denoted bunch 1 (top) and bunch 2 (bottom).

As above, we define the FWHM of the IF as half the distance between the strong minima (in the vicinity of ±1.5 ps for all traces in Fig. 6.5). In this case, for the EOSD signals, the IF width of bunches 1 and 2 are 1.48 ps and 1.21 ps, respectively. Corresponding interferometer scans are in agreement with widths of 1.50 ps and 1.17 ps, respectively.

The two are in very good quantitative agreement, especially considering the differences in the measurement techniques. The advantage for EOSD, however, is of course that it produces the full trace in a single shot and with, in principle, no ambiguity as regards the shape of the signal $E_{THz}(t)$ which is difficult to reconstruct from an IF alone [36].

6.4 Double beam generation by laser masking

In the previous section tuning of the resulting bunch length was performed by changing the transverse size of the beam prior to EEX. We now instead demonstrate the generation of tunable, longitudinally double-pulsed electron bunches by imparting an initially transverse double beam structure.

Experimental results on the generation of electron bunch trains with sub-picosecond structure have been previously reported where an initial transverse electron beam modulation was produced by masking the electron beam directly [14].

The ability to shape the temporal profile in a non-interceptive way would be highly desired, especially for a high average current electron accelerator. Longitudinal shaping by transverse-to-longitudinal phase space exchange of a transverse beam modulation imparted instead by laser masking was suggested in [106]. This has great practical advantage over masking of the electron beam, primarily in that the laser mask is easily accessible during beam operations whereas a beam mask must be enclosed in the accelerator vacuum pipe and restricted to remote control.

Here we demonstrate proof of principle of this concept. By masking of the photoinjector drive laser to effectively produce two horizontally offset beams at photoemission in the RF gun, an initial transverse structure is generated. Moderate longitudinal profile tuning is then accomplished by again focusing the beam upstream of EEX.

However, the dynamics during photoemission and acceleration are quite complex. As the beam is still low energy, space charge forces can drive nonlinear expansion of the beam, distorting the shape imparted by the initial laser mask [107]. Further, the focusing solenoids that enclose the RF gun for initial collimation of the emerging beam also cause the beam to rotate during acceleration through the gun. This known as Larmor precession with the rotation angle as a function of propagation length $\theta(z)$ given by [107, 108]

$$\theta(z) = \int_0^z \frac{eB(z')dz'}{2m\gamma(z')\beta(z')c} \tag{6.3}$$

where **B** is the magnetic field in the solenoid and γ and β are the usual relativistic factors, now a function of z for the accelerating beam.

The drive laser mask used is a 4-mm diameter spot with a 1.5-mm wide rectangular block across the diameter. The spot as measured at the cathode is shown in Fig. 6.6. The magnification of the optical transport line from the laser room to the accelerator enclosure is observed with the spot now having a diameter of 6 mm. The two spots generated are given labels *a* and *b*.

Also shown in 6.6 is the resulting beam after the 9-cell accelerating cavity. An empirical approach is taken to adjusting the solenoid strength to produce the most distinct transverse modulation. As this in turn changes the rotation imparted by the Larmor precession we then adjust the rotation of the laser mask to compensate. Two horizontal spots on the beam are then resolved, though for the gun and solenoid settings used they lose some definition. The beamlets corresponding to spots *a* and *b* of the virtual cathode image are also labeled.

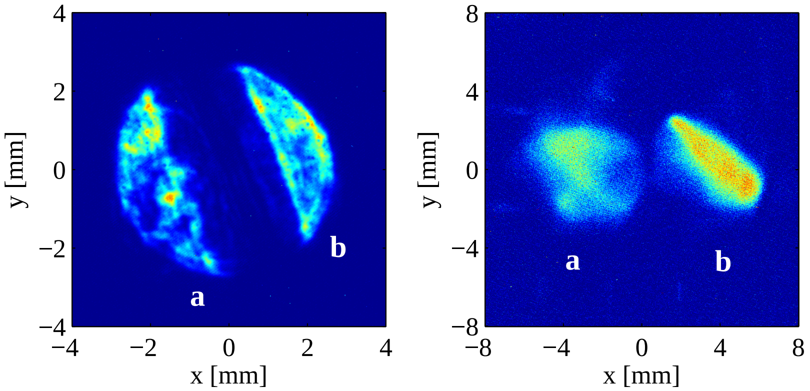

Figure 6.6: Raw images of the masked laser spot at the photocathode (left) and resulting transverse beam modulation after the 9-cell SCRF booster cavity (right). Labels *a* and *b* are assigned to the two generated beamlets and their corresponding laser spots.

We note that the vertical extent is nearly identical in both cases (6 mm) while horizontally the beam is blown out to a width of ~12 mm. As demonstrated in [107], this behavior is explained by space-charge expansion in the low-energy regime during the acceleration process.

As the dynamics of beam generation in the gun are highly nonlinear, again an empirical approach was taken to determine the resulting beam distribution. Emittance measurements after the booster cavity and before EEX (Fig. 2.1) were performed using the techniques described in Sec. 2.5.3. Longitudinal properties are shown in Table 6.1.

Table 6.1: Measured longitudinal properties for the double beam.

σ_z (mm)	σ_δ (mrad)	E$_0$ (MeV)	ϵ_z^* (mm-mrad)
0.68	0.65	14.1	12.2

The phase space ellipses for the transverse coordinates of the beamlets *a* and *b* were measured independently with the parameters, inferred emittances, and combined emittances in Table 6.2. These were then used to generated the Gaussian beam populations shown in Fig. 6.7.

Table 6.2: Results of transverse emittance measurement after acceleration for the double beam.

u	Beamlet	$\langle u \rangle$ (mm)	$\langle u' \rangle$ (mrad)	σ_u (mm)	$\sigma_{u'}$ (mrad)	$\sigma_{uu'}$ (mm/mrad)	ϵ_u^* (mm-mrad)	$\epsilon_{u,\text{total}}^*$ (mm-mrad)
x	a	-3.43	-1.04	1.57	0.10	0.14	4.4	22
	b	3.43	0.83	1.66	0.08	0.14	3.7	
y	a	0.01	0.32	1.77	0.13	0.20	6.2	8.5
	b	-0.01	0.02	1.45	0.10	0.21	4.2	

From Fig. 6.7 we see the desired double pulse in the horizontal x plane with the beamlets nearly overlapping in the y phase space. Both phase spaces are divergent so that the quad triplet Q1-Q3 (Fig. 2.1) is used to refocus the beam prior to EEX. For our experiment, a total bunch charge of 400 pC was used (~200 pC per beamlet) with an energy of 14.1 MeV. The quadrupoles upstream of the EEX line were set for Q1 = 0.5 A, Q2 = -0.8 A, with Q3 varied around the current setting found to maximize beam compression (0.5 A).

To see the effect of focusing and the EEX line, beam propagation from where the beam was measured down through the EEX line was computed using a MATLAB-based 3D ray-tracing program prepared using linearized transport matrices for machine parameters at A0PI. Space charge effects were not included in this calculation. The results for the longitudinal phase space after EEX are shown in Fig. 6.8.

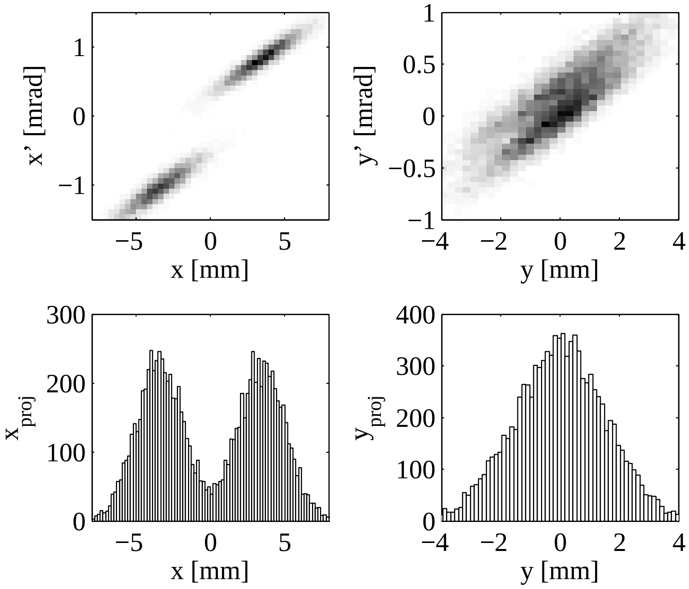

Figure 6.7: Transverse beam population deduced from measurements at the exit of 9-cell SCRF booster cavity prior to beam focusing and EEX.

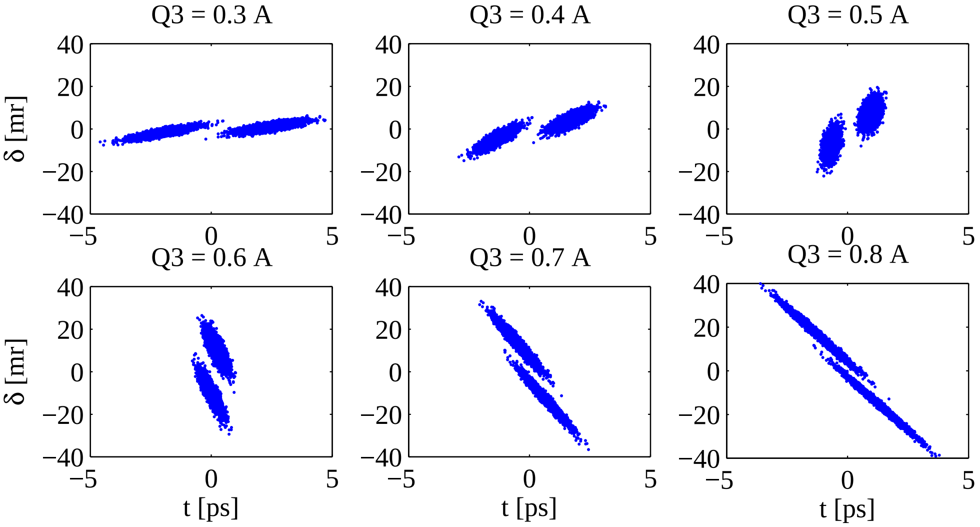

Figure 6.8: Simulated longitudinal phase spaces of the initial transverse double beam (Fig. 6.7) as a function of the current applied to the final focusing quadrupole magnet Q3 before EEX.

We see from the plots of Fig. 6.8 the effect of the transverse to longitudinal phase mapping. The initial transverse phase space follows a simultaneous shearing and rotation of the two ellipses in the resulting longitudinal phase space as a function of the focusing strength of the input quad strength Q3.

At 0.3 A the combined phase space shows a very narrow projection in energy spread δ with a long temporal projection in time t. At around 0.6 A, the two ellipses nearly overlap in time so that the temporal profile is nearly that of a single Gaussian bunch. Increasing the focusing strength further then smears the two ellipses in both energy and temporal spread.

In the range from 0.3 A to 0.6 A we can easily tune the duration and spacing of the double pulse in the longitudinal projection over the range of a few ps. This is illustrated in a more continuous fashion in Fig. 6.9 where only the longitudinal distribution as a function of Q3 current is shown.

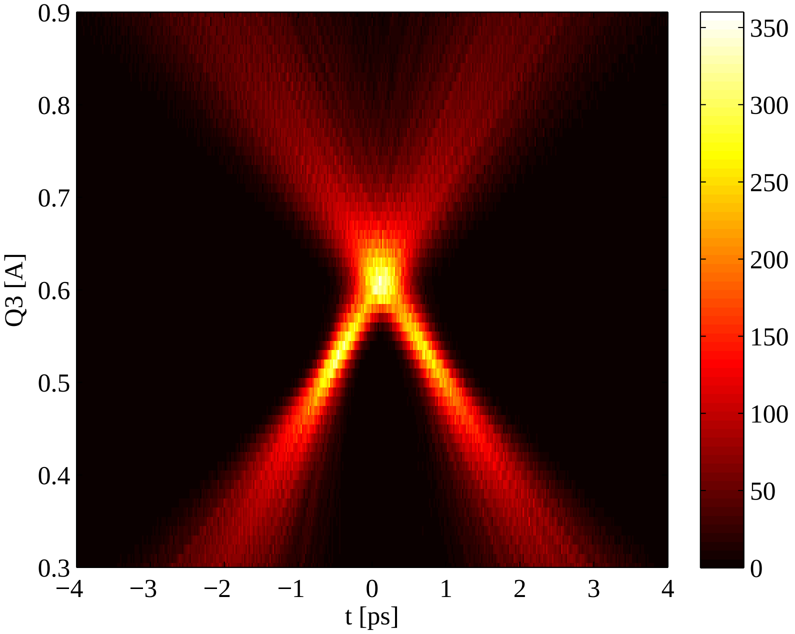

Figure 6.9: Simulated longitudinal distribution $\rho(t)$ as a function of the current applied to the final focusing quadrupole magnet Q3 before EEX.

6.5 Measurement of the double bunch

To verify the behavior of the longitudinal projection shown in Fig. 6.9, we turn to the diagnostics. For this measurement, a chirped pulse duration of 5 ps was used for the laser. With machine control and data acquisition automated, we scan the Q3 current and record the EOSD signal for each setting, as shown in Fig. 6.10. We have again removed the relative shot-to-shot timing fluctuations due to beam-laser jitter for illustration.

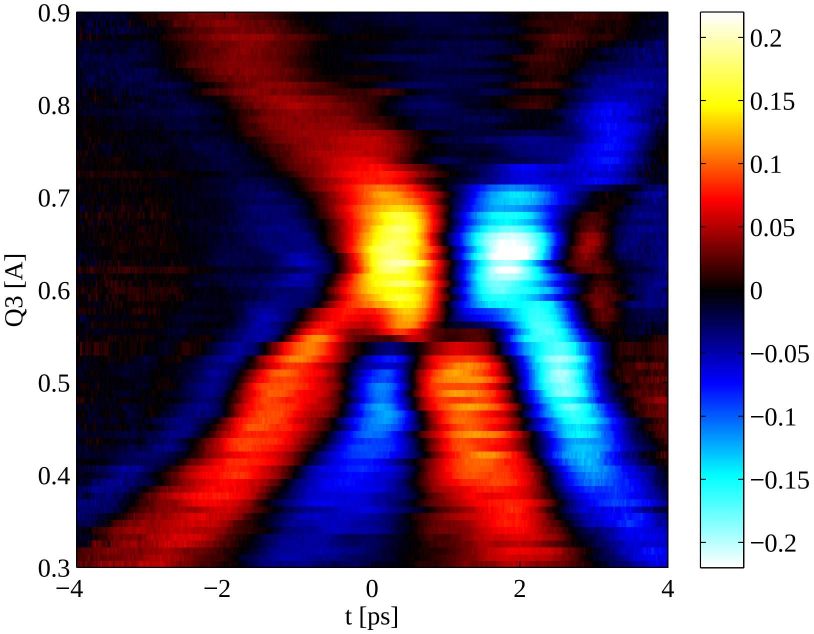

Figure 6.10: Recovered retardances $\Gamma(t)$ as a function of the current applied to the final focusing quadrupole magnet Q3 before EEX.

We note again the oscillatory nature of the signals as measured by EOSD. Good qualitative agreement to the simulation in Fig. 6.9 is still observed, however. For increasing quadrupole strength the two bright, compact signals converge to a single oscillatory cycle around 0.6 A before they again separate as each sub-bunch becomes stretched.

From this quadrupole scan we select a strong double pulse structure with Q3 = 0.48 A and compare the results of several repeated shots in Fig. 6.11. Excellent repeatability is observed.

As done previously, the double pulse structure is additionally verified by a Martin-Puplett interferometer scan with comparison to an equivalent EOSD interferogram computed using Eq. (6.2), shown in Fig. 6.12.

The strong secondary harmonic peaks in the interference pattern are resolved, again with quite good agreement in the spacing, width and amplitude of the peaks.

Finally we compare the bunch spacings and FWHM durations determined by EOSD in Fig. 6.10 with those of the simulation shown in Fig. 6.9. The result is shown in Fig. 6.13. While the trend for the bunch

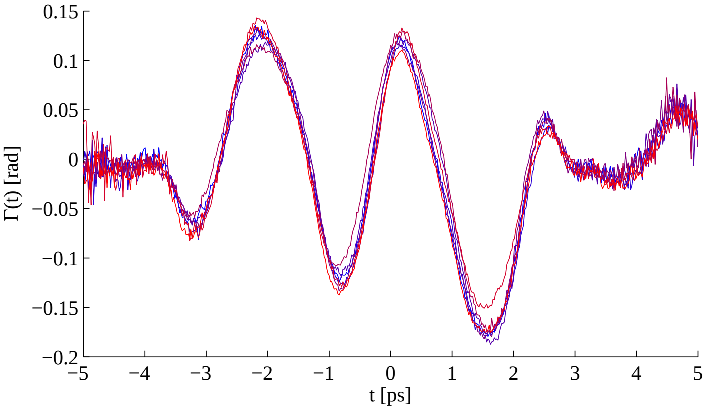

Figure 6.11: Repeated measurement of retardances $\Gamma(t)$ for a double bunch over seven shots. Relative differences in time of arrival have been removed.

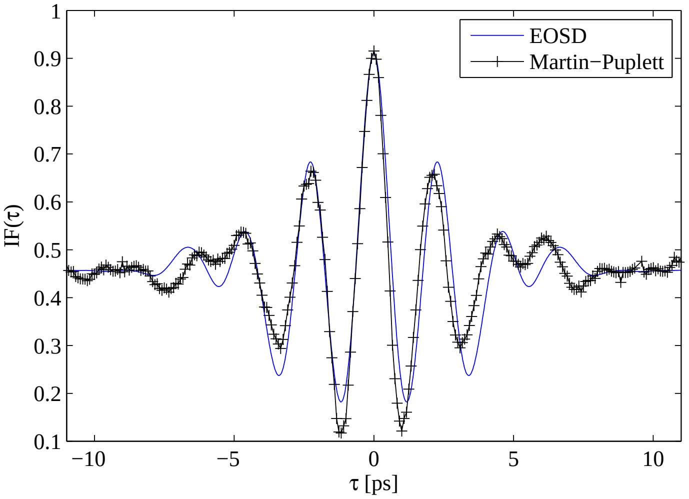

Figure 6.12: Comparison of interferogram generated using EOSD signal shown in Fig. 6.11 to independent measurement by Martin-Puplett interferometer.

spacing agrees well within the measurement limit, as the two converge there appears to be a discrepancy as the simulated bunch length decreases steadily to Q3 = 0.5 A with little reduction in the spread measured by EOSD. This may demonstrate the sacrifice in temporal resolution of overstretching the pulse necessary to accommodate the double-bunch quadrupole scan to include a longer temporal range for tune-up.

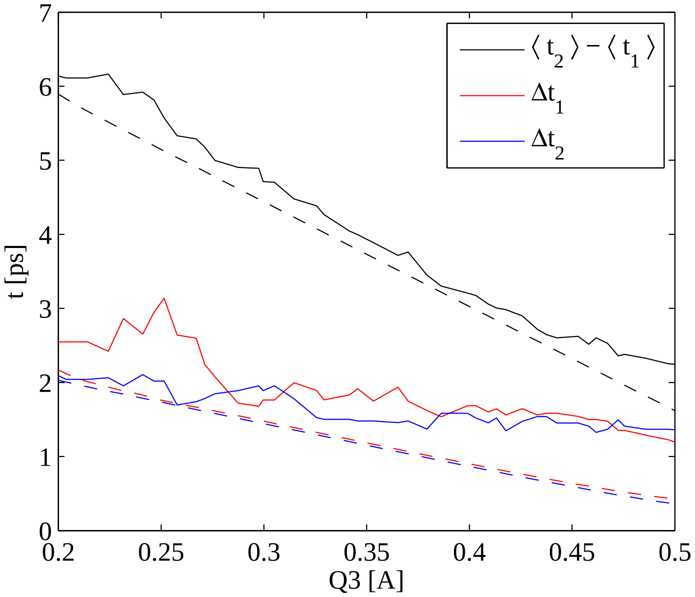

Figure 6.13: Comparison of measured (solid curves) and simulated (dashed curves) double bunch spacings $\langle t_2 \rangle - \langle t_1 \rangle$ and FWHM durations Δt_i for the quadrupole scan data of Fig. 6.9 and 6.10

However, there is also a likely a discrepancy in the linearized beam simulation which did not include space charge. Full simulations for A0 using ASTRA [50] have typically predicted a minimum electron bunch length of 1 ps in the presence of higher order effects.

CHAPTER 7

CONCLUSIONS

Design and installation of single-shot diagnostics for diagnosing the longitudinal properties of an electron beam with sub-picosecond time structure has been achieved.

As this was developed on the principle of laser-based, electro-optic spectral decoding, commissioning and characterization of a Ti:sapph laser at the A0 photoinjector was performed both for diagnostics and for use as an ultra-fast drive laser. Stable synchronization of the laser was accomplished to within 1 ps of the accelerator. Control and diagnosis of the laser's spectral amplitude and phase were achieved demonstrating laser pulse widths varied from 100 fs to 5 ps FWHM.

Transport and relative timing optics were installed to enable EOSD. Verification of the suggested geometric dependence of signal strength on crystal orientation relative to the probe and signal was also measured.

Though the technique is robust, minor artifacts typical of spectral decoding in a thick crystal are still observed. Thinner 200 μm and 500 μm ZnTe crystals were also tried in an attempt to improve temporal resolution due to dispersion, but with the thinner crystals there was no observable signal. The limitations of spectral decoding regarding the chirped length remain constrained by the length of the temporal window desired to envelop the signal.

Of remaining interest are the strongly bipolar waveforms measured by EOSD. By this we mean the near-unity ratio of the peak positive to negative amplitudes observed in the traces. Attempts to account for this by low-frequency dispersion and the chirped pulse distortions do not significantly account for this effect. Secondary reflections of the THz signal within the crystal have also been studied in a manner following [66, 69] but have shown negligible effect.

The primary influence is suspected to be in an underestimate of the low-frequency losses as the diffraction-limited spot size of the laser at the crystal is only 30 μm is the effective detector aperture. In this case a half-width low-frequency cutoff approaching 0.5 THz is possible as an even smaller percentage of the larger low-frequency CTR components are sampled. Combining this with a high-frequency cutoff established by the incident bunch length, the spectral intensity begins to appear as a broadband Gaussian centered in the 0.3-THz range, resulting in a near single-cycle transient.

It is also interesting that the two very different diagnostic techniques agree so consistently. They both probe the same signal in the same regime, though with different transfer functions that largely depend on the detector acceptance. With computed relative response functions included, the minor discrepancies between the two measurements may prove useful in verifying the accuracy of theoretical modeling.

While more work is necessary to fully account for this, beams of picosecond structure are successfully resolved showing excellent agreement with existing interferometric diagnostics. From a practical point of view, the advantage of the single-shot EOSD over interferometry is significant, as one can monitor changes to the longitudinal distribution live during beam tuning without the long wait and additional noise of a multi-shot scan.

Using the system developed, a longitudinally shaped electron beam utilizing novel laser masking and A0PI's emittance exchange line was demonstrated for applications in future light sources. The hardware developed here will eventually be installed at the Advanced Superconducting Test Accelerator, a 1-GeV electron accelerator currently under construction at Fermilab.

Tuning of a double pulse structure with variable bunch spacing has been measured by the diagnostics with the spacing observed in agreement with beam simulations. Experimental verification of transverse structure being preserved through acceleration can offer significant advantages over the shaping technique demonstrated in [14] by directly masking the beam after acceleration. A patterned laser can instead be used to impart a longitudinal modulation after EEX.

To impart a very fine modulation, a patterned cathode is alternately being suggested [109] using a nanocathode field-emission array. Nanometer-scale transverse modulations could then be produced, generating a longitudinal density modulation of the same order. By inverse Compton scattering of the resulting beam with a pulsed laser, coherent, attosecond x-ray pulses could in principle be generated by a relatively compact source, paving the way for a new generation of light sources.

REFERENCES

[1] J. M. J. Madey, “Stimulated Emission of Bremsstrahlung in a Periodic Magnetic Field,” Journal of Applied Physics **42**, 1906 (1971).

[2] L. R. Elias, W. M. Fairbank, J. M. J. Madey, H. A. Schwettman, and T. I. Smith, “Observation of stimulated emission of radiation by relativistic electrons in a spatially periodic transverse magnetic field,” Phys. Rev. Lett. **36**, 717 (1976).

[3] F. A. Hopf, P. Meystre, M. O. Scully, and W. H. Louisell, “Classical theory of a free-electron laser,” Phys. Rev. Lett. **37**, 1215 (1976).

[4] D. A. G. Deacon, L. R. Elias, J. M. J. Madey, G. J. Ramian, H. A. Schwettman, and T. I. Smith, “First operation of a free-electron laser,” Phys. Rev. Lett. **38**, 892 (1977).

[5] A. H. Zewail, “Four-dimensional electron microscopy,” Science **328**, 187 (2010).

[6] ILC Global Design Effort, “ILC Reference Design Report, Vol. 3,”, `http://www.linearcollider.org/about/Publications/Reference-Design-Report` (2007).

[7] D. J. Jackson, *Classical Electrodynamics* (Wiley, New York, 1998), 3rd ed.

[8] C. A. Brau, *Modern Problems in Classical Electrodynamics* (Oxford University Press, New York, 2004).

[9] D. J. Griffiths, *Introduction to Electrodynamics* (Prentice Hall, New Jersey, 1999), 3rd ed.

[10] J.-P. Carneiro, N. Barov, H. Edwards, M. Fitch, W. Hartung, K. Floettmann, S. Schreiber, and M. Ferrario, “Transverse and longitudinal beam dynamics studies at the Fermilab photoinjector,” Phys. Rev. ST Accel. Beams **8**, 040101 (2005).

[11] J. Li, R. Tikhoplav, and A. Melissinos, “Performance of the upgraded laser system for the Fermilab-NIU photoinjector,” Nucl. Instrum. Meth. A. **564**, 57 (2006).

[12] T. Koeth, Ph.D. thesis, Rutgers University, Piscataway, NJ (2009).

[13] J. Ruan et al., “First Observation of the Exchange of Transverse and Longitudinal Emittances,” Phys. Rev. Lett. **106**, 244801 (2011).

[14] Y.-E. Sun et al., “Tunable Subpicosecond Electron-Bunch-Train Generation Using a Transverse-To-Longitudinal Phase-Space Exchange Technique,” Phys. Rev. Lett. **105**, 234801 (2010).

[15] T. W. Koeth et al., in *Proc. of the 2007 IEEE Particle Accelerator Conference* (Albuquerque, New Mexico, 2007), p. 3663.

[16] E. Courant and H. Snyder, “Theory of the alternating-gradient synchrotron,” Ann. Phys.-New York **3**, 1 (1958), ISSN 0003-4916, URL `http://www.sciencedirect.com/science/article/pii/0003491658900125`.

[17] H. Wiedemann, *Particle Accelerator Physics* (Springer, 2007), 3rd ed.

[18] G. Hoffstaeter, “Advanced accelerator physics,”, Lecture Notes for US Particle Accelerator School (2010).

[19] P. Emma, Z. Huang, K.-J. Kim, and P. Piot, “Transverse-to-longitudinal emittance exchange to improve performance of high-gain free-electron lasers,” Phys. Rev. ST Accel. Beams **9**, 100702 (2006).

[20] M. Cornacchia and P. Emma, “Transverse to longitudinal emittance exchange,” Phys. Rev. ST Accel. Beams **5**, 084001 (2002).

[21] B. Jiang, J. G. Power, R. Lindberg, W. Liu, and W. Gai, “Emittance-exchange-based high harmonic generation scheme for a short-wavelength free electron laser,” Phys. Rev. Lett. **106**, 114801 (2011).

[22] V. Ginzburg and I. Frank, “Radiation of a uniformly moving electron due to its transition from one medium into another,” J. Phys. USSR p. 353 (1945).

[23] V. L. Ginzburg, “Transition Radiation and Transition Scattering,” Phys. Scr. pp. 182–191 (1982).

[24] C. Settakorn, Ph.D. thesis, Stanford University, Stanford, CA (2001).

[25] A. G. Shkvarunets and R. B. Fiorito, “Vector electromagnetic theory of transition and diffraction radiation with application to the measurement of longitudinal bunch size,” Phys. Rev. ST Accel. Beams **11**, 012801 (2008).

[26] V. Lebedev, “Diffraction-limited resolution of the optical transition radiation monitor,” Nucl. Instrum. Meth. A **372**, 344 (1996).

[27] N. Carron, “Fields of Particles and Beams Exiting a Conductor,” Prog. Electromagn. Res. pp. 147–183 (2000).

[28] S. Casalbuoni, B. Schmidt, and P. Schmüser, “Far-Infrared Transition and Diffraction Radiation,”, TESLA Report 2005-15 (2005).

[29] M. Castellano, A. Cianchi, G. Orlandi, and V. Verzilov, “Effects of diffraction and target finite size on coherent transition radiation spectra in bunch length measurements,” Nucl. Instrum. Meth. A **435**, 297 (1999).

[30] J. van Tilborg, Ph.D. thesis, Eindhoven University of Technology (2006).

[31] D. Xiang, W.-H. Huang, and Y.-Z. Lin, “Imaging of high-energy electron beam profile with optical diffraction radiation,” Phys. Rev. ST Accel. Beams **10**, 062801 (2007).

[32] H. Loos et al., in *Proceedings of FEL2008* (Gyeongju, Korea, 2008), p. 485.

[33] T. J. Maxwell, Master’s thesis, Northern Illinois University (2007).

[34] T. J. Maxwell, D. Mihalcea, and P. Piot, in *Proc. of 2008 IEEE Beam Instrumentation Workshop* (Lake Tahoe, CA, 2008), p. 1097.

[35] A. S. Marathay and J. F. McCalmont, “Vector diffraction theory for electromagnetic waves,” J. Opt. Soc. Am. A **18**, 2585 (2001).

[36] D. Mihalcea, C. L. Bohn, U. Happek, and P. Piot, “Longitudinal electron bunch diagnostics using coherent transition radiation,” Phys. Rev. ST Accel. Beams **9**, 082801 (2006).

[37] R. Thurman-Keup, R. Fliller, and G. Kazakevich, in *Proc. of the Beam Instrumentation Workshop 2008* (Lake Tahoe, CA, 2008), pp. 153–157.

[38] L. Frölich, Ph.D. thesis, University of Hamburg, Hamburg, Germany (2005).

[39] T. Watanabe, J. Sugahara, T. Yoshimatsu, S. Sasaki, Y. Sugiyama, K. Ishi, Y. Shibata, Y. Kondo, K. Yoshii, T. Ueda, et al., "Overall comparison of subpicosecond electron beam diagnostics by the polychromator, the interferometer and the femtosecond streak camera," Nucl. Instrum. Meth. A **480**, 315 (2002).

[40] M. Ding, H. Weits, and D. Oepts, "Coherent transition radiation diagnostic for electron bunch shape measurement at felix," Nucl. Instrum. Meth. A **393**, 504 (1997).

[41] A. H. Lumpkin and J. Ruan, in *Proc. of the 13th Beam Instrumentation Workshop* (Lake Tahoe, California, 2008), pp. 258–262.

[42] A. Lumpkin, "The next generation of rf FEL (free electron laser) diagnostics: synchroscan and dual-sweep streak camera techniques," Nucl. Instrum. Meth. A. **304**, 31 (1991).

[43] Hamamatsu Corp., "Guide to Streak Cameras,", `http://www.hamamatsu.com/` (2008).

[44] K. McDonald and D. Russell, in *Frontiers of Particle Beams; Observation, Diagnosis and Correction*, edited by M. Month and S. Turner (Springer Berlin / Heidelberg, 1989), vol. 343 of *Lecture Notes in Physics*, pp. 122–132.

[45] P. Lapostolle, "Quelques effets essentiels de la charge despace dans les faisceaux continus,", Report CERN/DI-70-36 (1970).

[46] M. Zhang, "Emittance formula for slits and pepper pot measurement,", FERMILAB-TM-1988 (1996).

[47] O. Luiten et al., "How to Realize Uniform Three-Dimensional Ellipsoidal Electron Bunches," Phys. Rev. Lett. **93**, 094802 (2004).

[48] J. Moody et al., "Longitudinal phase space characterization of the blow-out regime of rf photoinjector operation," Phys. Rev. ST Accel. Beams **12**, 070704 (2009).

[49] P. Musumeci et al., "Experimental Generation and Characterization of Uniformly Filled Ellipsoidal Electron-Beam Distributions," Phys. Rev. Lett. **100**, 244801 (2008).

[50] K. Flöttmann, "ASTRA,", `http://www.desy.de/~mpyflo`.

[51] R. W. Boyd, *Nonlinear Optics* (Academic Press, 2008), 3rd ed.

[52] Butcher, P.N. and Cotter, D., *The Elements of Nonlinear Optics* (Cambridge University Press, New York, US, 1990).

[53] P. Lazaridis, G. Debarge, and P. Gallion, "Time-bandwidth product of chirped sech(2) pulses: application to phase-amplitude-coupling factor measurement: addendum," Opt. Lett. **21**, 164 (1996).

[54] L. Cohen, "Time-frequency distributions-a review," Proceedings of the IEEE **77**, 941 (1989).

[55] K. B. Wolf, M. A. Alonso, and G. W. Forbes, "Wigner functions for Helmholtz wave fields," J. Opt. Soc. Am. A **16**, 2476 (1999).

[56] M. J. Bastiaans, "Wigner distribution function and its application to first-order optics," J. Opt. Soc. Am. **69**, 1710 (1979).

[57] R. Paschotta, *Encyclopedia of Laser Physics and Technology* (Wiley-VCH, Weinheim, Germany, 2008), 1st ed.

[58] E. Hecht, *Optics* (Addison Wesley, San Francisco, CA, 2002), 4th ed.

[59] G. Ghosh, “Dispersion-equation coefficients for the refractive index and birefringence of calcite and quartz crystals,” Opt. Commun. **163**, 95 (1999).

[60] Z. Jiang and X.-C. Zhang, “Electro-optic measurement of THz field pulses with a chirped optical beam,” Appl. Phys. Lett. **72**, 1945 (1998).

[61] M. J. Fitch, Ph.D. thesis, University of Rochester (2000).

[62] M. Brunken et al., “Electro-Optic Sampling at the TESLA Test Accelerator: Experimental Setup and First Results,”, TESLA Report 2003-11 (2003).

[63] G. Berden, S. Jamison, A. MacLeod, W. Gillespie, B. Redlich, and A. van Der Meer, “Electro-Optic Technique with Improved Time Resolution for Real-Time, Nondestructive, Single-Shot Measurements of Femtosecond Electron Bunch Profiles,” Phys. Rev. Lett. **93**, 1 (2004).

[64] Q. Chen, M. Tani, Z. Jiang, and X.-C. Zhang, “Electro-optic transceivers for terahertz-wave applications,” J. Opt. Soc. Am. B **18**, 823 (2001).

[65] I. Wilke et al., “Single-Shot Electron-Beam Bunch Length Measurements,” Phys. Rev. Lett. **88**, 124801 (2002).

[66] S. Casalbuoni et al., “Numerical Studies on the Electro-Optic Sampling of Relativistic Electron Bunches,”, TESLA Report 2005-01 (2005).

[67] S. P. Jamison, A. M. MacLeod, G. Berden, D. A. Jaroszynski, and W. A. Gillespie, “Temporally resolved electro-optic effect,” Opt. Lett. **31**, 1753 (2006).

[68] K. Y. Kim, B. Yellampalle, G. Rodriguez, R. D. Averitt, a. J. Taylor, and J. H. Glownia, “Single-shot, interferometric, high-resolution, terahertz field diagnostic,” Appl. Phys. Lett. **88**, 041123 (2006).

[69] B. R. Steffen, Ph.D. thesis, University of Hamburg (2007).

[70] B. Steffen, V. Arsov, G. Berden, W. Gillespie, S. Jamison, A. MacLeod, A. van Der Meer, P. Phillips, H. Schlarb, B. Schmidt, et al., “Electro-optic time profile monitors for femtosecond electron bunches at the soft x-ray free-electron laser FLASH,” Phys. Rev. ST Accel. Beams **12**, 032802 (2009).

[71] A. Azima, Ph.D. thesis, University of Hamburg (2009).

[72] J. Kim and D. Kim, “Characterization of a polarization-resolved high spectral resolution UV-visible spectrometer,” Rev. Sci. Instr. **79**, 033109 (2008).

[73] P. Tournois, “Acousto-optic programmable dispersive filter for adaptive compensation of group delay time dispersion in laser systems,” Opt. Commun. **140**, 245 (1997).

[74] H. Enqvist, “A setup for efficient frequency tripling of high-power femtosecond laser pulses,” Lund Reports on Atomic Physics **LRAP-330** (2004).

[75] D. You, R. R. Jones, P. H. Bucksbaum, and D. R. Dykaar, “Generation of high-power sub-single-cycle 500-fs electromagnetic pulses,” Opt. Lett. **18**, 290 (1993).

[76] G. Gallot and D. Grischkowsky, “Electro-optic detection of terahertz radiation,” J. Opt. Soc. Am. B **16**, 1204 (1999).

[77] B. Yellampalle, K. Y. Kim, G. Rodriguez, J. H. Glownia, and a. J. Taylor, “Algorithm for high-resolution single-shot THz measurement using in-line spectral interferometry with chirped pulses,” Appl. Phys. Lett. **87**, 211109 (2005).

[78] S. P. Jamison, G. Berden, P. J. Phillips, W. a. Gillespie, and a. M. MacLeod, "Upconversion of a relativistic Coulomb field terahertz pulse to the near infrared," Appl. Phys. Lett. **96**, 231114 (2010).

[79] J. van Tilborg, N. H. Matlis, G. R. Plateau, and W. P. Leemans, "Optical sideband generation: a longitudinal electron beam diagnostic beyond the laser bandwidth resolution limit," AIP Conference Proceedings **1299**, 565 (2010).

[80] F. G. Sun, Z. Jiang, and X.-C. Zhang, "Analysis of terahertz pulse measurement with a chirped probe beam," Applied Physics Letters **73**, 2233 (1998).

[81] J. Fletcher, "Distortion and uncertainty in chirped pulse thz," Opt. Express **10**, 1425 (2002).

[82] X.-Y. Peng, O. Willi, M. Chen, and A. Pukhov, "Optimal chirped probe pulse length for terahertz pulse measurement," Opt. Express **16**, 12342 (2008).

[83] A. E. Siegman, *Lasers* (University Science Books, Sausalito, California, 1986).

[84] J. Liu, D. Shen, S.-C. Tam, and Y.-L. Lam, "Modeling pulse shape of Q-switched lasers," IEEE J. Quantum Elect. **37**, 888 (2001).

[85] S. Schreiber et al., in *Proc. of the 21st International Conference on Free Electron Laser and 6th FEL Applications Workshop* (Hamburg, Germany, 1999), pp. 23–28.

[86] H. Schlarb et al., in *Proc. of the 8th European Workshop on Beam Diagnostics and Instrumentation for Particle Accelerators* (Venice, Italy, 2007), pp. 307–309.

[87] G. M. Knippels et al., "Two-color facility based on a broadly tunable infrared free-electron laser and a subpicosecond-synchronized 10-fs-Ti:sapphire laser.," Opt. Lett. **23**, 1754 (1998).

[88] F. Kiewiet et al., "Femtosecond synchronization of a 3 GHz RF oscillator to a mode-locked Ti:sapphire laser," Nucl. Instrum. Meth. A **484**, 619 (2002).

[89] M. Shea, R. Goodwin, and M. Kucera, "Internet Rack Monitor,", `http://www-inteng.fnal.gov/Integrated_Eng/irm/` (2010).

[90] R. Trebino, *Frequency-Resolved Optical Gating: The Measurement of Ultrashort Laser Pulses* (Kluwer Academic Publishers, Boston, Massachusettes, 2000).

[91] K. W. DeLong et al., "Frequency-resolved optical gating with the use of second-harmonic generation," J. Opt. Soc. Am. B **11**, 2206 (1994).

[92] R. Trebino, K. W. DeLong, D. N. Fittinghoff, J. N. Sweetser, M. A. Krumbugel, B. A. Richman, and D. J. Kane, "Measuring ultrashort laser pulses in the time-frequency domain using frequency-resolved optical gating," Review of Scientific Instruments **68**, 3277 (1997).

[93] D. N. Fittinghoff, J. L. Bowie, J. N. Sweetser, R. T. Jennings, M. A. Krumbüugel, K. W. DeLong, R. Trebino, and I. A. Walmsley, "Measurement of the intensity and phase of ultraweak, ultrashort laser pulses," Opt. Lett. **21**, 884 (1996).

[94] S. Linden, H. Giessen, and J. Kuhl, "Xfrog a new method for amplitude and phase characterization of weak ultrashort pulses," Physica Status Solidi B **206**, 119 (1998), ISSN 1521-3951.

[95] C. Iaconis and I. Walmsley, "Spectral phase interferometry for direct electric-field reconstruction of ultrashort optical pulses," Opt. Lett. **23**, 792 (1998).

[96] L. Gallmann, D. Sutter, N. Matuschek, G. Steinmeyer, U. Keller, C. Iaconis, and I. Walmsley, in *Conference on Lasers and Electro-Optics, 2000* (2000), pp. 583 –584.

[97] G. Taft, A. Rundquist, M. Murnane, I. Christov, H. Kapteyn, K. DeLong, D. Fittinghoff, M. Krumbugel, J. Sweetser, and R. Trebino, “Measurement of 10-fs laser pulses,” IEEE Journal of Selected Topics in Quantum Electronics **2**, 575 (1996).

[98] K. W. DeLong, R. Trebino, and D. J. Kane, “Comparison of ultrashort-pulse frequency-resolved-optical-gating traces for three common beam geometries,” J. Opt. Soc. Am. B **11**, 1595 (1994).

[99] Technology and Applications Center, Newport Corp., “Application Note 33: Amplitude and Phase Characterization of Ultrashort Laser Pulses,”, `http://assets.newport.com/webDocuments-EN/images/12246.pdf` (2007).

[100] D. N. Nikogosyan, “Beta barium borate (BBO),” Appl. Phys. A - Mater. **22**, 1013 (1991).

[101] A. W. Weiner, “Effect of group velocity mismatch on the measurement of ultrashort optical pulses via second harmonic generation,” IEEE J. Quantum Electron. **19**, 1276 (1983).

[102] Femtosoft Technologies, “FROG (v. 3.2.2),”, `http://www.femtosoft.biz` (2006).

[103] K. W. DeLong and R. Trebino, “Improved ultrashort pulse-retrieval algorithm for frequency-resolved optical gating,” J. Opt. Soc. Am. A **11**, 2429 (1994).

[104] R. Trebino and D. J. Kane, “Using phase retrieval to measure the intensity and phase of ultrashort pulses: frequency-resolved optical gating,” J. Opt. Soc. Am. A **10**, 1101 (1993).

[105] P. Piot et al., in *Proc. of the 33rd Free Electron Laser Conference* (Shanghai, China, 2011).

[106] P. Piot, Y.-E. Sun, J. G. Power, and M. Rihaoui, “Generation of relativistic electron bunches with arbitrary current distribution via transverse-to-longitudinal phase space exchange,” Phys. Rev. ST Accel. Beams **14**, 022801 (2011).

[107] M. Rihaoui, P. Piot, J. G. Power, Z. Yusof, and W. Gai, “Observation and simulation of space-charge effects in a radio-frequency photoinjector using a transverse multibeamlet distribution,” Phys. Rev. ST Accel. Beams **12**, 124201 (2009).

[108] M. Reiser, *The Theory and Design of Charged Particle Beams*, Wiley Series in Beam Physics and Accelerator Technology (Wiley, New York, 1994), p. 74.

[109] W. Graves, F. Kaertner, D. Moncton, and P. Piot, “Intense Super-radiant X-rays from a Compact Source using a Nanocathode Array and Emittance Exchange,” (2012), `arXiv:physics.acc-ph/1202.0318`.